IntechOpen

New Trends in Structural Engineering

Edited by Hakan Yalciner
and Ehsan Noroozinejad Farsangi

NEW TRENDS IN STRUCTURAL ENGINEERING

Edited by **Hakan Yalciner**
and **Ehsan Noroozinejad Farsangi**

New Trends in Structural Engineering
http://dx.doi.org/10.5772/intechopen.73625
Edited by Hakan Yalciner and Ehsan Noroozinejad Farsangi

Contributors

Bilge Doran, Hasan Orhun Koksal, Selen Aktan, Cengiz Karakoç, Oktay Jafarov, Hyeon-Jong Hwang, Akira Aikawa, Teng Wang, Yanmei Ding, Yu Song, Wangchun Zhang, Ali M. Memari, Mohammad Aliaari

© The Editor(s) and the Author(s) 2018
The rights of the editor(s) and the author(s) have been asserted in accordance with the Copyright, Designs and Patents Act 1988. All rights to the book as a whole are reserved by INTECHOPEN LIMITED. The book as a whole (compilation) cannot be reproduced, distributed or used for commercial or non-commercial purposes without INTECHOPEN LIMITED's written permission. Enquiries concerning the use of the book should be directed to INTECHOPEN LIMITED rights and permissions department (permissions@intechopen.com).
Violations are liable to prosecution under the governing Copyright Law.

Individual chapters of this publication are distributed under the terms of the Creative Commons Attribution 3.0 Unported License which permits commercial use, distribution and reproduction of the individual chapters, provided the original author(s) and source publication are appropriately acknowledged. If so indicated, certain images may not be included under the Creative Commons license. In such cases users will need to obtain permission from the license holder to reproduce the material. More details and guidelines concerning content reuse and adaptation can be foundat http://www.intechopen.com/copyright-policy.html.

Notice

Statements and opinions expressed in the chapters are these of the individual contributors and not necessarily those of the editors or publisher. No responsibility is accepted for the accuracy of information contained in the published chapters. The publisher assumes no responsibility for any damage or injury to persons or property arising out of the use of any materials, instructions, methods or ideas contained in the book.

First published in London, United Kingdom, 2018 by IntechOpen
eBook (PDF) Published by IntechOpen, 2019
IntechOpen is the global imprint of INTECHOPEN LIMITED, registered in England and Wales, registration number: 11086078, The Shard, 25th floor, 32 London Bridge Street
London, SE19SG – United Kingdom
Printed in Croatia

British Library Cataloguing-in-Publication Data
A catalogue record for this book is available from the British Library

Additional hard and PDF copies can be obtained from orders@intechopen.com

New Trends in Structural Engineering
Edited by Hakan Yalciner and Ehsan Noroozinejad Farsangi

p. cm.

Print ISBN 978-1-78984-506-8

Online ISBN 978-1-78984-507-5

eBook (PDF) ISBN 978-1-83881-745-9

Meet the editors

Associate Professor Dr. Hakan Yalciner is an earthquake and structure engineer in Erzincan Binali Yıldırım University and chair in the Department of Civil Engineering. Dr. Yalciner received his PhD from Eastern Mediterranean University. He is a voting member of ACI Committees 546-00 (Repair of Concrete) and 546-0E (Corrosion Studies). His research interests include performance analysis of structures under extreme conditions and loads, such as corrosion, seismic events, and blast. Dr. Yalciner developed different empirical models for the prediction of the structural behavior of corroded reinforced concrete members. He is currently director of the 13th March of Structural Mechanics Laboratory in Erzincan Binali Yıldırım University. His total accepted budget for academic projects in 2018 was US$250,000.

Dr. Ehsan Noroozinejad Farsangi is currently serving as an associate professor in the Department of Earthquake Engineering at Graduate University of Advanced Technology, Iran. He obtained his doctorate degree from the International Institute of Earthquake Engineering and Seismology, Tehran. He is also serving as the deputy editor of the *International Journal of Earthquake and Impact Engineering*, UK, and is a voting member of the International Union of Laboratories and Experts in Construction Materials, Systems and Structures technical committee on Structural Performance and Design of Structures. His current research interests include structural dynamics and vibration control; multihazard protection of structures from earthquake, blast, fire, and wind; resilience-based design; finite element methods; fiber-reinforced polymers in prestressed concrete structures; and infrastructure engineering.

Contents

Preface

The primary intention of this book is to embark on a journey that takes the reader through the latest concepts, techniques, and trends in structural engineering. This publication is mainly focused on structural engineering principles in the simulation, modeling, and design of structural elements. In addition, factors affecting structural response and behavior are investigated. The book is addressed to researchers and practitioners on the subject, as well as undergraduate and postgraduate students and other experts and newcomers seeking more information about the state of the art, new challenges, innovative solutions, and new trends and developments in these areas.

The behavior and design of masonry walls is the subject of Chapters 1 and 2. In the first chapter, two formulations were proposed by the authors for masonry walls confined with fiber-reinforced polymers, which are adjusted for the cohesion and internal friction angle of both units and mortar. In the second chapter, a discussion on experimental tests carried out on different types of fuse elements as well as quarter-scale specimen of frame and infill walls with fuse elements is presented. Later on, the results of finite element computer modeling studies are presented and verified through experimental analysis.

Chapter 3 is dedicated to a novel prefabricated steel-reinforced concrete composite column. In the proposed column, four steel angles are placed at the corners of the cross-section, and transverse bars and plates are used to connect the angles by welding or bolting. In this chapter, the newly developed composite column is introduced, and basic mechanisms, structural performance, and field applications are discussed.

Chapter 4 deals with the behavior of a simply-supported beam (SSB) reinforced with external prestressing using three diagonal web members. A theoretical model was created for the reinforced SSB. Then equations governing the relationship between beam deflection and increment in external tendon force and the relationship between load and deflection were derived. Later, finite element analysis was performed to study the effects of cross-sectional area of the tendon, tendon sag, initial tendon force, and other factors on the structural performance of an SSB after reinforcement.

The final chapter, Chapter 5, discusses the vertical natural vibration modes of a ballasted railway track. This study measured the natural vibration characteristics of the ballast layer using field measurements, full-scale impact loading experiments, and large-scale finite element analysis.

It is our hope that this book, which integrates the modeling and design aspects of various structural systems, will serve as a comprehensive guide and reference for practicing engineers and educators, and, more importantly, as a welcome mat for recent graduates entering the structural engineering profession by assuring them that they have discovered an exciting world of challenges and opportunities.

Associate Professor Dr. Hakan Yalçiner
Department of Civil Engineering
Erzincan University
Erzincan, Turkey

Assistant Professor Dr. Ehsan Noroozinejad Farsangi
Department of Earthquake Engineering
KGUT
Iran

Section 1

Behavior and Design of Masonry Walls

Chapter 1

Constitutive Modeling of Masonry Walls Strengthened with Fiber Reinforced Polymers

Bilge Doran, Hasan Orhun Köksal, Selen Aktan,
Oktay Jafarov and Cengiz Karakoç

Additional information is available at the end of the chapter

http://dx.doi.org/10.5772/intechopen.77201

Abstract

This study primarily focuses on the constitutive modeling of masonry walls strengthened with fiber-reinforced polymers (FRP). In general, providing suitable relations for the material characterization of the masonry constituents so that the nonlinear finite element (NLFEA) applications of the elasto-plastic theory achieves a close fit to the experimental load-displacement diagrams of the walls subjected to in-plane loadings is desired. In this chapter, two relations proposed for masonry columns confined with FRP are adjusted for the cohesion and the internal friction angle of both units and mortar. Relating the mechanical parameters to the uniaxial compression strength and the hydrostatic pressure acting over the wall surface, the effects of major and intermediate principal stresses σ_1 and σ_2 on the yielding and the shape of the deviatoric section are then reflected into the analyses. Finally, NLFEA results for the walls tested in different studies showed a good match with the experimental ones.

Keywords: masonry wall, fiber reinforced polymer, cohesion, internal friction, elasto-plastic analysis, finite element analysis

1. Introduction

Many historical masonry buildings of the world's architectural heritage are in dire need of retrofitting as they do not perform well to the seismic activities. Retrofitting of such structures needed better understanding of the constitutive features to characterize its present condition and determine the true structural safety for seismic actions. Although masonry has been used in building for centuries in many countries such as Turkey, constitutive models and calculation techniques have not yet been available that allow realistic descriptions of the mechanic behavior of structures made of this heterogeneous material. During the last decade, the interest in seismic retrofitting of masonry structures has led to the development of specific engineering techniques and strategies in seismic areas. In this context, fiber-reinforced polymer (FRP) offered a capable alternative solution for retrofitting of masonry structures instead of conventional retrofitting techniques such as ferrocement, grout injection, and so on. Unreinforced masonry (URM) walls are the main load-bearing elements of masonry structures and the use of FRP enhances the strength, flexibility, and ductility under earthquake loading. Therefore, techniques of FRP application has become very effective in the strengthening of damaged URM walls. However, the strengthening of masonry structures by means of carbon fibers still lacks adequate theoretical and experimental verification, unlike reinforced concrete (RC) structures. Therefore, attention should be primarily focused on the description of the URM- and FRP-confined wall behavior under shear and compression. This study aims to investigate the finite element analysis (FEA) of URM walls strengthened with FRP composites by adopting an elasto-plastic approach proposed for the assessment of FRP-confined masonry columns under uniaxial compression [1].

A large literature has grown up which extends analytical and numerical models applied to masonry structures. These models involve mechanical parameters that are difficult to measure and cannot be implemented practically into numerical analyses [2–13]. Researchers related to detailed micro-, simplified micro- and macro-FE modeling of masonry walls subjected to compression and shear have initially taken similar steps in the modeling process for masonry prisms and columns under concentric loading. Proceeding in a similar way with that used for the RC members [8, 9, 11, 12] employed a general-purpose finite element program LUSAS [14] for modeling the unreinforced and reinforced masonry prisms and columns activating both the elasto-plastic and isotropic damage models to reflect the nonlinear behavior of the blocks, grout, and mortar joints. Masonry walls were assumed as isotropic and elastic ignoring the influence of mortar joints acting as planes of weakness. The fact that a complete constitutive model should reflect the inelastic material properties of the units and mortar and a failure criterion describing the conditions for failure under combined compression-tension required more detailed analytical studies [15] and experimental investigations [16]. A micromodel should include several material parameters such as modulus of elasticity, Poisson's ratio, cohesion, internal friction angle, and compressive and tensile strength for the representation of units and mortar. Moreover, the composite unit-mortar interface model requires additional material parameters for the description of the interface behavior, for example, tensile strength, cohesion, internal friction angle, compressive strength, tensile fracture energy, shear fracture energy, dilatancy angle, and the close prediction for the experimental load-displacement diagram could be possible in the application of the theoretical model if the shear properties were reduced to 30%, the compressive strength to 20%, and the compressive fracture energy was multiplied by three [17]. From the engineering point of view, there is considerable limitation in the applicability of these sophisticated models [18–23] to FE analysis of masonry walls unless rational relations for the material parameters necessary to explain the models are provided.

The implementation of the plasticity theory to FRP-strengthened masonry walls under vertical and lateral loads by considering the constitutive behavior of masonry units, mortar, and FRP composite material separately, in this study, is analyzed. Köksal et al. [1] considered FRP-confined masonry columns as pressure-dependent material structures based on Drucker-Prager (DP) criterion. A DP-type yield criterion is also employed relating the cohesion and the internal friction angle of both the masonry unit and mortar to their uniaxial compressive strength by extending the previous approach to the FRP-strengthened masonry walls. For this purpose, an extensive parametric study is performed in order to explain the mechanical properties of masonry units and mortar with only one single parameter, that is, their uniaxial compressive strength [24]. Seven masonry walls are considered here. Three of them [25, 26] were unreinforced, single-sided strengthened with glass fiber-reinforced polymer (GFRP), and strengthened by carbon fiber-reinforced polymers (CFRP) strips on one side, respectively. Two of them [27] were strengthened by polyethylene terephthalate (PET) fiber sheets with unidirectional fiber; one was fully wrapped and the other was partially wrapped with both vertical and horizontal strips of PET sheets. One of them [28] was double-sided strengthened with FRP and the other [29] was unreinforced masonry walls, respectively. These seven walls are successively analyzed using FEA method with the proposed approach in LUSAS software [14].

2. The mechanics of constitutive modeling

A large literature has grown up which extends analytical and numerical models applied to masonry structures. These models involve mechanical parameters that are difficult to measure and cannot be implemented practically into numerical analyses. Several experimental and analytical studies on the behavior of masonry shear walls as the main structural component of masonry have been carried out in order to obtain a comprehensive approach for the overall assessment of masonry behavior [18, 21, 30–35]. Proposed theoretical models for implementation to FE analysis of masonry generally require a large number of material parameters that are difficult to measure easily and reliably. For this reason, several attempts have been made to express the stress-strain relationships of the masonry and its constituents using different modeling techniques such as micro-modeling, homogenization approach, and macro-modeling. The common approach in these studies is to treat masonry as a continuous medium or an equivalent continuous medium with the exception of detailed micro-modeling. Detailed micro-modeling should describe the masonry, mortar, and the interaction behavior between them [22, 36–38]. Köksal et al. [1, 8, 9] have performed FE analysis of masonry prisms and columns strengthened with FRP describing the constitutive behavior of the unit, mortar, and FRP separately. The similar approach has been adopted for the FE modeling of masonry shear walls while making the assumption that the material description of the mortar includes the effect of the unit-mortar interface behavior. Since the most common test performed on concrete-like brittle materials is for the measurement of its uniaxial compressive strength, it seems reasonable that the mechanical properties of masonry constituents can be assumed to be related to their compressive strengths. The authors have adopted this strategy in the elasto-plastic analyses of RC elements, masonry prisms, and columns, successively [1, 39, 40].

The most important mechanical parameter in FE analysis for masonry is the modulus of elasticity (E_m) determined by uniaxial compression tests. The failure mechanism and load-displacement behavior of masonry are strongly affected by the differences in the modulus of elasticity between unit and mortar [24, 41]. In detailed micro-modeling, modulus of elasticity of units and mortar are required for NLFEA of the masonry walls. The relations for the masonry constituents are given in **Table 1** [24, 42].

Multi-axial stress states generally define the behavior of the structures such as masonry walls, RC panels, confined columns, or elements loaded over a specified limited area. The basic plastic models, that is, Mohr-Coulomb (MC) and DP are widely adopted in constitutive modeling of frictional materials, like concretes, soils, and rocks, when describing the material behavior beyond the elastic range. Since material parameters of MC criterion are easily obtained from standard tests and are logical from the physical point of view, MC criterion is the most common used criterion in geotechnical and structural engineering [13]. MC criterion in three-dimensional (3D) stress space can be expressed as Eq. (1):

$$f(\xi, \rho, \theta) = \sqrt{2}\,\xi \sin\phi + \sqrt{3}\,\rho \sin\left(\theta + \frac{\pi}{3}\right) + \rho \cos\left(\theta + \frac{\pi}{3}\right) \sin\phi - \sqrt{6}\,c \cos\phi = 0 \qquad (1)$$

$$\mathit{for}\; 0 \prec \theta \prec \frac{\pi}{3}$$

where $\xi = I_1/\sqrt{3}$ $\xi = I_1/\sqrt{3}$and $\rho = \sqrt{2}\,J_2$ [43]. The invariants ξ and I_1 indicate the hydrostatic component of the current stress state. However, because of the smooth surface approximation to the six-faceted MC yield function, DP criterion is conversely easy to implement and allows a fast computation of plastic behavior, even it is a drawback from the physical point of view given as Eq. (2) [1, 44]:

$$f(\xi, \rho) = \sqrt{6}\,\alpha\xi + \rho - \sqrt{2}\,k = 0 \qquad (2)$$

where α and k are material constants. Generally, these constants are expressed in terms of the cohesion (c) and the internal friction angle (ϕ) [13]. Therefore, the surfaces of both DP and MC yield criteria are made to coincide along the compression meridian, and then the constants α and k are related to the constants c and ϕ by [45] given in Eq. (3):

$$\alpha = \frac{2\sin\phi}{\sqrt{3}(3 - \sin\phi)}, k = \frac{6c\cos\phi}{\sqrt{3}(3 - \sin\phi)} \qquad (3)$$

Material	**Expression**
Brick	$E_{br} = (300\text{~}700)\, f_{br}$
Block	$E_{bl} = 1000\, f_{bl}$
Mortar	$E_{mr} = 200\, f_{mr}$

Table 1. Expressions for modulus of elasticity of the masonry constituents.

In masonry columns strengthened with FRP, since the existence of major and intermediate principal stresses σ_1 and σ_2 will affect the yielding and the shape of the deviatoric section, the effect of FRP confinement should be included in the derivation of the material parameters. Due to the complexity of establishing a general failure surface in the principal stress space because of the lack of necessary experimental data, the mean stress $\sigma_m = I_1/3$ at the failure point is defined as a constant value which is corresponding to $(f_{mu} + 2f_l)/3$ at all stress levels. The cohesion and the internal friction angle of the units to include the confinement stresses are given as Eq. (4):

$$\frac{c_{mu}}{f_{mu}} = \frac{\tan\phi_{mu}}{3}\sqrt{\frac{|\sigma_m|}{f_{mu}}} \le \frac{c_{mu}}{f_{mu}}\bigg|_{\frac{|\sigma_m|}{f_{mu}} = 1} \tag{4}$$

$$\phi_{mu} = \phi_i - 0.75\frac{|\sigma_m|}{f_{mu}} \ge \phi_f = \phi_{mu}\bigg|_{\frac{|I_1|}{f_{mu}} = 1} \tag{5}$$

In Eq. (5), ϕ_i can be nearly equal to $\pi/3$ for brick and $\pi/4$ for concrete. Besides, applying the boundary condition, ϕ_f is approximately $\pi/4$ for brick and between $\pi/5$ and $\pi/6$ for concrete. For high hydrostatic pressures $(0 > \sigma_m/f_{mu} \ge -1)$, internal friction angle can be taken as a constant value, that is, 30°–35° for concrete and nearly 45° for clay brick as illustrated in **Figure 1**. Since much lower pressures exist on masonry walls and their constituents, material parameters have been calibrated to best reconcile the experimental data of several walls. In the wall tests, as the axial load level is less than the ultimate uniaxial strength, the mean stress can be taken as a constant value corresponding to $(p + 2f_l)/3$ at all stress levels. The validity of Eqs. (4) and (5) is finally verified by numerical simulations of the walls subjected to the pressures in the range of $\xi/f_{mu} \le -0.58$ throughout this study.

The use of the compressive meridian obviously causes some overestimation for the failure load for this case. In order to lessen this overestimation, an ending point definition for the termination of NLFEA should be needed. The ending point for the analysis can be determined

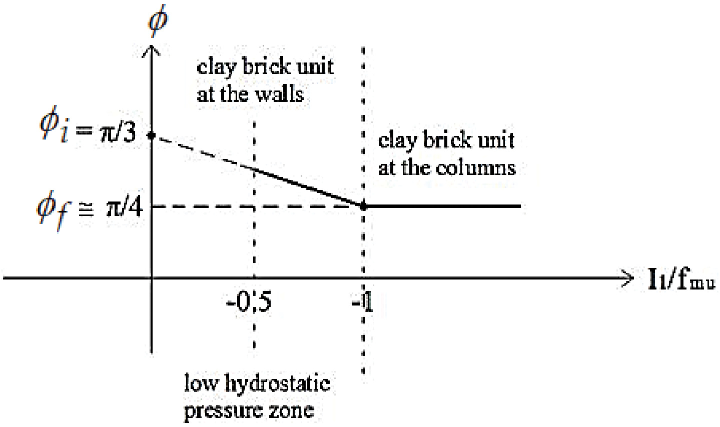

Figure 1. Plotting of Eq. (5) for the internal friction angle of clay brick [13].

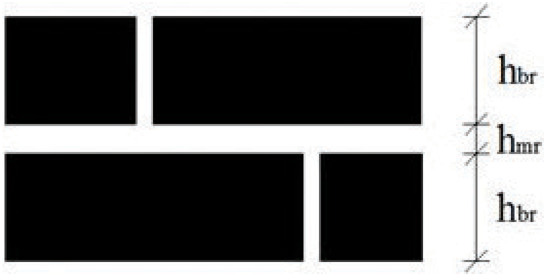

Figure 2. Assumption for the discontinuity surface between two units along the thickness of the mortar resulting failure of the wall [13].

defining the discontinuity surface between two units along the thickness of the mortar as illustrated in **Figure 2**. The maximum tensile strain can then be determined from the case of that a complete opening will occur along the mortar thickness between two units as given in Eq. (6):

$$\varepsilon_{\max} = h_{mr}/\left(2\,h_{br} + h_{mr)}\right. \tag{6}$$

Mortar generally governs the nonlinear behavior of masonry and has an influence on the axial strain of masonry prism and also on the shear response of the masonry walls [24, 46]. Therefore, any theoretical model should account for the nonlinear response of both the mortar and the unit-mortar interface to predict the inelastic behavior of masonry [41, 47]. In this study, the mechanical parameters of mortar, given in Eqs. (7) and (8), are adjusted to reflect the unit-mortar interface response as preferred in the modeling of masonry prisms and columns previously [1, 8]:

$$c_{mr} = 1.55\sqrt[3]{f_{mr}} \tag{7}$$

$$\phi_{mr} = 1.519 f_{mr} \tag{8}$$

3. Finite element modeling and model verification

Three-dimensional (3D) finite element models for masonry walls strengthened with FRP composites are developed in LUSAS [14]. Masonry constituents, that is, brick and mortar, are assumed to be isotropic elasto-plastic obeying DP criterion. They are modeled separately with eight-noded hexahedral element (HX8M) which is a solid element with an incompatible strain field as illustrated in **Figure 3a**. FRP composites are modeled by four-noded thick shell element (QTS4) which has a thick and thin curved shell geometry including multiple branched junctions as in **Figure 3b**. Both the element formulations take account of membrane, shear and flexural deformations, and are capable of modeling inelastic phenomenon.

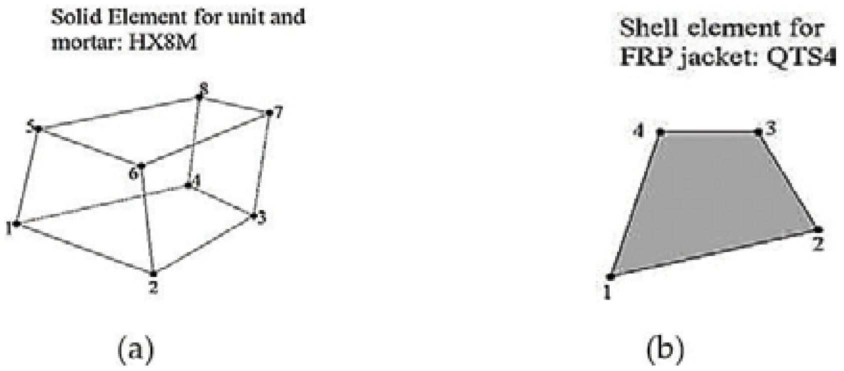

Figure 3. (a) Eight-noded hexahedral element for units and mortar and (b) four-noded thick shell element for FRP jacket [13].

Table 2 shows the material and geometrical properties for masonry walls with its FRP confinement evaluated in this study. All mechanical properties of the masonry constituents utilized in the analyses are also given in **Table 3**.

Stratford et al. [25] tested six 1200 × 1200 mm masonry panels under a combination of vertical preloading, and in-plane horizontal shear loading. Both clay and concrete brick specimens were tested while one specimen of each material was left unreinforced and the other two panels were single-sided strengthened using GFRP. GFRP had equal amounts of fibers in the horizontal and vertical directions (parallel to the mortar joints) and fibers were oriented at 45° to the joints. As can be seen in **Figure 4**, two connected hydraulic jacks (N) were placed on the wall while the shear load was applied to the wall by a horizontal hydraulic jack (P).

For the case of URM wall, the end point for the FEA is determined defining a discontinuity surface between two clay units along the thickness of the mortar. The maximum tensile strain pointing out that a complete opening will occur along the mortar thickness between two units, can be found by dividing the mortar joint thickness 10 mm by two block heights plus the mortar thickness as $10/(2 \times 65 + 10) = 0.071$. This strain value can be called critical tensile strain. As the lateral load is increased, the effect of tensile deformations grows up along the toe of the wall and it is easy to observe the critical tensile strain at the toe of the wall from **Figure 5**. If FEA ends when the ultimate tensile strain at the wall reaches the critical value, both simulation model and laboratory test results agreed very well as shown in **Figure 6**.

As can be seen in **Figure 6**, horizontal displacement at the failure is experimentally determined approximately as 14 mm. NLFEA gives a value of 13.81 mm from the use of the maximum tensile strain criterion for the wall. As can be seen in **Figures 5** and **7**, the region of concentrated maximum tensile strain matches the location of experimental crack pattern on the wall.

Figure 8 shows the stress-strain plots for strengthened wall Clay 2. The load-displacement plot obtained from NLFEA is well agreed with the experimental data. As shown in **Figure 9**, the analysis is terminated upon reaching the maximum tensile strain corresponding to the tensile strength of GFRP at a horizontal drift of 10.16 mm. This value is experimentally determined approximately as 12 mm.

Reference	Experiment	Precompression load (MPa)	Wall dimension (mm)	Brick dimension (mm)	FRP	
					E_{FRP} (MPa)	t (mm)
Stratford [25]	Clay 1 URM	1.38	1200 × 1200 × 60	228 × 65 × 60	-	-
	Clay 2 GFRP	1.38	1200 × 1200 × 60	228 × 65 × 60	73,300	0.15
Capozucca [26]	HRM-C2	1.5	840 × 633 × 50	100 × 17 × 50	240,000	0.177
Rahman and Ueda [27]	WALL 3 WALL 4	1.16	860 × 540 × 100	205 × 60 × 100	10,000	0.841
Mosallam and Banerjee [28]	W4-C-RT	1.29	1830 × 1830 × 203	406 × 152 × 203	96,500	1.60
Haider [29]	URM 6	0.5	2870 × 2408 × 150	310 × 76 × 150	-	-

Table 2. General characteristics of masonry walls and FRP confinement.

Reference	Experiment	Brick			Mortar		
		E_{mu} (MPa)	c_{mu} (MPa)	ϕ_{mu} (°)	E_{mr} (MPa)	c_{mr} (MPa)	ϕ_{mr} (°)
Stratford [25]	Clay1 URM	18,600	3.04	59.68	3250	3.45	16.71
	Clay 2 GFRP	18,600	3.04	59.68	3250	3.45	16.71
Capozucca [26]	HRM-C2	7000	2.33	59.37	150	2.21	4.41
Rahman and Ueda [27]	WALL 3	8000	2.27	58.94	125	12.5	18.90
	WALL 4	8000	2.16	59.06	125	12.5	18.90
Mosallam and Banerjee [28]	W4-C-RT	6000	2.32	57.66	800	3.79	22.20
Haider [29]	URM 6	20,000	0.90	59.54	1100	2.65	7.59

Table 3. Mechanical properties adopted for FE analyses.

In all experiments, except for the unreinforced clay specimen (Clay 1), the strengthened masonry walls (Clay 2) failed by rapid propagation of diagonal crack which followed the mortar joints as in **Figure 10a**. Crushing failure, which occurred when the compressive strength of the mortar was reached, cannot happen for these walls because of the mortar strength higher than 11 MPa. Shear failure, involving sliding along a slip plane either within the mortar or at the brick-mortar interface, is the main failure mode. The fracture pattern is well predicted through the concentration of the maximum tensile strains diagonally shown in **Figure 10b**.

Capozucca [26] investigated the behavior of historical reinforced masonry (HRM) walls strengthened by CFRP strips, experimentally. CFRP strips bonded to only one face of the specimen horizontally and vertically. FRP strips, containing unidirectional fibers, can be bonded to the surface of the wall and arranged to provide an external truss action [25]. The

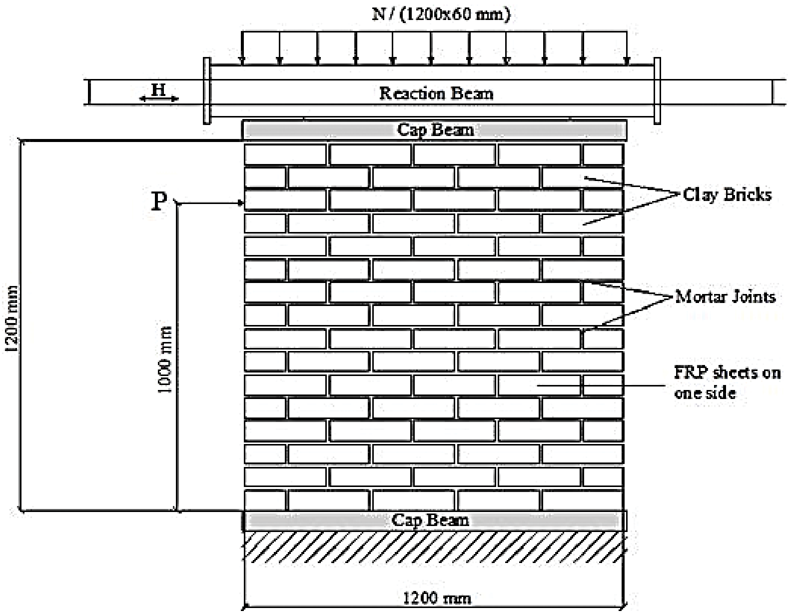

Figure 4. Experimental setup of shear wall Clay 2 [13].

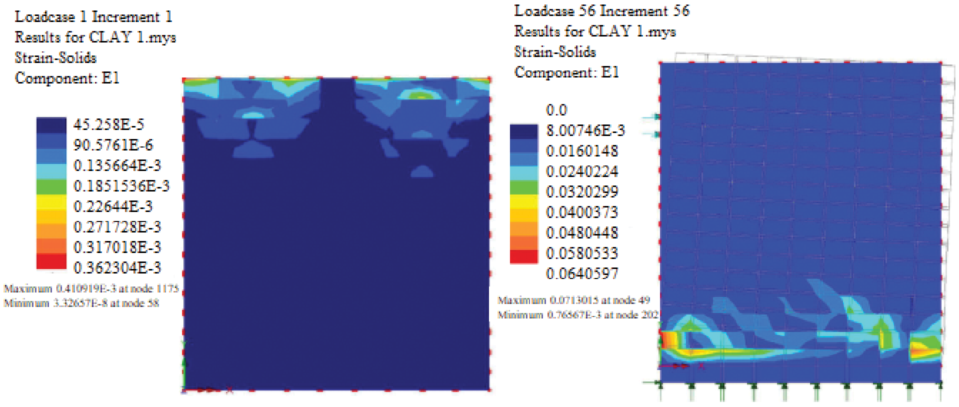

Figure 5. Maximum strains along the wall height for Clay 1 [13].

strengthened wall was subjected to cyclic loading until failure. Specimens were built with clay bricks and mortar with thickness 4 mm. Flexural tensile strength of mortar was 0.80 MPa. A single-story HRM C2 wall was built using historic full clay bricks in scale, one-third, and was tested in a special frame (**Figure 11**). Besides, mechanical and geometrical properties of brick, mortar and CFRP strips are given here in **Tables 2** and **3**.

Initially, pre-compression load (1.50 MPa) was applied to the flanges and web by three jacks, kept constant, then horizontal force was applied measuring horizontal force until failure [26]. Wall C2 damaged by cyclic shear tests and then was strengthened by 50 mm wide carbon strips

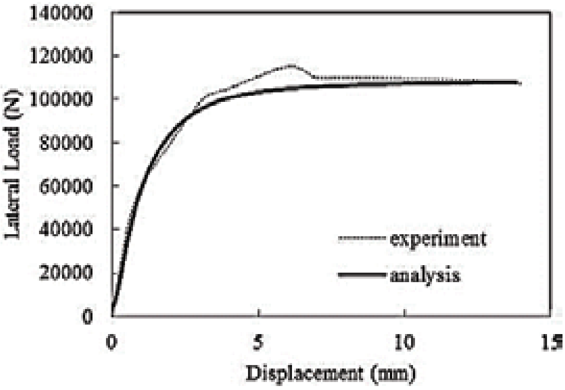

Figure 6. Lateral load-displacement responses for Clay 1 [13].

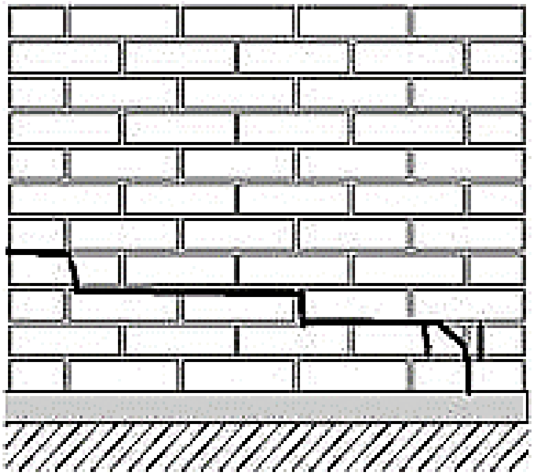

Figure 7. Experimental crack pattern for Clay 1 [13].

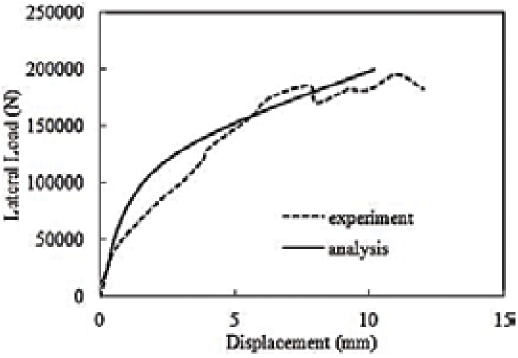

Figure 8. Lateral load-displacement responses for strengthened Clay 2 [13].

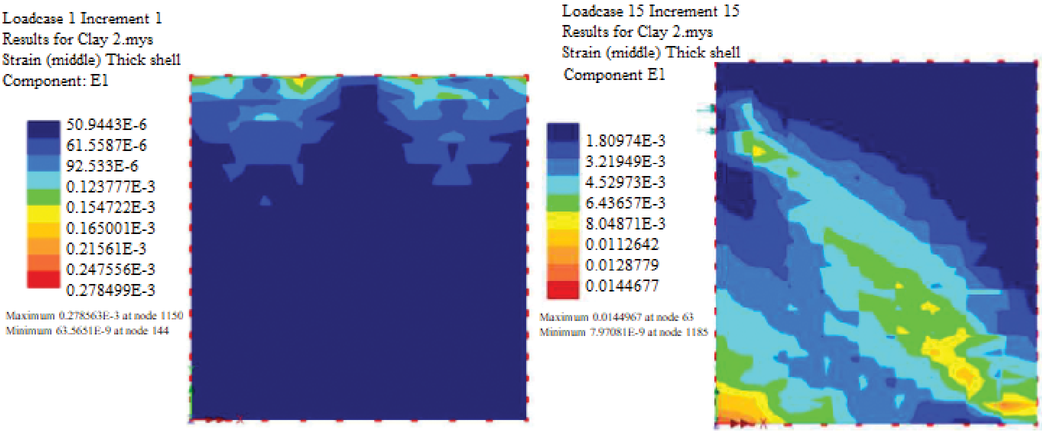

Figure 9. Maximum strain distribution over GFRP surface [13].

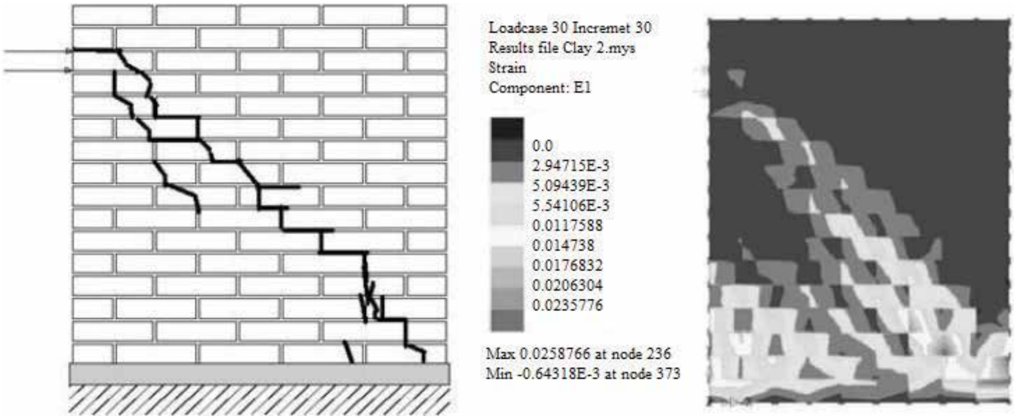

Figure 10. (a) Schematic crack patterns in strengthened wall (Clay 2) and (b) maximum tensile strains over unreinforced face in 3D FE model [13].

bonded to one side, parallel and normal to mortar joints. Mechanical parameters of CFRP strips are summarized in **Table 2**. Walls C1 and C2 were initially subjected, respectively, to five cyclic stages of horizontal force and seven cyclic stages before to bring the walls to failure by an ultimate stage with unidirectional horizontal force [26]. These are the possible reasons for the stiffer behavior observed in **Figures 12** and **13**. The critical tensile strain assumption for masonry is adopted for the stress-strain plots (**Figure 13**), while the analysis is terminated by reaching the tensile strength of GFRP as in **Figure 12**. Therefore, the material parameters for the masonry constituents of the pre-damaged walls should be somewhat lower than the recommended ones in Eqs. (4)–(7). The cohesion and internal friction angle values of the clay brick lowered by 35 and 15%, respectively. Since the mortar has already defined by a very weak material, any reduction on its mechanical properties will not be reasonable. Another reason for the stiffer predictions can be the present approach does not consider the debonding

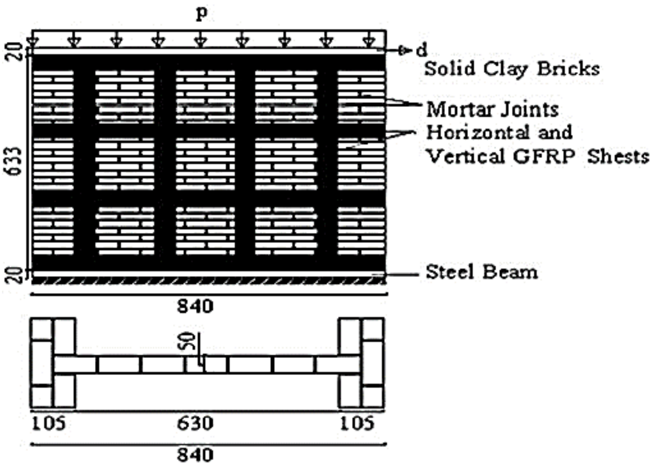

Figure 11. Geometrical details of HRM C2 wall [13, 26].

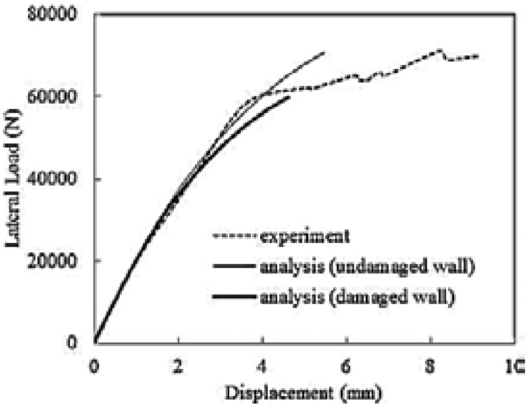

Figure 12. Comparison of load-displacement responses for pre-damaged HRM C2 wall employing the ultimate tensile strain criterion of GFRP [13].

phenomenon between the wall and FRP layer which affects the maximum lateral displacement of the wall particularly while reaching the ultimate load capacity [48].

Actually, presence of discontinuity surfaces with some specific values of separation affects the failure mechanisms and the level of FRP confinement in cracked and damaged walls. Therefore, the use of the critical tensile strain criterion instead of the ultimate tensile strength of FRP can be more reasonable for the analysis of pre-damaged walls.

Rahman and Ueda [27] studied the mechanical behavior of masonry walls experimentally. WALLS 1 and 2 were unreinforced, and WALLS 3 and 4 were fully (%100) and partially (%40) strengthened with FRP, respectively (**Figure 14**). The dimensions of each brick unit were 205 × 100 × 60 mm while the dimensions of walls were 860 × 540 × 100mm with an approximate mortar thickness of 10 mm. A pre-compression of 100 kN (1.16 MPa) was

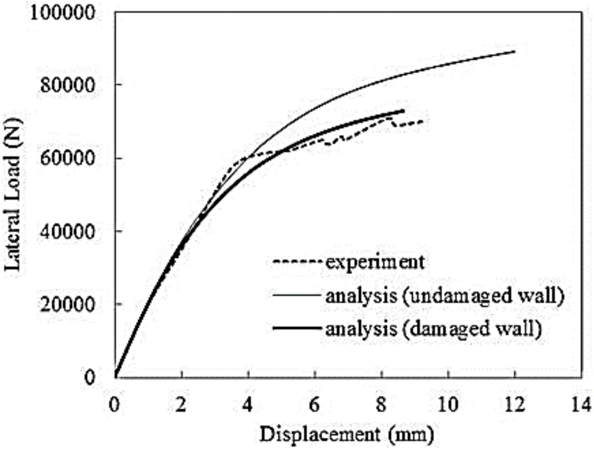

Figure 13. Comparison of load-displacement responses for pre-damaged HRM C2 wall adopting the maximum tensile strain criterion of masonry [13].

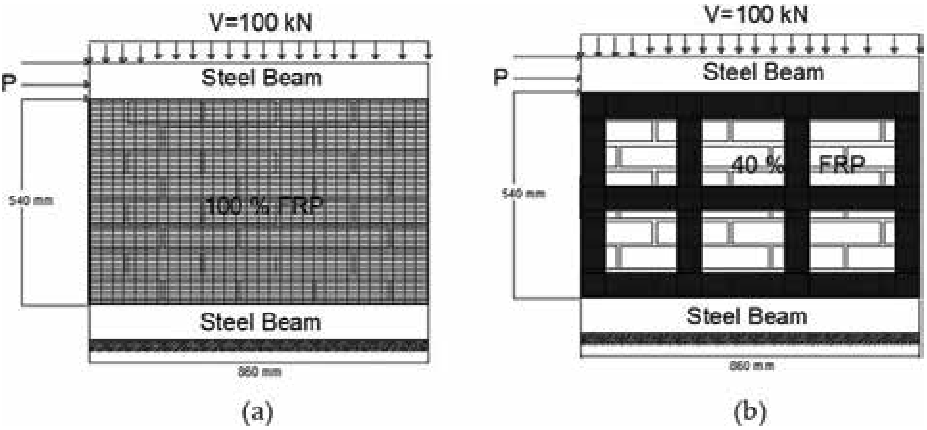

Figure 14. Geometrical details of experiments (a) WALL 3 and (b) WALL 4 [27].

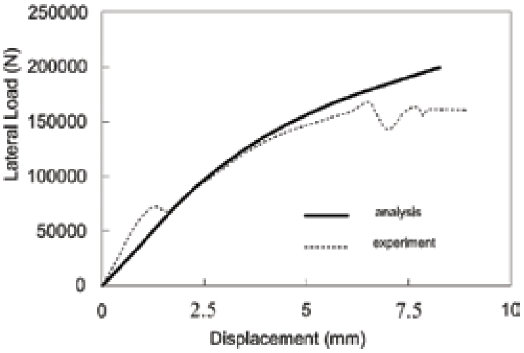

Figure 15. Comparison of load-displacement responses for WALL 3.

applied on the top of the wall. The modulus of elasticity and the tensile strength of FRP sheet were 10,000 and 740 MPa, respectively [49].

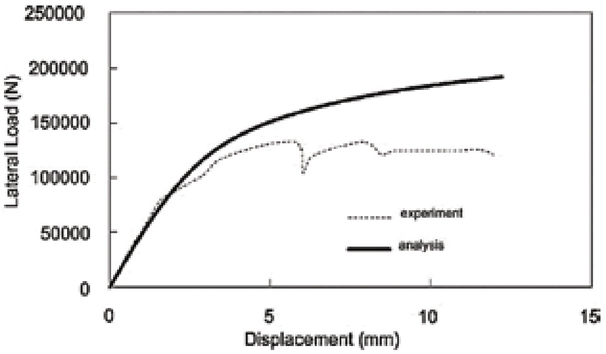

Figure 16. Comparison of load-displacement responses for WALL 4.

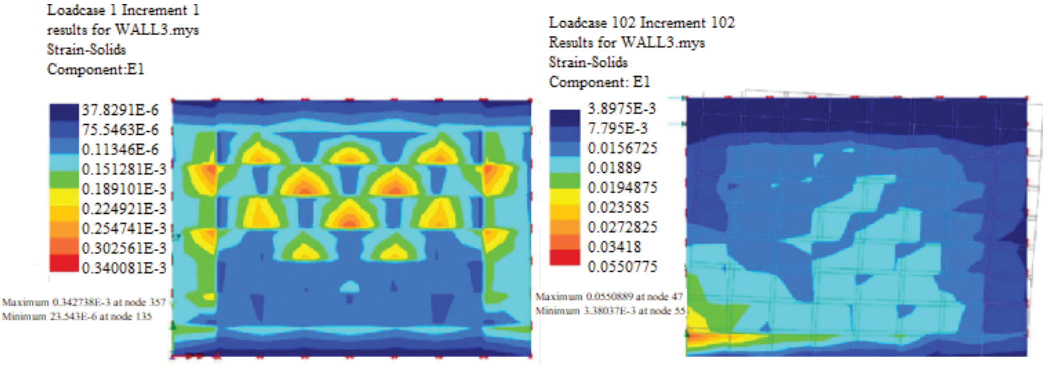

Figure 17. Maximum strains along the height of WALL 3.

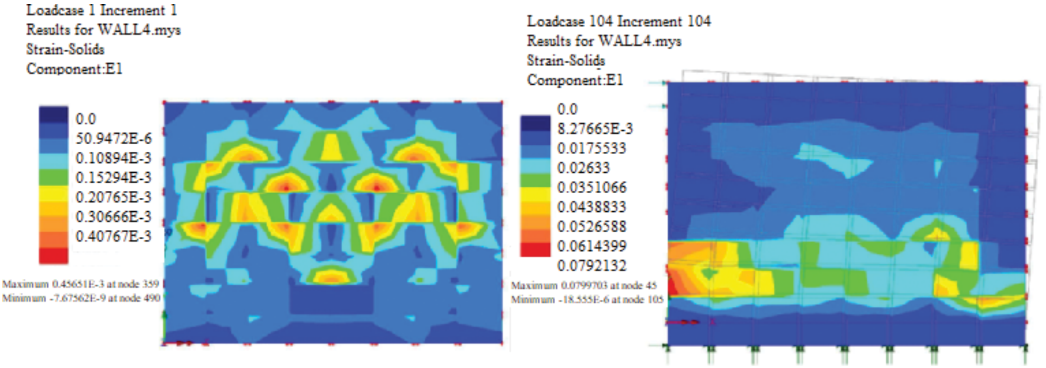

Figure 18. Maximum strains along the height of WALL 4.

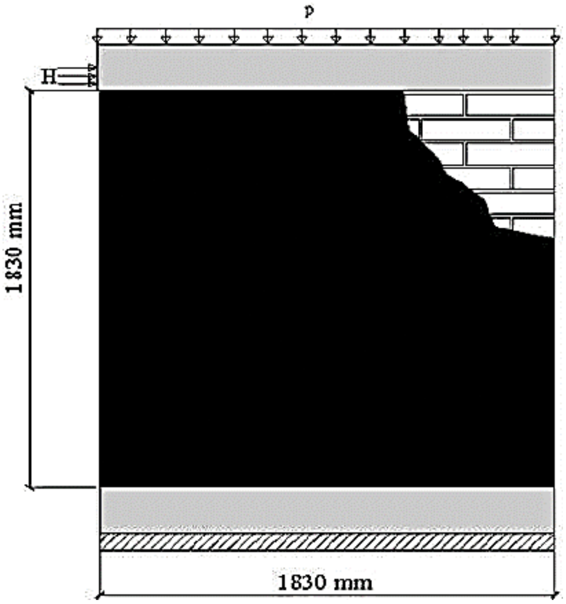

Figure 19. Experimental setup of W4-C-RT wall.

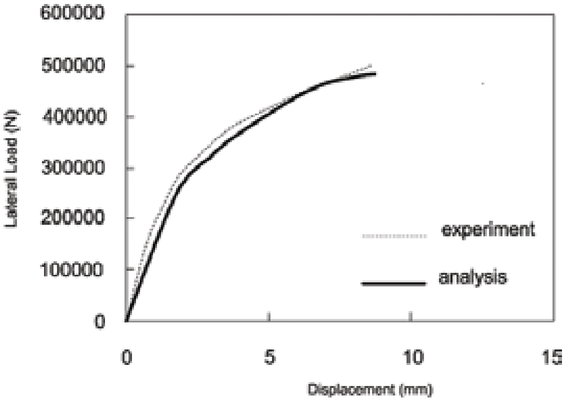

Figure 20. Lateral load-displacement responses for W4-C-RT.

The stress-strain plots for WALL 3 are shown in **Figure 15**. The load-displacement plot (**Figure 16**) obtained from NLFEA is well agreed with the experimental data. The analysis is terminated upon reaching the maximum tensile strain corresponding to the tensile strength of PET at a horizontal drift of 8.80 mm for WALL 3 (**Figure 17**). This value is experimentally determined approximately as 9.30 mm. Finally, the maximum strains along the wall height are depicted in **Figure 17**. The analysis is terminated upon reaching the maximum tensile strain corresponding to the tensile strength of PET at a horizontal drift of 12.50 mm (**Figure 18**). This value is experimentally determined approximately as 12.40 mm for WALL 4. In **Figure 18**, the maximum strains along the wall height can be seen.

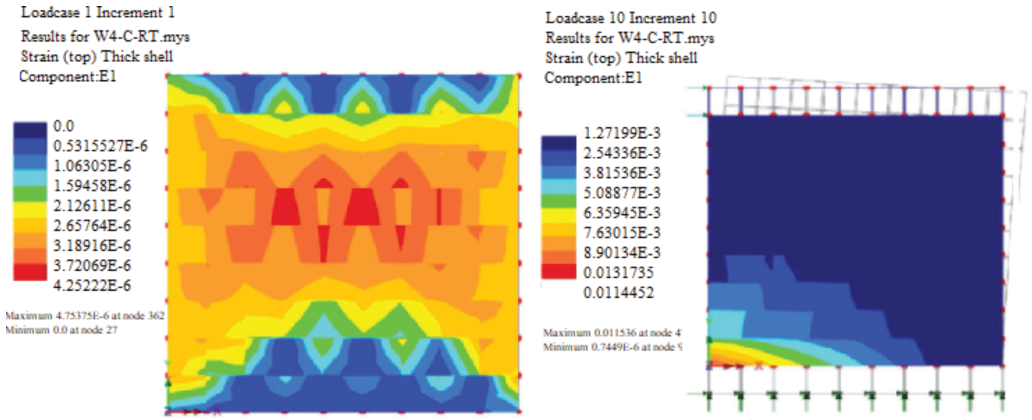

Figure 21. Maximum strains along the wall height (W4-C-RT).

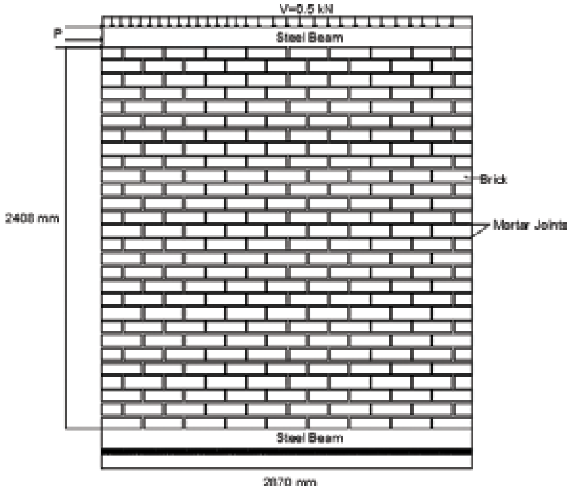

Figure 22. Experimental setup of URM 6 wall.

Mosallam and Banerjee [28] tested six identical masonry wall specimens of size 1830 × 1830 mm with 406 × 152 × 203 mm hollow concrete block under a combination of constant axial and incremental lateral loads (push-pull) (**Figure 19**). Two of them were unreinforced and the others were strengthened with different types of FRP elements. The compressive strength of masonry prisms, grout cylinders, and mortar cylinders was calculated as 2.16, 18.96, and 14.62 MPa, respectively. The tensile strength of FRP was 1061 MPa and modulus of elasticity was 96,500 MPa. In this study, W4-C-RT wall retrofitted wall specimen with double-sided carbon/epoxy laminate is considered. The rapture strain of FRP element is calculated as 0.011 from ratio of tensile stress of FRP to modulus of elasticity. Load-displacement curves obtained from experiments and numerical analysis are given in **Figure 20**.

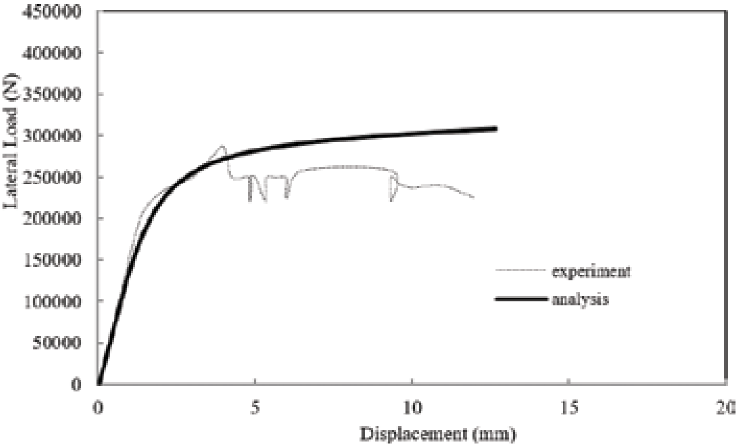

Figure 23. Lateral load-displacement responses for URM 6.

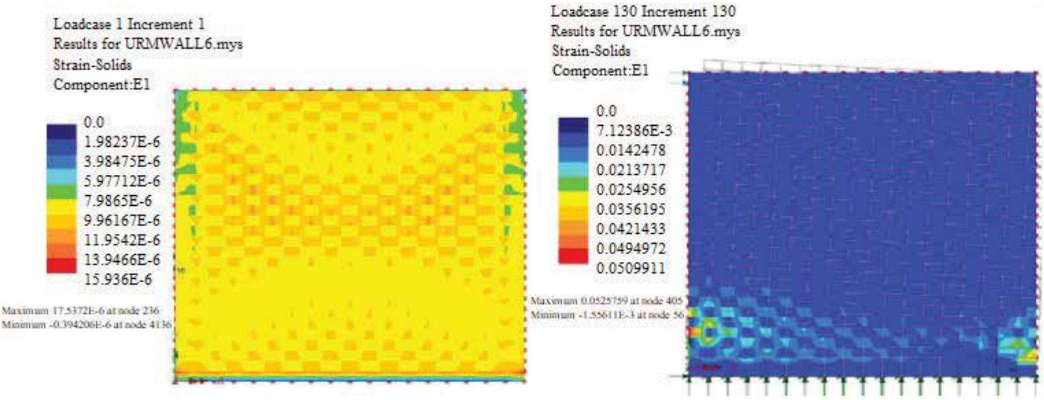

Figure 24. Maximum strains along the wall height (URM 6).

The load-displacement plot obtained from NLFEA is well agreed with the experimental data. As shown in **Figure 21**, the analysis is terminated upon reaching the maximum tensile strain corresponding to the tensile strength of FRP at a horizontal drift of 8.20 mm. This value is experimentally determined approximately as 8.00 mm. The critical tensile strain is calculated as 0.038. As the lateral load is increased, the effect of tensile deformations grows up along the toe of the wall and it is easy to observe the critical tensile strain at the toe of the wall from **Figure 21**.

Haider [29] investigated the behavior of clay brick masonry walls under a combination of vertical preloading, and lateral shear loading (**Figure 22**). Mechanical and geometrical properties of brick and mortar are given in **Table 3**. Compressive strength of clay brick and mortar were 15.7 and 5.00 MPa, respectively. For the case of clay brick masonry wall, the end point for the

FEA is determined defining a discontinuity surface between two brick units along the thickness of the mortar. The maximum tensile strain can be found as 0.061. Load-displacement curve obtained from NLFEA and experimental data is given in **Figure 23**.

As shown in **Figure 24**, the analysis is terminated upon reaching the maximum tensile strain at a horizontal drift of 13.00 mm. Experimental value is approximately as 12.40 mm. The effect of tensile deformations grows up along the toe of the wall under increasing lateral load and the critical tensile strain is observed at the toe of the wall (**Figure 24**).

4. Conclusions

This chapter deals with the implementation of the plasticity theory to URM and FRP-strengthened masonry walls under compression and shear by considering the constitutive behavior of masonry units, mortar, and FRP composite material separately. A DP-type yield criterion is also employed relating the cohesion and the internal friction angle of both unit and mortar to their uniaxial compressive strength by extending the previous approach to the FRP-strengthened masonry walls. For this purpose, a large parametric study is performed in order to explain the mechanical properties of unit and mortar with only a single parameter, that is, their uniaxial compressive strength [24]. In order to evaluate the accuracy of the proposed approach, the analytical results are compared with the experimental results of both unreinforced and strengthened masonry walls tested in two different experimental studies. Following conclusions are drawn:

1. The analytical approach previously recommended for masonry columns for the cohesion and internal friction angle have been updated and extended to the analysis of FRP-strengthened URM walls. The behavior of URM as well as the FRP-confined masonry walls simulated by means of the proposed approach considering these analytical relations is consistent with the test results.
2. Elasto-plastic analyses need an ending-point definition to terminate NLFEA when the stress-strain curve has an ideal plastic plateau. For the case of URM wall, the end point is determined defining the discontinuity surface between two clay units along the thickness of the mortar. It is possible to calculate the maximum strain ε_1 by dividing the mortar thickness by two block heights plus the mortar thickness. FEA should be interrupted when the ultimate tensile strain at the wall reaches this value. For the case of strengthened walls with FRP, FEA can be interrupted when the ultimate tensile strain reaches the rupture strain, $\varepsilon_{rup} = f_t/E_{FRP}$. For the analyses of both the strengthened walls which are previously tested and damaged ones, and the employment of FRP strips which confines only to one side of the wall partially, the use of the maximum tensile strain criterion of masonry seems much more reasonable.
3. Cohesion and internal friction values of the masonry units are expressed in terms of hydrostatic pressure at the failure and their uniaxial compressive strength. The relations of masonry constituents are recommend are valid for $\xi/f_{mu} < 0.58$. The dependency of the material parameters of the frictional materials on the hydrostatic pressure is then reflected into the analysis directly.

4. The material parameters of DP criterion are expressed in terms of the cohesion and the internal friction angle of MC criterion in this study. Therefore, the surfaces of both DP and MC yield criteria are made to coincide along the compression meridian.

Nomenclature

c	cohesion
c_{mr}	cohesion of mortar
E_{bl}	modulus of elasticity of the blocks
E_{br}	modulus of elasticity of bricks
E_m	modulus of elasticity
E_{mr}	modulus of elasticity of the mortar
f_{bl}	compressive strength of the blocks
f_{br}	compressive strength of bricks
f_l	confining pressure exerted by FRP
f_{mr}	compressive strength of the mortar
f_{mu}	uniaxial compressive strength of the unit
h_{br}	height of the unit
h_{mr}	height of the mortar thickness
I_1	first invariant of the stress and the deviatoric tensor
J_2	second invariant of the stress and the deviatoric tensor
k	material constant
p	vertical pre-compression of the wall
α	material constant
ε_{max}	maximum tensile strain
ξ	hydrostatic component of the current stress state
ϕ	internal friction angle
ϕ_i	initial angle of internal friction in radians
ϕ_f	final angle of internal friction in radians
ϕ_{mr}	internal friction angle of mortar
σ_m	mean stress

Author details

Bilge Doran[1]*, Hasan Orhun Köksal[2], Selen Aktan[2], Oktay Jafarov[3] and Cengiz Karakoç[4]

*Address all correspondence to: doranbilge@gmail.com

1 Yıldız Technical University, Istanbul, Turkey

2 Çanakkale Onsekiz Mart University, Çanakkale, Turkey

3 WorleyParsons Baku Office, Azerbaijan

4 Boğaziçi University, Istanbul, Turkey

References

[1] Köksal HO, Aktan S, Kuruşçu AO. Elasto-plastic finite element analysis of FRP-confined masonry columns. Journal of Composites for Construction. 2012;**16**(4):407-417. DOI: 10.1061/(ASCE)CC.1943-5614.0000268

[2] Hamid AA, Chukwunenye AO. Compression behavior of concrete masonry prisms. Journal of Structural Engineering. 1986;**112**(3):605-613. DOI: 10.1061/(ASCE)0733-9445(1986)112:3(605)

[3] Cheema TS, Klingner RE. Compressive strength of concrete masonry prisms. Journal of the American Concrete Institute. 1986;**83**(1):88-97

[4] Khalil MRA, Shrive NG, Ameny P. 3 dimensional stress-distribution in concrete masonry prisms and walls. Magazine of Concrete Research. 1987;**39**(139):73-82. DOI: 10.1680/macr.1987.39.139.73

[5] Ganesan T, Ramamurthy K. Behavior of concrete hollow-block masonry prisms under axial-compression. Journal of Structural Engineering. 1992;**118**(7):1751-1769. DOI: 10.1061/(ASCE)0733-9445(1992)118:7(1751)

[6] Ramamurthy K. Behavior of grouted concrete hollow block masonry prisms. Magazine of Concrete Research. 1995;**47**(173):345-354. DOI: 10.1680/macr.1995.47.173.345

[7] Sayed Ahmed EY, Shrive NG. Nonlinear finite-element model of hollow masonry. Journal of Structural Engineering. 1996;**122**(6):683-690. DOI: 10.1061/(ASCE)0733-9445(1996)122:6(683)

[8] Köksal HO, Doran B, Ozsoy AE, Alacalı SN. Nonlinear modeling of concentrically loaded reinforced blockwork masonry columns. Canadian Journal of Civil Engineering. 2004;**31**(6):1012-1023. DOI: 10.1139/l04-058

[9] Köksal HO, Karakoç C, Yıldırım H. Compression behavior and failure mechanisms of concrete masonry prisms. Journal of Materials in Civil Engineering. 2005;**17**(1):107-115. DOI: 10.1061/(ASCE)0899-1561(2005)17:1(107)

[10] Shing PB, Lofti HR, Barzegarmehrabi A, Brunner J. Finite-element analysis of shear resistance of masonry wall panels with and without confining frames. Proceedings of the Tenth World Conference on Earthquake Engineering. 1992:2581-2586

[11] Köksal HO, Karakoç C. An isotropic damage model for concrete. Materials and Structures. 1999;**32**(222):611-617. DOI: 10.1007/BF02480497

[12] Köksal HO, Arslan G. Damage analysis of RC beams without web reinforcement. Magazine of Concrete Research. 2004;**56**(4):231-241. DOI: 10.1680/macr.2004.56.4.231

[13] Köksal HO, Jafarov O, Doran B, Aktan S, Karakoç C. Computational material modeling of masonry walls strengthened with fiber reinforced polymers. Structural Engineering and Mechanics. 2013;**48**(5):737-755. DOI: 10.12989/sem.2013.48.5.737

[14] LUSAS Finite Element System, Version 14.5-2. FEA Ltd, Surrey. UK; 2011

[15] Dhanasekar M, Page AW, Kleeman PW. A finite element model for the in-plane behavior of brick masonry. Proceedings of the 9th Australasian Conference on Mechanisms of Structures. 1984:262-267

[16] Ganz HR, Thurlimann B. Strength of brick walls under normal force and shear. Proceedings of the 8th International Symposium on Load Bearing Brickwork. London, U.K; 1983

[17] Lourenco PB. Computational strategies for masonry structures [Ph.D. thesis]. Civil Engineering and Geosciences. Eindhoven, Netherland: Delft University; 1996

[18] Chaimoon K, Attard MM. Modeling of unreinforced masonry walls under shear and compression. Engineering Structures. 2007;**29**(9):2056-2068. DOI: 10.1016/j.engstruct.2006.10.019

[19] Giambanco G, Rizzo S, Spallino R. Numerical analysis of masonry structures via interface models. Computer Methods in Applied Mechanics and Engineering. 2001;**190**(49-50):6493-6511. DOI: 10.1016/S0045-7825(01)00225-0

[20] Lourenco PB, Rots JG. Multisurface interface model for analysis of masonry structures. Journal of Engineering Mechanics. 1997;**123**(7):660-668. DOI: 10.1061/(ASCE)0733-9399(1997)123:7(660)

[21] Formica G, Sansalone V, Casciaro R. A mixed solution strategy for the nonlinear analysis of brick masonry walls. Computer Methods in Applied Mechanics and Engineering. 2002;**191**(51-52):5847-5876. DOI: 10.1016/S0045-7825(02)00501-7

[22] Milani G. 3D FE limit analysis model for multi-layer masonry structures reinforced with FRP strips. International Journal of Mechanical Sciences. 2010;**52**(6):784, 004-803. DOI: 10.1016/j.ijmecsci.2010

[23] Grande E, Milani G, Sacco E. Modelling and analysis of FRP-strengthened masonry panels. Engineering Structures. 2008;**30**(7):1842-1860. DOI: 10.1016/j.engstruct.2007.12.007

[24] Jafarov O. Lifli Polimerle Güçlendirilmiş Yığma Duvarların Modellenmesi [Ph.D. thesis]. Istanbul: Civil Engineering, Yıldız Technical University; 2012

[25] Stratford T, Pascale G, Manfroni O, Bonfiglioli B. Shear strengthening masonry panels with sheet glass-fiber reinforced polymer. Journal of Composites for Construction. 2004;**8**(5):434-443. DOI: 10.1061/(ASCE)1090-0268(2004)8:5(434)

[26] Capozucca R. Experimental analysis of historic masonry walls reinforced by CFRP under in-plane cyclic loading. Composite Structures. 2011;**94**(1):277-289. DOI: 10.1016/j.compstruct.2011.06.007

[27] Rahman A, Ueda T. Numerical simulation of FRP retrofitted laterally loaded masonry. Eleventh North American Masonry Conference. Minneapolis; 5-8 June 2011

[28] Mosallam A, Banerjee S. Enhancement in in-plane shear capacity of unreinforced masonry (URM) walls strengthened with fiber reinforced polymer composites. Composites: Part B. 2011;**42**(6):1657-1670. DOI: 10.1016/j.compositesb.2011.03.015

[29] Haider W. In plane responce of wide spaced reinforced masonry shear walls [Ph.D thesis]. Emerald, Australia: Central Queensland University; 2007

[30] Krstevska L, Tashkov LJ, Arun G, Aköz F. Evaluation of seismic behavior of historical monuments. SHH07 International Symposium on Studies on Historical Heritage Symposium Book. Antalya, Turkey; 2007. pp. 411-418

[31] Mele E, De Luca A, Giordano A. Modelling and analysis of a basilica under earthquake loading. Journal of Cultural Heritage. 2003;**4**(4):355-367. DOI: 10.1016/j.culher.2003.03.002

[32] Berto L, Saetta A, Scotta R, Vitaliani R. An orthotropic damage model for masonry structures. International Journal for Numerical Methods in Engineering. 2002;**55**(2):127-157. DOI: 10.1002/nme.495

[33] Tasnimi AA, Farzin M. Inelastic behavior of RC columns under cyclic loads, based on cohesion and internal friction angle of concrete. Modarres Technical and Engineering Journal. 2006;**23**:29-40

[34] Mohebkhah A, Tasnimi AA, Moghadam HA. Nonlinear analysis of masonry-infilled steel frames with openings using discrete element method. Journal of Constructional Steel Research. 2008;**64**(12):1463-1472. DOI: 10.1016/j.jcsr.2008.01.016

[35] Popehn JRB, Schultz AE, Lu M, Stolarski HK, Ojard NC. Influence of transverse loading on the stability of slender unreinforced masonry walls. Engineering Structures. 2008;**30**(10):2830-2839. DOI: 10.1016/j.engstruct.2008.02.016

[36] Buhan P, Felice G. A homogenization approach to the ultimate strength of brick masonry. Journal of the Mechanics and Physics of Solids. 1997;**45**(7):1085-1104. DOI: 10.1016/S0022-5096(97)00002-1

[37] Milani G, Lourenco PB, Tralli A. Homogenised limit analysis of masonry walls, part I: Failure surfaces. Computers & Structures. 2006;**84**(3-4):166-180. DOI: 10.1016/j.compstruc.2005.09.005

[38] Brasile S, Casciaro R, Formica G. Finite element formulation for nonlinear analysis of masonry walls. Computers & Structures. 2010;**88**(3-4):135-143. DOI: 10.1016/j.compstruc.2009.08.006

[39] Köksal HO, Doran B, Turgay TA. Practical approach for modeling FRP wrapped concrete columns. Construction and Building Materials. 2009;**23**(3):1429-1437. DOI: 10.1016/j.conbuildmat.2008.07.008

[40] Doran B, Köksal HO, Turgay T. Nonlinear finite element modeling of rectangular/square concrete columns confined with FRP. Materials & Design. 2009;**30**(8):3066-3075. DOI: 10.1016/j.matdes.2008.12.007

[41] Mohamad G, Lourenco PB, Roman HR. Mechanical Behavior Assessment Of Concrete Block Masonry Prisms Under Compression. International Conference on Concrete for Structures. Coimbra, Portugal; 2005. p. 261-268

[42] Kaushik HB, Rai DC, Jain SK. Stress-strain characteristics of clay brick masonry under uniaxial compression. Journal of Materials in Civil Engineering. 2007;**19**(9):728-739. DOI: 10.1061/(ASCE)0899-1561(2007)19:9(728)

[43] Chen WF, Han DJ. Plasticity for Structural Engineers. New York: Springer-Verlag; 1988. p. 600

[44] Maïolino S, Luong MP. Measuring discrepancies between coulomb and other geotechnical criteria: Drucker-Prager and Matsuoka-Nakai. 7th EUROMECH Solid Mechanics Conference. Lisbon, Portugal; 7-11 September 2009

[45] Chen WF, Lui EM. Structural Stability: Theory and Implementation. New York: Elsevier; 1987. p. 486

[46] Haach VG, Vasconcelos G, Lourenco PB. Influence of the geometry of units and filling of vertical joints in the compressive and tensile strength of masonry. Special Issue of Materials Science Forum. 2010;**636-637**:1321-1328. DOI: 10.4028/www.scientific.net/MSF.636-637.1321

[47] Marcari G, Fabbrocino G, Manfredi G, Prota A. Experimental and numerical evaluation of tuff masonry panels shear seismic capacity. 10th North American Masonry Conference. St. Louis, USA; 2007

[48] La Mendola L, Failla A, Cucchiara C, Accardi M. Debonding phenomena in CFRP strengthened Calcarenite masonry walls and vaults. Advances in Structural Engineering. 2009;**12**(5):745-760. DOI: 10.1260/136943309789867872

[49] Rahman A, Ueda T. In-plane shear performance of masonry walls after strengthening by two different FRPs. Journal of Composites for Construction. 2016;**20**(5):1-14. DOI: 10.1061/(ASCE)CC.1943-5614.0000661

Chapter 2

Finite Element Modeling of Masonry Infill Walls Equipped with Structural Fuse

Ali M. Memari and Mohammad Aliaari

Additional information is available at the end of the chapter

http://dx.doi.org/10.5772/intechopen.77307

Abstract

Masonry infill walls in multi-story buildings are intended to function as envelope and partition walls, and without sufficient gaps between the infill and the frame, the infill tends to contribute to lateral seismic load resistance, which can lead to damage. By isolating the infill walls from the frame, vulnerability to damage will be reduced; however, the potential benefit from the strength and stiffness of the infill walls will be lost too. The compromise solution seems to be a controlled engagement of the masonry infill walls by employing a structural fuse concept. In this chapter, initially, a review of the literature on seismic performance of masonry infill walls is presented. This is then followed by explanation of the concept of the masonry infill structural fuse. Then a discussion on experimental tests carried out on different types of fuse elements as well as ¼ scale specimen of frame and infill walls with fuse elements is presented. Finally, the results of finite element computer modeling studies are discussed. The study has found that the concept of using structural fuse elements as sacrificial components in masonry construction is practical and can be given consideration for more refined design and detailing toward practical application.

Keywords: masonry, infill, seismic, fuse, modeling

1. Introduction

Masonry bearing wall systems were the predominant structural systems prior to the use of framed structures. Once steel and concrete framing systems replaced bearing wall systems, especially for multistory buildings, masonry walls were then used as infill walls (**Figure 1**) to provide the envelope and partition wall functions. Besides such functions, the role of masonry infill walls in seismic resistance of buildings has long been well recognized. In fact, because of participation of masonry infill walls in resisting lateral seismic loads, infill walls and/or their framing systems can sustain damage with life-safety hazard potential [1, 2].

Traditionally, masonry infill walls are specified by architects as exterior envelope walls, backup walls for veneer systems, or interior partition walls. Such construction does not carry gravity load from floors and only carries its own weight. Depending on the details of joints between the edges of infill walls and infilled frames, the interaction between the infill wall and frame can adversely affect the seismic behavior of the structure (e.g., [3, 4]). In most cases, the small gaps between the infill wall and the structural frame are infilled with caulking and in some cases with mortar [5]. This tight-fit construction (**Figure 2**) engages the infill wall in in-plane lateral load resistance [6]. Depending on whether the wall is solid (complete infill) or the existence of large openings that make the infill wall partial infill, the wall's interaction with confining

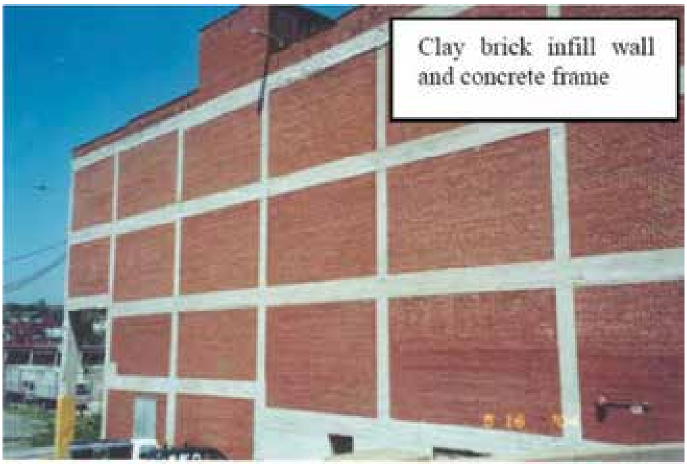

Figure 1. Examples of masonry infill wall in a reinforced concrete frame building [Photo by Ali M. Memari].

Figure 2. Example of a tight-fit masonry infill wall construction [Photo by Ali M. Memari].

frames could possibly lead to premature column failure as a result of short column effect or to increased levels of ductility demand in columns. Furthermore, because these tight-fit infill walls essentially behave as shear walls, their distribution in plan could increase torsional moments and create structural irregularities, if not placed symmetrically. The manner infill walls resist lateral loads is much like a compression brace, and the cyclic interaction of this effective brace with structural frame connection may lead to either the failure in the masonry and/or damage to the beam-column connection. Tight-fit construction of infill walls, whether of partial height or full height can lead to extensive damage to walls, columns, or beam-column joints. Besides the life-safety hazard that such damage will pose, in terms of financial loss, infill wall damage and subsequent repair/replacement work can seriously challenge building owners and tenants.

In order to avoid damage to infill walls, columns, or joints, the use of gaps between the infill wall and the frame is one alternative as shown in **Figures 3** and **4**. Providing gaps between the infill wall and the confining frame is a building code requirement (e.g., [7]) if the infill wall is not designed as part of the lateral force-resisting system, that is, if it is a nonparticipating infill. On the other hand, if the in-plane isolation joints are not large enough to satisfy the conditions

Figure 3. Example of partition infill wall isolated from the frame with small gaps: (a) beam-column joint area and (b) gap between column and infill wall [Photo by Ali M. Memari].

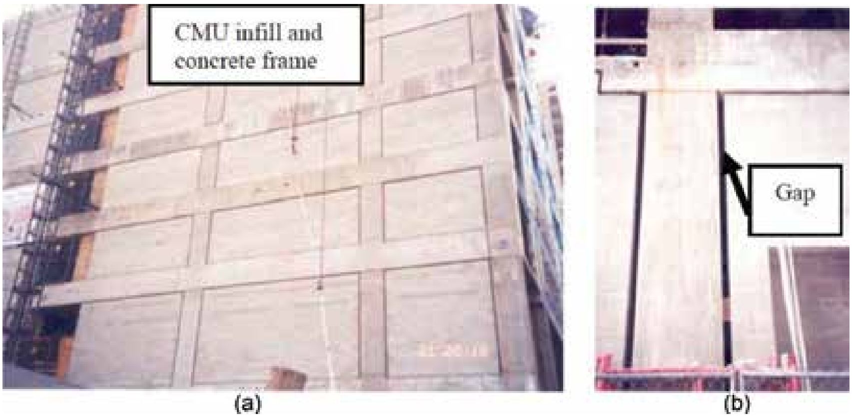

Figure 4. Use of large gaps between infill backup wall and frame in a Seattle building: (a) view of several stories of the building and (b) close-up view of gaps between column and infill walls [Photo by Ali M. Memari].

for nonparticipating infills, then the infill wall is considered as part of the primary lateral force-resisting system, that is, participating infill, and it must be designed as a shear wall, which complicates design and construction and is not typically desirable by designers. For isolation of infill walls, small gaps (e.g., 9.5 mm–12.7 mm) are usually provided, which are then filled with caulking or other deformable fillers. **Figure 3** shows an example of an infill wall construction with isolated joints from the frame with small gaps. In more seismically active areas, larger gaps are usually provided, as shown in the example of **Figure 4**, which shows a large gap between concrete masonry unit (CMU) infill wall and reinforced concrete frame. This particular infill wall was, however, intended to function as the backup wall for brick veneer exterior skin. In general, when such a gap is to be provided, the gap size should exceed the expected interstory drift, which is determined either by structural analysis, or as the maximum allowable value specified in the building code.

Providing large gaps for partition wall applications will cause its own challenging issues with respect to fire safety and sound transmission issues for which the architect and designers should recommend appropriate solutions. Providing small gaps in general will not have the scale of the problems of large gaps. However, under moderate-to-strong earthquakes, the gap openings will likely approach the upper limit for story drift ratios of building codes such as ASCE 7–16 [8]. For instance, for a Risk Category II building with allowable story drift ratio of 2%, the upper limit will be nearly 75 mm for a 3750 mm story height. In that case, once the gap opening is overcome by the frame story drift, the columns will then bear against the infill wall, and under cyclic-type oscillations, the infill wall and/or frame members can sustain damage. It is the responsibility of the designer to assure the sufficiency of the gap size, and if it is desirable to keep the gap size small, the designer will have to increase the size or number of frame members designated as part of the lateral-force-resisting system, which could translate to substantial increase in construction cost.

By isolating the infill wall from the frame and avoiding their interaction in buildings with moment-resisting frames as their primary lateral force-resisting system, damages to infilled frames, failure of infill walls, and potential life-safety hazards can be avoided. However, in that case, the building is deprived of the potential benefit from the strength and stiffness that masonry infill walls can offer even if they are not designed as shear walls. It should be noted that even unreinforced masonry walls inherently possess considerable stiffness that can be properly and advantageously employed in lateral force resistance.

One shortcoming of this isolation option is that the beneficial effects of the masonry infill in stiffening and strengthening the structural frame system will not be employed. In general, since the masonry infill walls are heavy and greatly increase the effective seismic weight of the building, it would be logical to engage them also in lateral load resistance. However, it is the potential damage to these brittle components that designers wish to avoid. The compromise solution seems to be a controlled engagement of the masonry infill walls by employing a structural fuse concept. Such an idea is based on desirability of employing beneficial effects of strength and stiffness of infill walls to reduce story drifts during seismic events up to certain controlled levels. Under strong shaking, when the interaction force between the infill wall and the frame exceeds a certain level, it is desirable to isolate the infill wall from the frame in order to avoid damage to the wall or the frame. This function is provided by using a structural fuse.

In this chapter, preliminary studies on this concept are reviewed. Initially, the concept of the masonry infill structural fuse is explained. This is followed by discussion of experimental tests on different types of fuse elements. Next, the pilot experimental studies employing a one-fourth scale frame and infill walls with fuse are reviewed. The results of computer-modeling studies are then presented followed by recommendations for additional follow-up studies that need to be undertaken.

2. Background and literature review

There has been over 60 years of research on infill walls. The following references are mentioned as chronological representative examples of the experimental and analytical studies done over the past six decades: [2, 5, 9–48]. Even after such extensive international efforts, there is still room for enhanced understanding and design considerations of masonry infill wall interaction with structural frame.

The consensus among researchers is that it is wise to use the beneficial properties of the infills in design if their strength and stiffness characteristics can be relied on. The masonry design code, ACI 530–13/ASCE 5–13/TMS 402–13 [7], provides design guidelines for infill walls

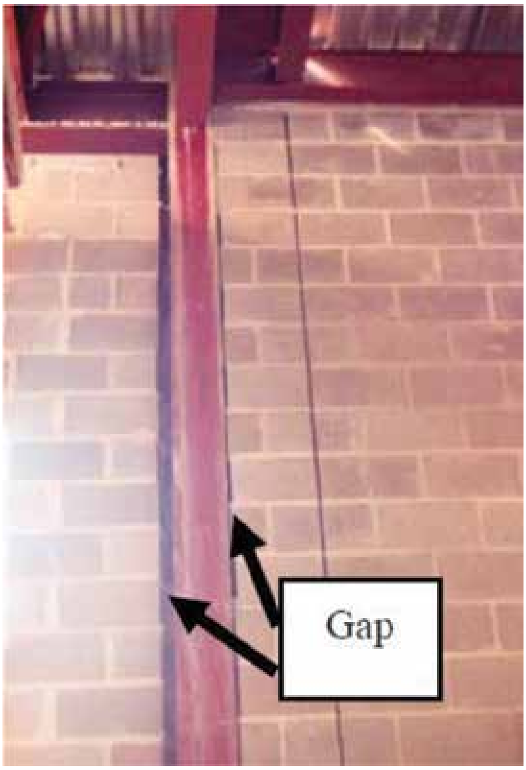

Figure 5. Use of different size gaps in a building [Photo by Ali M. Memari].

in Appendix B. The current code offers two sets of prescriptive design guidelines, one for masonry walls not considered participating in lateral force-resistance, and the other for walls that are expected to take part in lateral force resistance. For the latter group, masonry standards joint committee (MSJC) 2013 code requires these walls to be designed as shear walls, which necessitates use of sufficient reinforcement and detailing to satisfy in-plane and out-of-plane flexural and shear effects. According to the code, for the former group *B2.1.1: In-plane isolation joints shall be designed between the infill and the sides and top of the bounding frame., B2.1.2: In-plane isolation joints shall be specified to be at least 3/8 in. (9.5 mm) wide in the plane of the infill, and shall be sized to accommodate the design displacements of the bounding frame., B2.1.3: In-plane isolation joints shall be free of mortar to contain resilient material, provided that the compressibility of that material is considered in establishing the required size of the joint.* In practice, sometimes gaps of different sizes are provided (most likely not by design but because of construction issues) between the infill and the frame as shown in **Figure 5** in a building.

3. Development of a fuse element for masonry infill walls

In search of ways to find an alternative solution so that the infill wall can participate in lateral load resistance and provide additional stiffness for wind loading and low-to-moderate seismic events, but to disengage (be isolated) under major events, a fuse concept was introduced [49]. **Figure 6** shows the concept of a structural fuse placed between the infill wall and

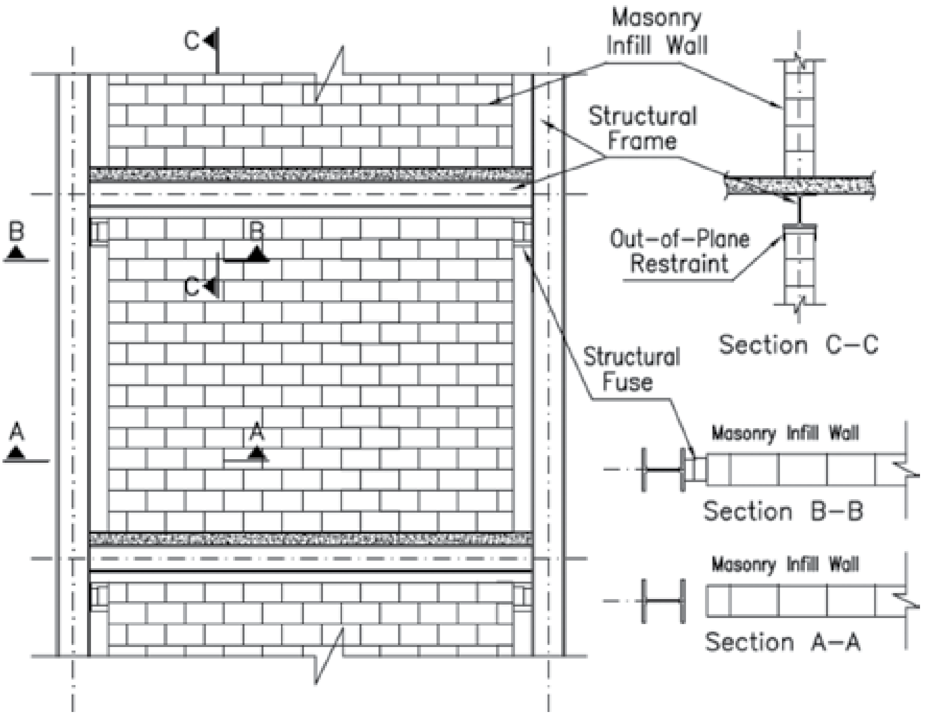

Figure 6. Schematic representation of fuse elements in a masonry infill wall [53].

structural frame. The fuse element is placed as a masonry unit (or part of it). Depending on the fuse element material and mechanism design, it can have stiffness and damping properties and it could be a single rigid-brittle element or a rigid-ductile element.

Pilot tests were carried out to investigate the concept and the feasibility of using such a fuse for infill walls [50–52]. A few different materials and mechanisms were studied to develop a potentially acceptable fuse element. The concept of a disk and a punching or penetrating rod was developed. In this concept, a disk of concrete or wood will be used as the breakable fuse element as shown in **Figure 7**. The fuse element types shown in **Figure 7** perform in a rigid manner up to their punching capacity, beyond which the interaction between the frame and the infill wall stops. In other words, when the fuse is installed between the top of the infill wall and the frame columns, the infill wall is engaged in lateral load resistance, but when the fuse breaks at the threshold design load of the fuse, the infill wall no longer offers resistance to lateral movement of the frame.

Another pilot study used rigid wood disks on a one-fourth scale three-story two-bay frame as shown in **Figure 8**. The pilot study investigated a rigid fuse element that worked only under compression. **Figure 8** shows how a wood disk breaks when its ultimate capacity is reached. The size of the gap between the infill walls and the frame shown in **Figure 8** was chosen for convenience of experimental study. For real applications in buildings, the fuse-holding mechanism will be placed in the location of an edge masonry unit, and therefore, normal gap

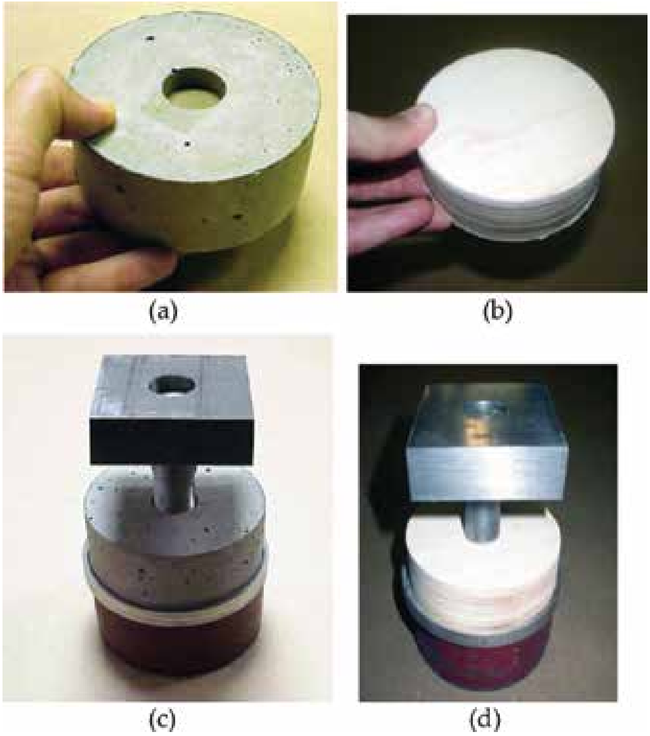

Figure 7. Rigid fuse element with concrete and wood disk alternatives: (a) concrete disk; (b) wood disk; (c) engagement of steel rod on concrete disk; (d) engagement of steel rod on wood disk [53].

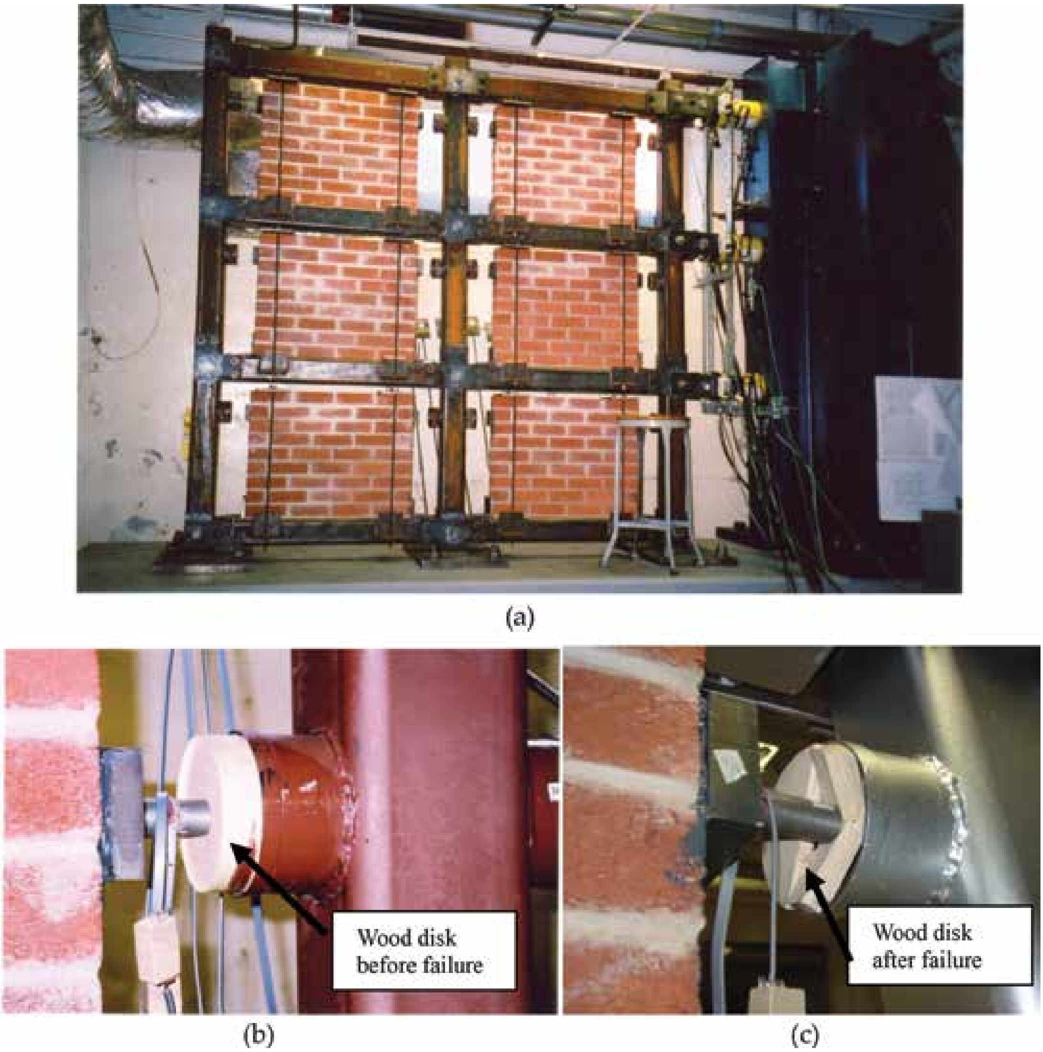

Figure 8. Test results on one-fourth scale frame and infill wall with wood disk fuses: (a) one-fourth scale experimental setup; (b) steel rod tightened against wood fuse; and (c) steel rod puncturing wood fuse [53].

sizes can be used. Furthermore, the out-of-plane movement of the infill wall can be restricted using different available mechanisms as appropriate to a given design.

The process of pilot study leading to the test specimen shown in **Figure 8** consisted of initially developing load-deformation relations for isolated disk element to obtain the average capacities. Then isolated masonry walls were tested under in-plane shear loading to determine their capacities. Finally, the fuse disks were chosen such that they will break prior to masonry infill shear capacity. The detail of the experimental study is explained in Ref. [53]. In this chapter, only the computer-modeling aspect of masonry infill walls equipped with rigid-brittle structural fuse elements is presented. The objective of this chapter is to discuss development of a finite element model for the system (infill-fuse-frame) and validate it by using the results of tests on masonry infill walls (without fuse) available in the literature. In the process of developing the finite element modeling, initially a single-bay, single-story steel frame with tightly fitted infill wall that has been studied by others was modeled. Once the single-bay, single-story model was validated using existing literature results, the model was subjected to monotonic push-over loading as well as cyclic loading under different load-control and displacement-control parameters. The presentation also includes discussion of a parametric study. Practical design approaches and guidelines for masonry infill walls equipped with the proposed structural fuse element and variation of masonry type for the fuse concept are presented in Refs. [54, 52].

4. Development of the finite element model for fuse-equipped infill wall

In the finite element model, material nonlinearities were considered because of nonlinear moment-rotation and force-deformation responses of steel frame connections, equivalent infill wall struts, tie-down anchors, and the fuse element. Large deformation and geometrical nonlinearities existed due to movements and contact between infill wall and frame. In this study, ANSYS finite element analysis program [55] was employed. Five different finite element types from ANSYS element library were used for modeling. The uniaxial BEAM3 element with compression, tension, and bending modeling capabilities was used to model the frame members. PLAIN42 element was used to model the masonry infill wall. CONTACT12 element was employed to model the interaction between infill and frame, and COMBIN39 spring element was considered to model the diagonal strut representing the masonry infill and rotational spring representing beam-column joint. Finally, COMBIN40 element was used to model the proposed structural fuse component.

To model a bare steel frame, BEAM3 element with three degrees of freedom (two translations and one rotation) at each node was used. PLAIN42 element with four nodes and two translational degrees of freedom per node was used as a plane stress element to model the infill wall. COMBIN39 element with two nodes and with up to three translational degrees of freedom per node can be used as a unidirectional element (e.g., uniaxial compression-tension element or purely rotational spring). The longitudinal option with two degrees of freedom per node was used to model the diagonal struts to represent effective infill and also tie-down rebars. The rotational option was used to represent the frame's beam-column connection. CONTACT12 element with two nodes and two translational degrees of freedom at each node was considered to model a gap between two surfaces, which can be in compression contact or at no contact and may also slide relative to each other considering Coulomb friction. This element was used to model the interaction between infill wall and frame when equipped with fuse. When there is interaction between the two surfaces, the normal stiffness and tangential (shear) stiffness may be active. A negative normal force represents contact between the two surfaces through a linear spring, while a positive normal force means lack of contact. On the other hand, when there is a negative force and the tangential force is less than the product of the normal force and friction coefficient, the two surfaces do not slide freely and are governed by the tangential spring stiffness. However, the two surfaces slide when the tangential force equals that product. COMBIN40 element is a special element to provide stiffness and damping to one side of a gap modeled in series. This two-node element with one degree of freedom per node (e.g., translational or rotational) can be specialized for different applications by appropriate assignment of values for spring stiffness coefficients, damping coefficient, mass value, gap size, and a limiting sliding force.

From the result of a comprehensive review of experimental and analytical studies on infill wall systems [22], an appropriate specimen was chosen for development of finite element modeling in this work. The approach for finite element model validation consisted of initially modeling the bare steel frame, then adding brace elements following methods in Refs. [56] (single-diagonal strut model) and [57] (three-diagonal strut model). The last step in developing the model was to add fuse elements.

One of the specimens in the tests in Ref. [58] on single-bay, single-story steel frame with CMU infill walls (labeled WD7) was chosen for finite element modeling. The specimens selected are described in detail in Ref. [22]. Lateral load was applied to the frame at the top. Specimen WD7 [58] included CMU infill wall with standard horizontal bed joint reinforcement constructed without any gaps between the infill and the steel frame. Load-deflection diagram for the specimen is shown in **Figure 9** including the bare frame and infilled frame tests. The figure also shows analysis results discussed subsequently.

The bare frame was modeled as shown in **Figure 10(a)** using the finite elements as explained in the previous section. The trilinear moment-rotation relationship proposed in Ref. [57] was

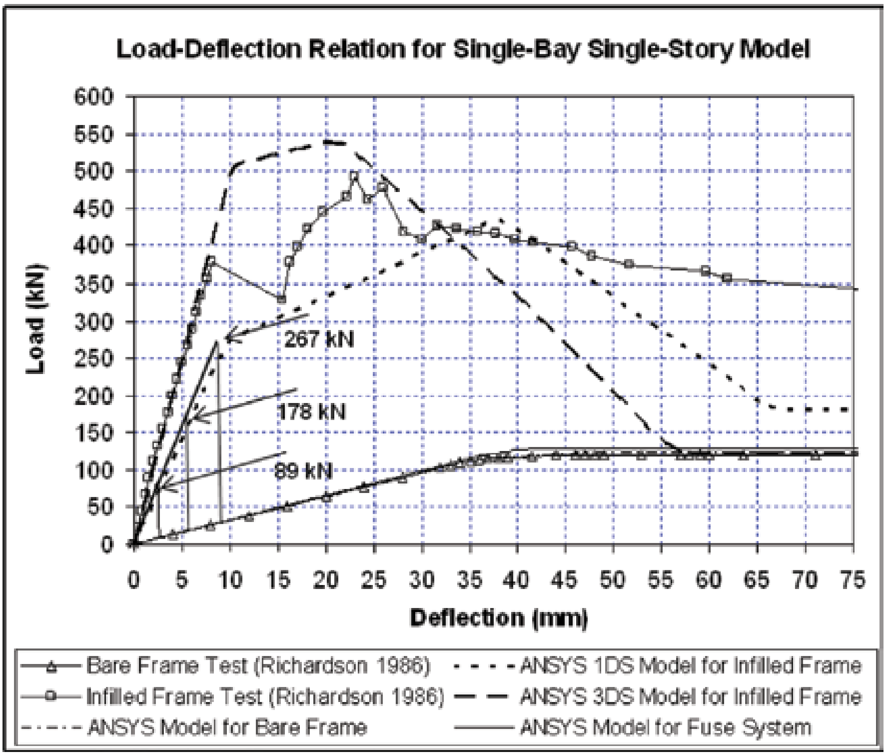

Figure 9. Load-deflection relation for single-bay, single-story system [53].

used for the beam-column joints. The load–displacement diagram for the model when subjected to monotonically increasing displacement was quite close to the experimental results. The bare frame showed to have an initial stiffness of about 3.22 kN/m. The failure mechanism consisted of formation of four plastic hinges in the four beam-column connections, which are represented by rotational springs in the model (**Figure 10(a)**).

The infill wall was modeled initially using the single-diagonal strut model [56] shown in **Figure 10(b)**. This was accomplished by adding a nonlinear diagonal compression strut to the bare frame model. However, the nonlinear rotational springs at the beam-column joint were substituted by frictionless hinges, in order for the diagonal strut to take the entire lateral load. The force-deformation model [56] was used for the strut representing the infill wall. The three-diagonal compression strut [57] shown in **Figure 10(c)** was also used as a second alternative for infill model. The force-deformation models were developed based on equations in Ref. [57] using the geometry and material properties of the modeled specimen (WD7). The infilled

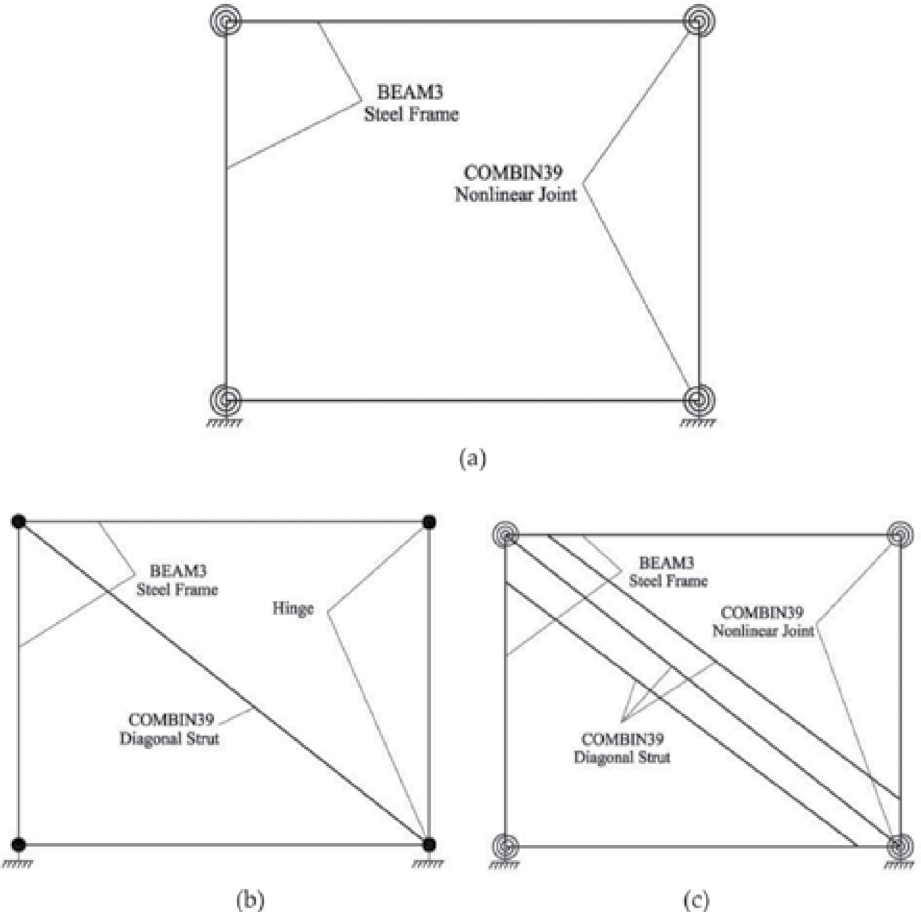

Figure 10. ANSYS models for (a) bare frame; (b) infilled steel frame with single-diagonal strut model; and (c) infilled steel frame with three-diagonal strut model [53].

frame models with the two types of strut models were subjected to monotonically increasing displacement with load-deflection plots compared to the experimental test results shown in **Figure 9**. The results of the two strut models show notable differences which is due to the assumptions made for force-deformation properties of the strut element. The three-diagonal strut model shows closer analytical results to the experimental test results.

The next step in completing the finite element model (shown in **Figure 11**) was to add appropriate fuse elements and hold-down elements. At the location of the fuse element on the columns, two nonlinear rotational springs were added. The final steel frame model shown in **Figure 11** had a total of 33 BEAM3 elements and 6 COMBIN39 elements. The masonry infill wall was, then, modeled with PLAIN42 elements. To model the contact between infill wall and steel frame, CONTACT12 elements were added at top and bottom at each side. The model presented also shows vertical steel rebar hold-downs modeled with COMBIN39 elements with tension force-deformation properties shown in **Figure 12**. The bottom corners of the infill

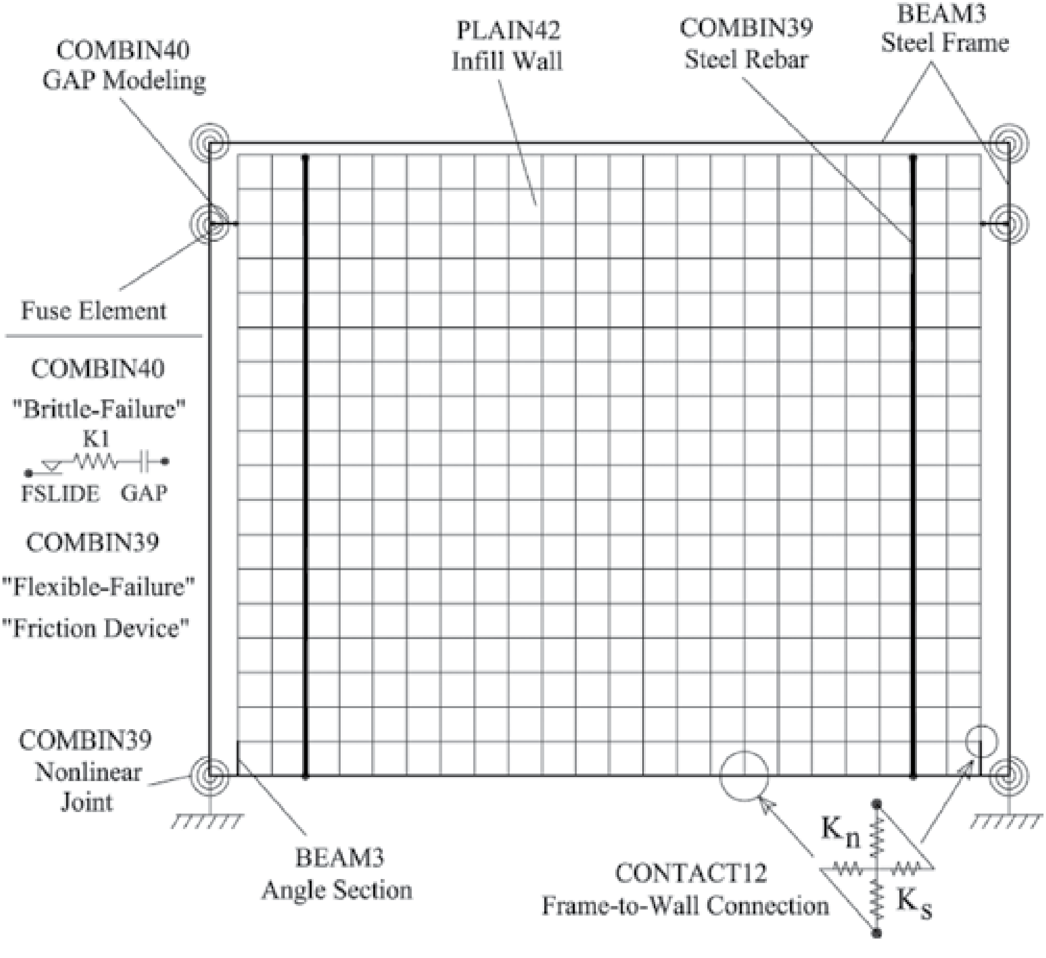

Figure 11. ANSYS model for infilled steel frame with fuse elements [53].

wall were assumed to be in tight fit connection with the columns to provide shear transfer. The micro infill wall modeling required 396 PLAIN42 elements, 27 CONTACT12 elements, and 2 COMBIN39 elements.

The fuse element used in the model is intended to simulate an elastic behavior up to failure or breakage of the element as shown in **Figure 13**. Once the fuse element breaks, there is no force transfer through the fuse element. COMBIN40 element provides the required property, which is transfer of force only in compression. To provide for such behavior, a very small value (0.0025 mm) was assumed for the GAP specification in the element property data. The spring K1 in the COMBIN40 element was determined considering the force-deformation results of the fuse elements pilot tests. COMBIN40 element features "break-away" property appropriate

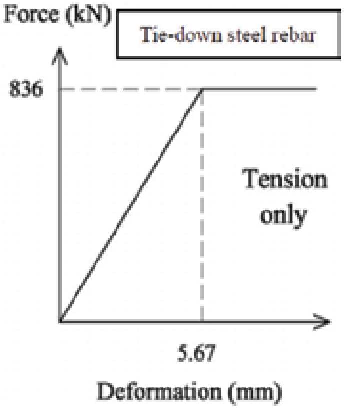

Figure 12. Force-deformation responses for tie-down steel rebar [53].

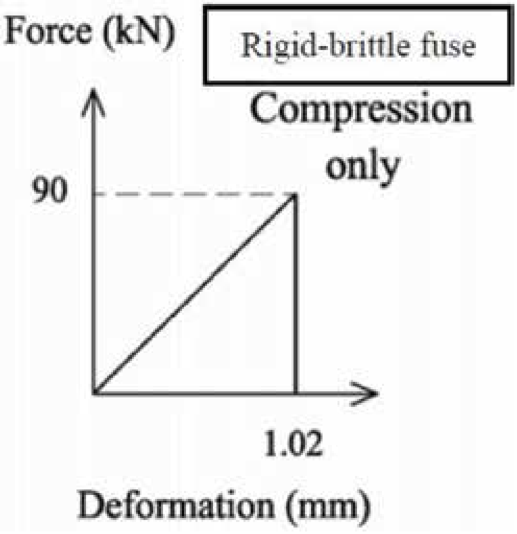

Figure 13. Force-deformation responses for the rigid-brittle fuse element [53].

to simulate the condition of fuse breakage with subsequent zero force in the element, once the fuse capacity is reached. The fuse capacity is a function of the masonry infill wall shear strength. According to test results in Ref. [56], the infill wall had a capacity of 383 kN, which with a factor of safety of 4.0, yields a fuse capacity of 89 kN for the model. This value was used to specify FSLIDE, for which a negative value results in a drop to zero when the force in the element reaches the specified capacity (89 kN), while a positive value represents yielding or constant force equal to the capacity. In this case, only negative value was assigned.

5. Discussion of the single-bay, single-story model analysis results

Pushover analysis of single-bay, single-story infilled frame with fuse element model was carried out to compare the response with infilled frame without fuse element. The results of this analysis are shown in **Figure 9** along with the results from the experimental study of the bare frame and infilled frame. For better clarity, **Figure 14** shows the plot of the initial deflection portions with larger scale. The effect of varying the fuse capacity on the system response is illustrated in **Figure 9** with three different values for the fuse capacity (i.e., 89 kN, 178 kN,

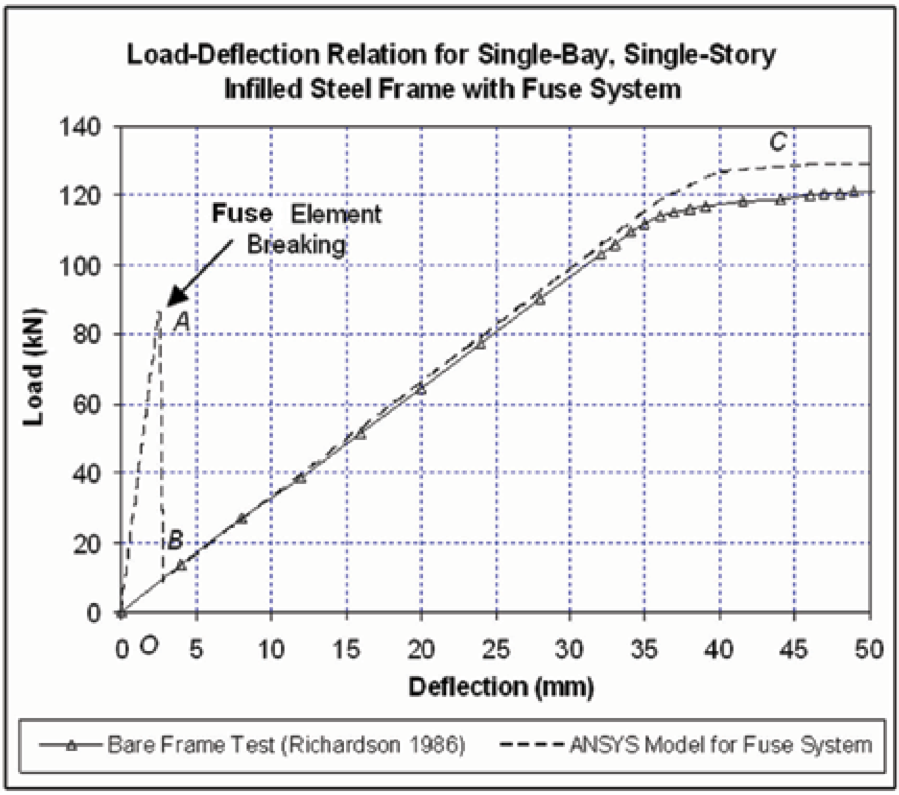

Figure 14. Load-deflection relation for single-bay, single-story model with "brittle-failure" fuse element [53].

and 267 kN). The figure shows two stages of response consisting of (a) prior to breakage of the fuse and (b) after breakage. During the first stage shown by line OA in **Figure 14**, the fuse transfers lateral loads from the frame to the infill wall and as such, the slope of the line OA represents the combined larger stiffness of the steel frame and the masonry infill wall. Upon breakage of the fuse at point A (capacity of fuse), there is sudden drop in the force level, line AB, followed by load-deflection relation along BC, which represents the response of the bare frame. This means that the infill wall is disengaged from the steel frame and only the bare frame is resisting the total load.

Comparison of the response of the model having fuse element with those of the bare frame and infilled frame in **Figure 9** shows that the stiffness of the system with fuse element is slightly smaller than that resulting from tested infilled frame (about 75% of the infilled frame). This, however, is about ten times the stiffness of the bare frame. Although as shown in **Figure 9**, higher strength fuse elements increase the strength capacity of the system, but it should be noted that the objective is to prevent failure of the wall. For example, based on the test results (shown on the figure), the tightly fitted masonry infill wall cracks around a lateral load of 378 kN. The smaller the fuse capacity, the larger will be the margin of safety against cracking.

The fuse element model shown in **Figure 13** describes a condition where upon breakage of the fuse, the force transfer across the fuse becomes zero. Since this could imply a shock-type response, but which is more like cracking of reinforced concrete or masonry system, it is possible to develop fuse elements that show more ductile response. For example, if the fuse element can be described by the trilinear or multilinear models shown in **Figure 15**, the corresponding load deflection plots for the infilled frame will be those shown in **Figures 16** and **17**, which show a more gradual drop of the force across the fuse and a smoother transition to the bare frame condition. It should be noted that depending on the mechanism of failure or design function of the fuse, different types of infilled frame response can be obtained. Examples of such mechanisms could include friction damper mechanism for energy dissipation and enhanced seismic response of the structure.

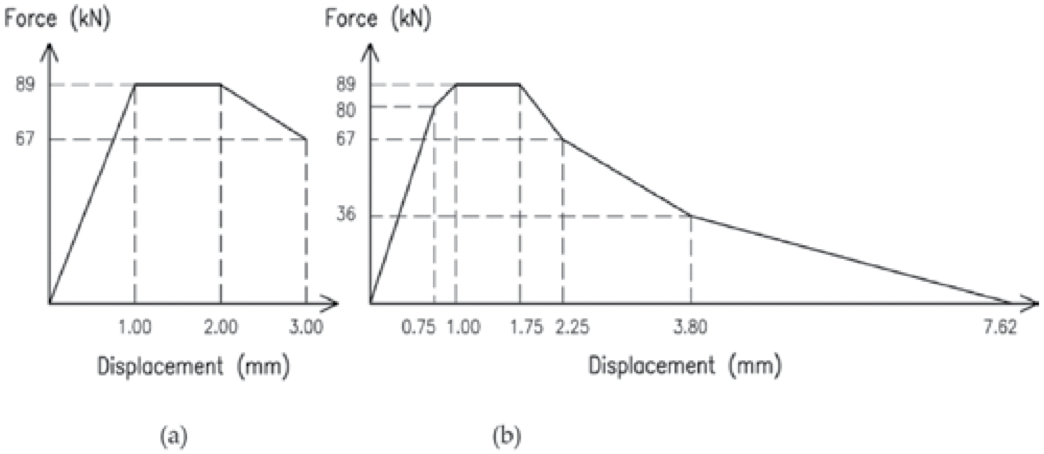

Figure 15. Assumed force-deformation responses for fuse element (a) “trilinear” and (b) “multilinear” [53].

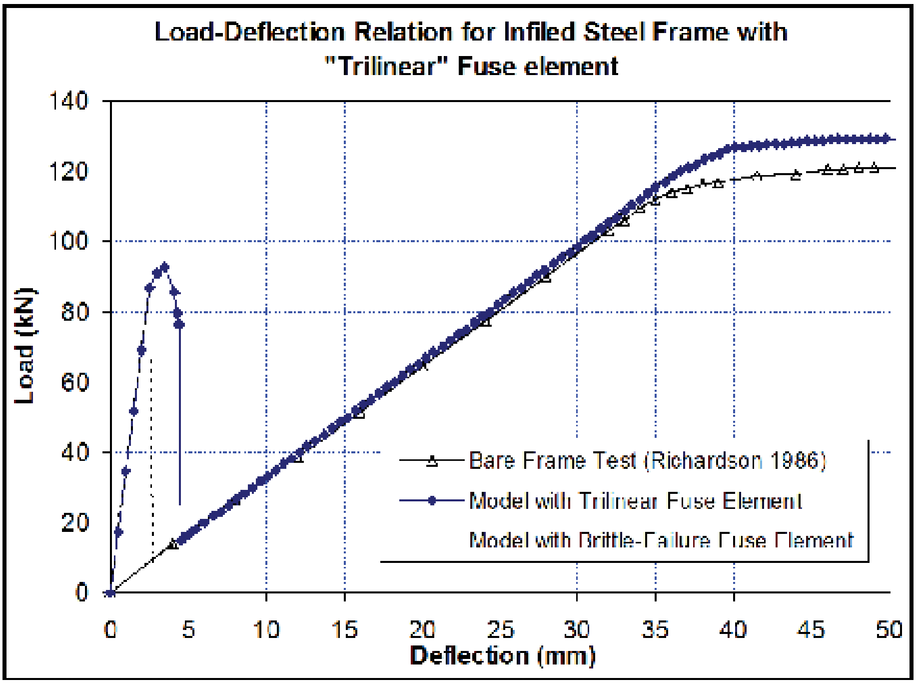

Figure 16. Load-deflection relation for single-bay, single-story case study with "trilinear" response for fuse element [53].

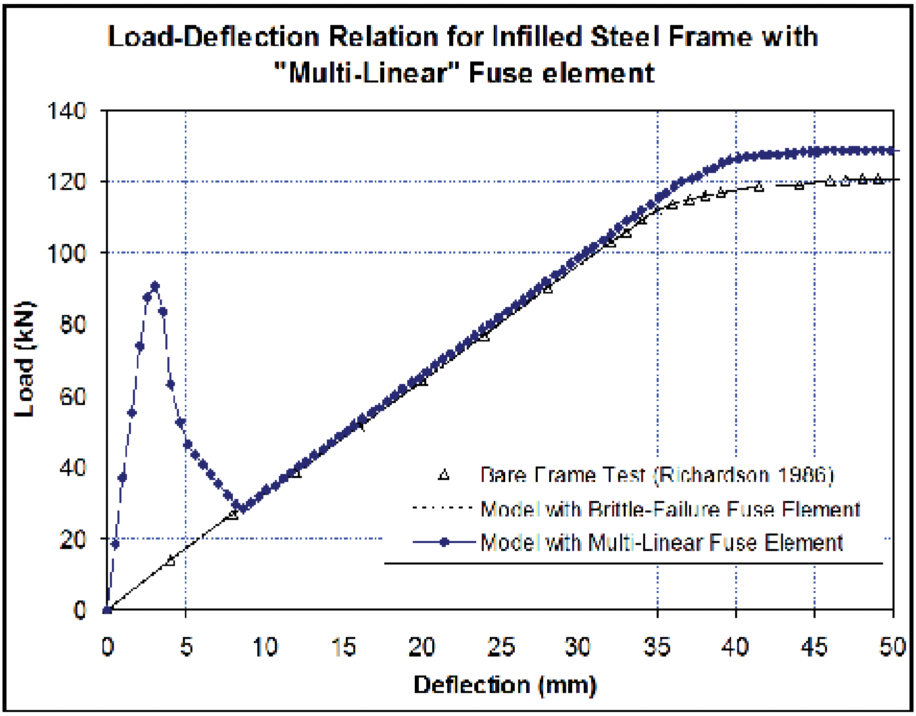

Figure 17. Load-deflection relation for single-bay, single-story case study with "multilinear" response for fuse element [53].

6. Discussion of the two-bay, three-story model analysis results

With the finite element model validated based on the performance of a single-bay, single-story infilled frame, the modeling approach can next be applied to a multi-bay, multistory system. The same modeling features presented in previous sections were used to model the two-bay, three-story frame shown in **Figure 18**. The panel dimensions and material properties were the same as those for the single-bay, single-story case. The steel frame members,

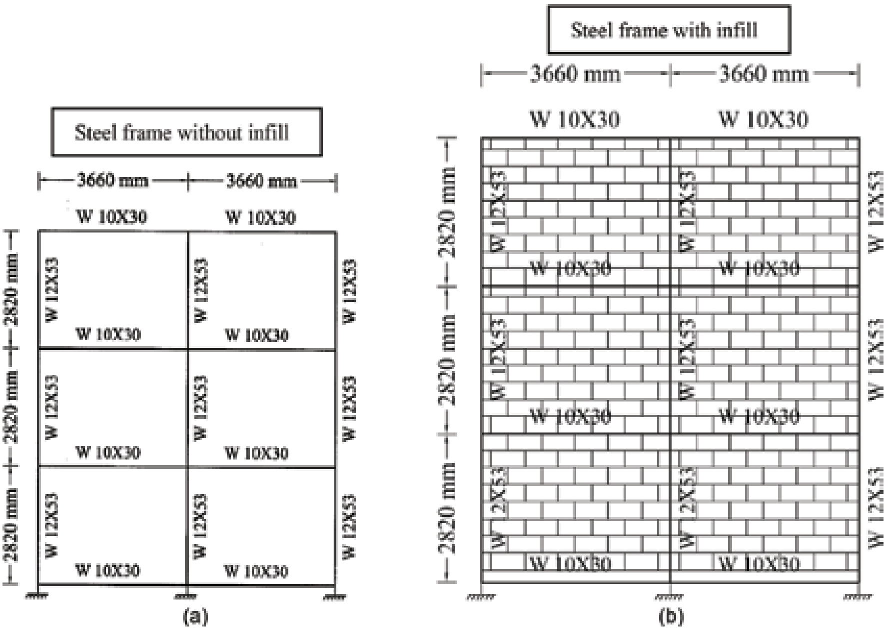

Figure 18. Two-bay, three-story model description [53].

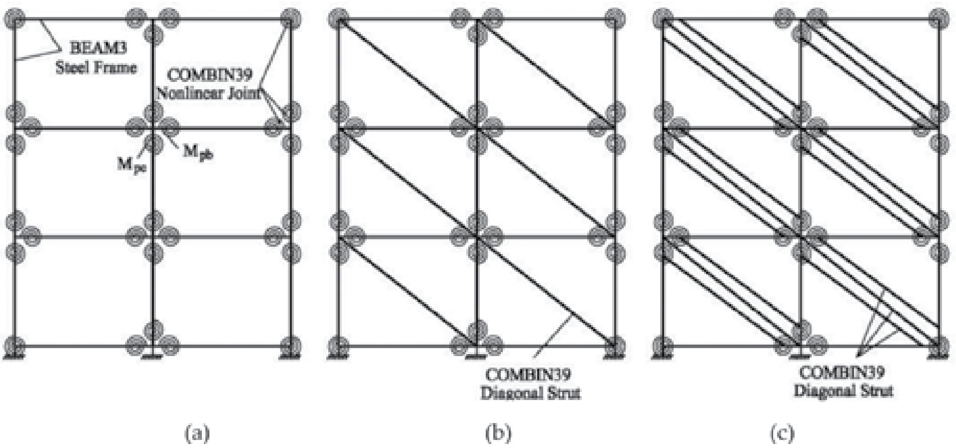

Figure 19. ANSYS models for two-bay, three-story case study: (a) bare steel frame; (b) single-diagonal strut method; and (c) three-diagonal strut method [53].

however, were modified to make them appropriate for a three-story structure. The masonry infill walls were assumed to be conventional CMU blocks (200 mm x 200 mm × 400 mm).

Models were developed for two-bay, three-story systems for three cases of bare frame, infilled frame without fuse, and infilled frame with fuse elements. The bare frame model shown in **Figure 19(a)** employed nonlinear beam-column joints shown in the figure by COMBIN39 elements. The model with masonry infill without fuse shown in **Figure 19(b** and **c)** consisted of two cases of single-diagonal strut and three-diagonal strut representation of the infill wall. **Figure 20** shows the moment-rotation section behavior assumed for beam and column sections. For the single-strut case, the force-deformation behavior model shown in **Figure 21** was used, while for the three-strut case, the models proposed in Ref. [57] were considered. The finite element model for the infilled frame with fuse elements is shown in **Figure 22**, where

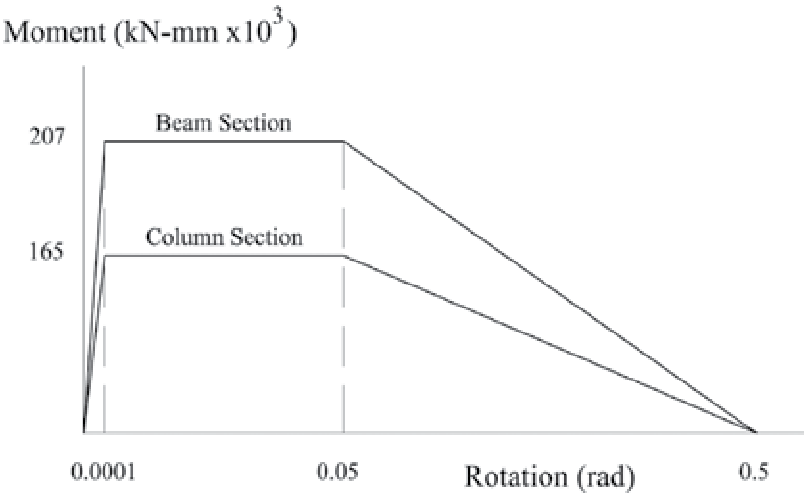

Figure 20. Moment-rotation response for joints [53].

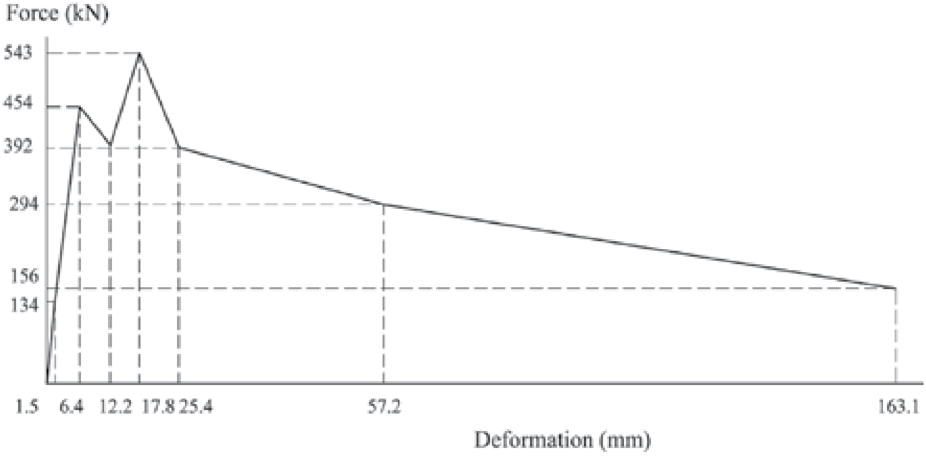

Figure 21. Force-deformation response for diagonal strut of single-diagonal strut model [53].

the elements used consist of 110 BEAM3 elements for the frame, 50 COMBIN30 elements for nonlinear joints, 606 PLAIN42 elements for masonry infill, 108 CONTACT12 elements for wall and frame connections, 12 COMBIN39/40 elements for fuse, 12 COMBIN40 elements for gap modeling, and 12 COMBIN39 elements for tie-downs.

The loading applied to the four models described consisted of imposing incremental horizontal in-plane displacement at the third floor level in a displacement-controlled mode. The resulting load-deflection diagrams for all four models are plotted in **Figure 23**. The results

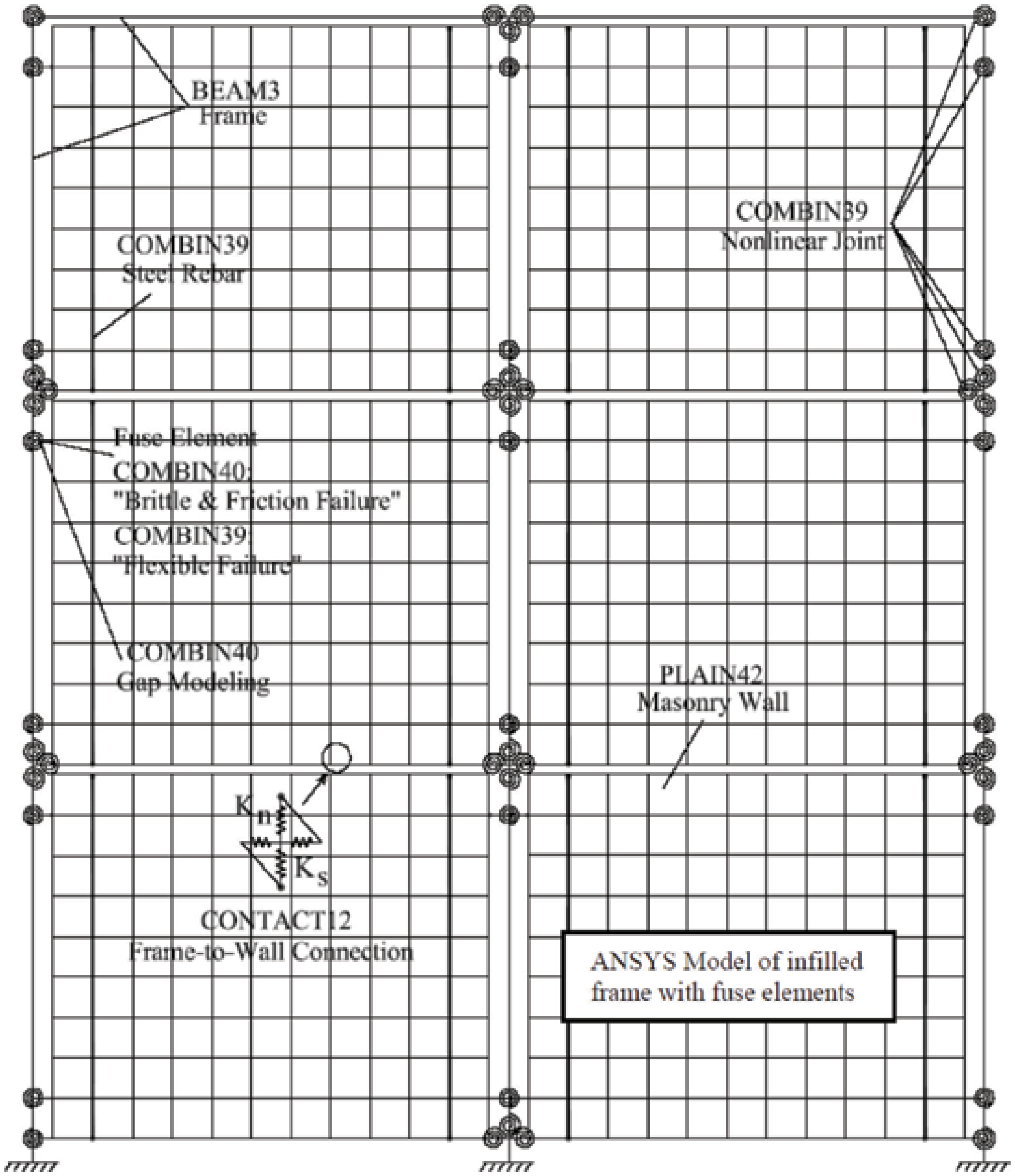

Figure 22. ANSYS model for two-bay, three-story infilled frame with fuse elements [53].

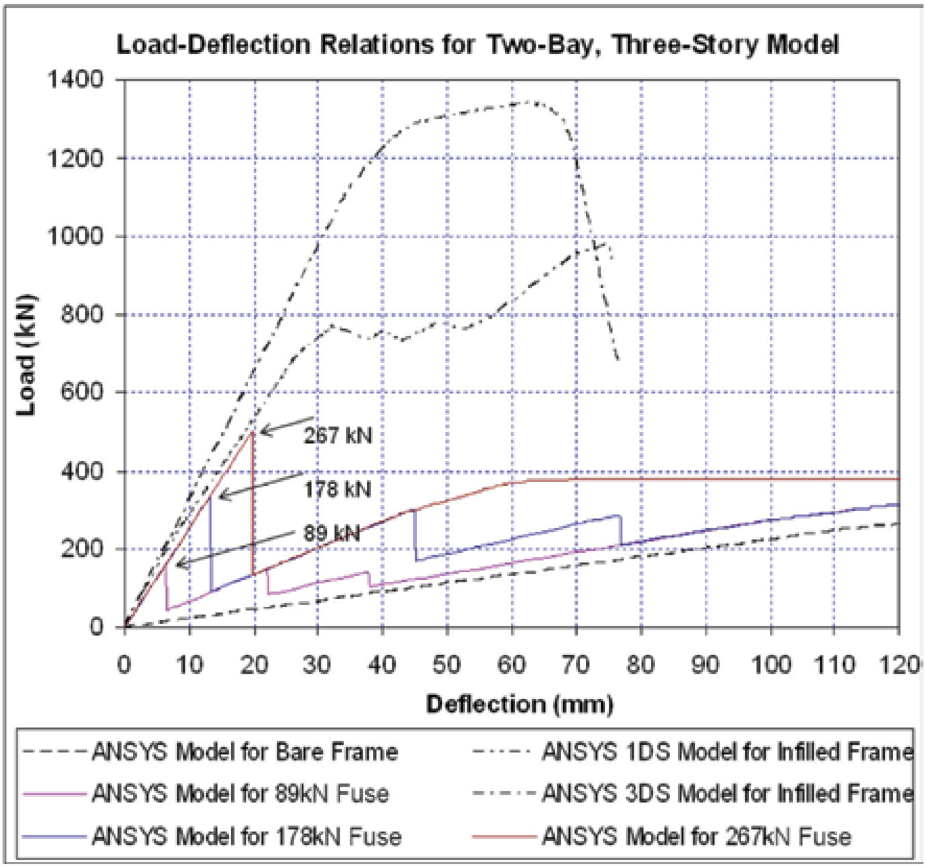

Figure 23. Load-deflection relation for single-bay, single-story system [53].

shown are consistent with the type of response observed for the single-bay, single-story in **Figure 9**. The results for the infilled frame with fuse element are also shown with three different fuse capacities. **Figure 24** shows the enlarged plot of the fuse-equipped system compared to the bare frame model, while **Figure 25** shows the sequence of fuse breakages. As expected, the load-deflection diagram for the system with fuse shows that after the breakage of the last fuse, the response closely follows the bare frame diagram. It should be added that such deflection will continue until the clearance between the frame and the infill wall is overcome, at which point the frame will directly bear against the infill wall, and the overall system will again experience high stiffness due to re-engagement and participation of infill wall.

The displacement-controlled load application is useful to understand the behavior of the system as each fuse breaks, and in general for experimental tests studies to collect detailed data at each displacement increment. To simulate more realistic earthquake loading conditions and also for design purposes, however, load-controlled application can be a better choice. The two-bay, three-story model of the infilled frame with fuse elements was subjected to such a load-controlled case. Consistent with the first-mode deflection and story lateral loads, in-plane loads of F/2, F/3, and F/6 were considered at the third, second, and first floor levels, respectively, and

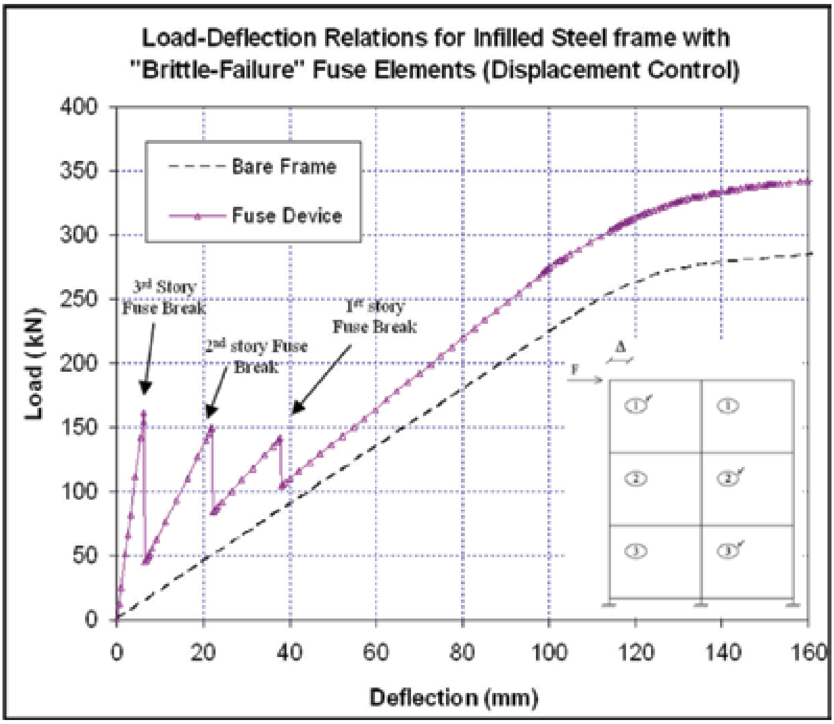

Figure 24. Load-deflection relation for two-bay, three-story infilled steel frame with "brittle-failure" fuse elements [53].

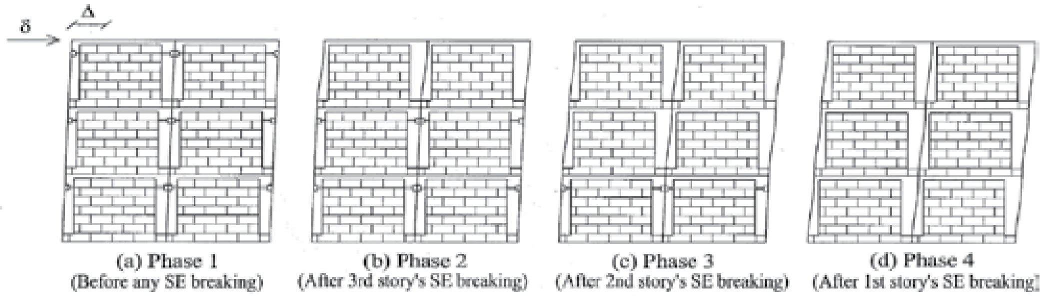

Figure 25. Behavior and failure mechanism of two-bay, three-story infilled steel frame with fuse system [53].

applied incrementally. The resulting load-deflection diagram is shown in **Figure 26** and the sequence of fuse breakage is graphically shown in **Figure 27**. **Figure 26** shows that upon the breakage of the last fuse (third story), the response follows that of the bare frame. The results in **Figure 26** show the beneficial effects of using fuse on increasing the stiffness and thus reducing in-plane deflection. Desirable sequence of fuse failure can be obtained by appropriate distribution of fuses with predetermined varying capacities over the height.

In addition to described analytical studies, parametric studies were conducted to determine the effect of varying the structural frame joint rigidities, member strengths, as well as the

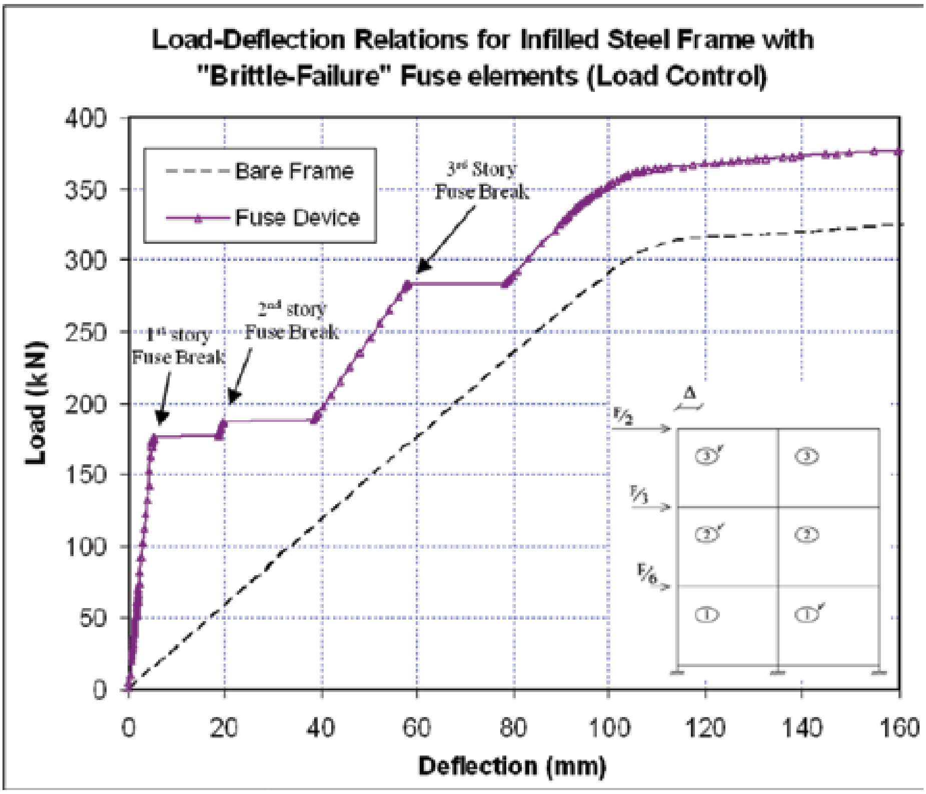

Figure 26. Load-deflection relation for two-bay, three-story infilled steel frame with "brittle-failure" fuse elements (load control) [53].

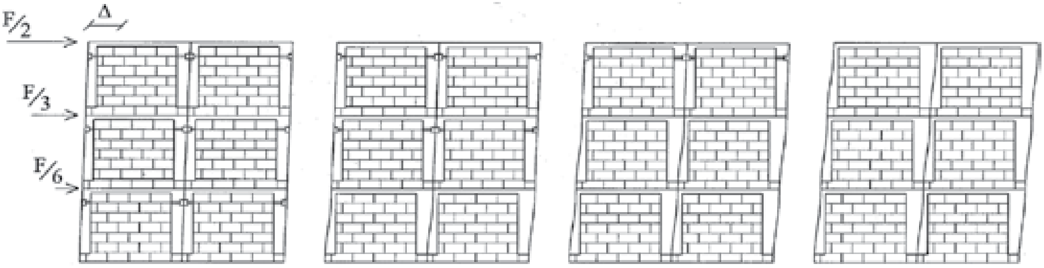

(a) Phase 1
(Before any SE breaking)

(b) Phase 2
(After 1st story's SE breaking)

(c) Phase 3
(After 2nd story's SE breaking)

(d) Phase 4
(After 3rd story's SE breaking

Figure 27. Behavior and failure mechanism of two-bay, three-story infilled steel frame with fuse system (load control) [53].

location and stiffness of fuse elements. The moment-rotation model used for beam-column connection is shown in **Figure 28**, where the initial stiffness is $K_j = M_{pl}/\phi_{el}$. By varying the rotation ϕ_{el} values from 0.0001 rad for a rigid frame to 100 rad for a pinned frame, the effects of joint stiffness on the response were evaluated. The results of the analysis for the two-bay, three-story frame are shown in **Figure 29**, which shows that by reducing the stiffness of the joints, the frame becomes more flexible. However, the effect on fuse performance is minor.

Next, by changing the size of the frame members, for a rigid frame, the member size effect on fuse equipped infilled frame performance were studied. Such behavior for the two-bay, three-story frame with different member sizes is shown in **Figure 30**. The initial design consisted of W12x53 for columns and W10x30 for beams, and the variation includes two cases of heavier and two cases of lighter sections. The results of the analysis show that heavier frame members provide stiffer and stronger system as a whole and that with stronger frames, fuse breaks at lower displacements. The results also show that the strength of the fuse elements should be consistent with that of frame, that is, a frame with higher ultimate load capacity should be used with fuse elements with larger capacity.

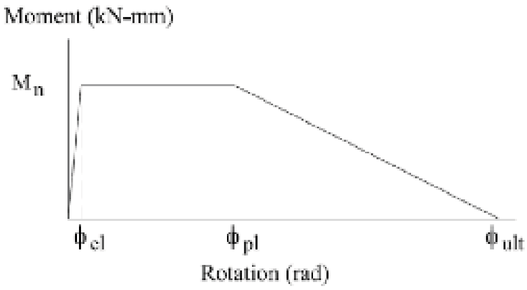

Figure 28. Three-linear moment-rotation response for joints [53].

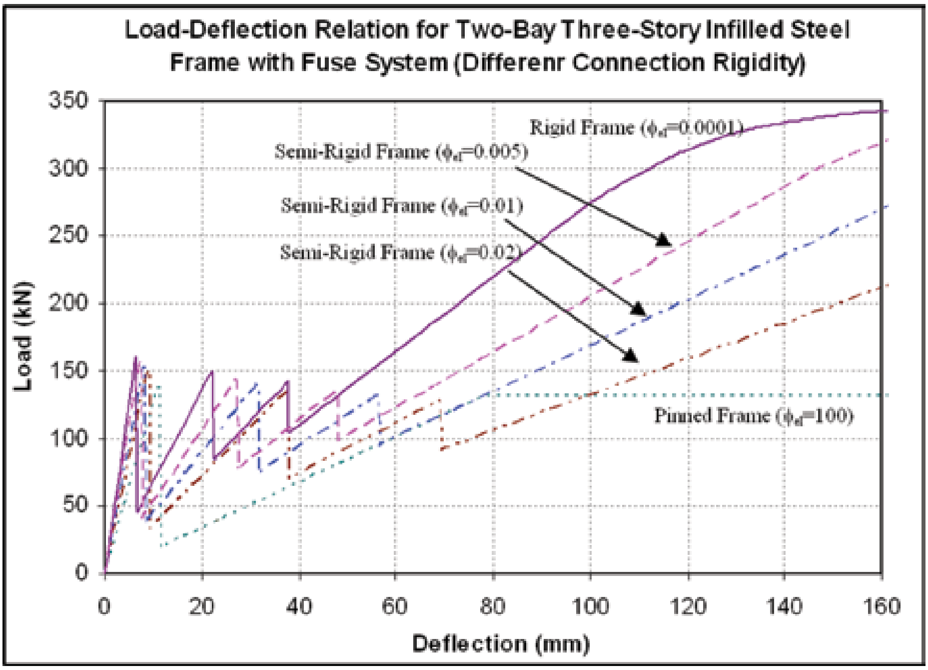

Figure 29. Load-deflection relation for two-bay, three-story infilled steel frame with fuse system with different connection rigidity (stiffness) [53].

Figure 30. Load-deflection relation for two-bay, three-story infilled steel frame with fuse system with different frame Strengths [53].

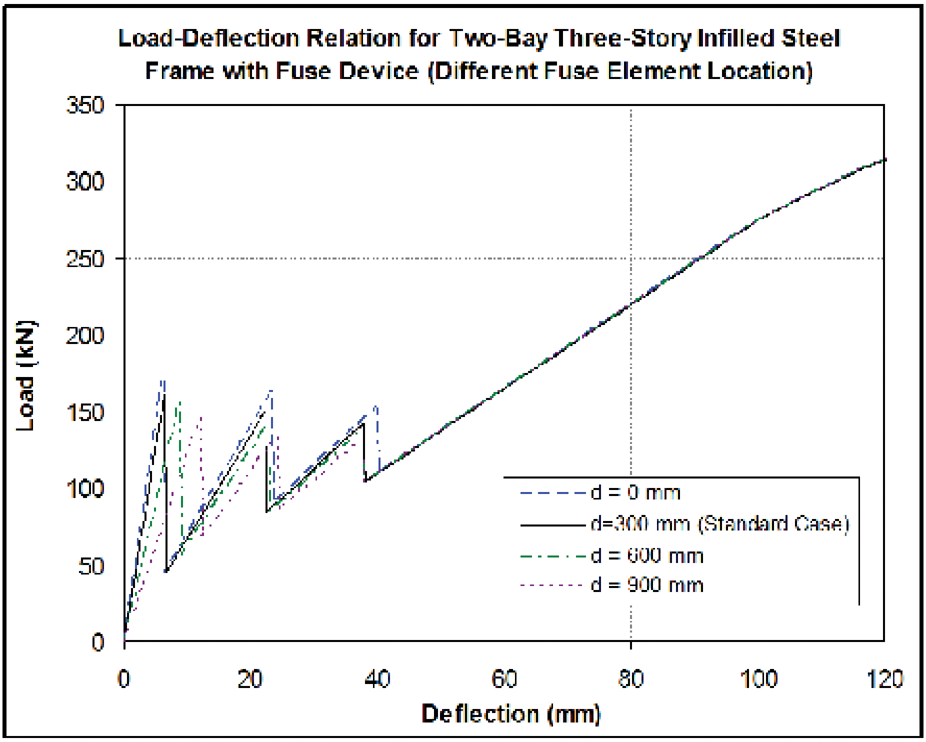

Figure 31. Load-deflection relation for two-bay, three-story infilled steel frame with fuse system with varying location for fuse element [53].

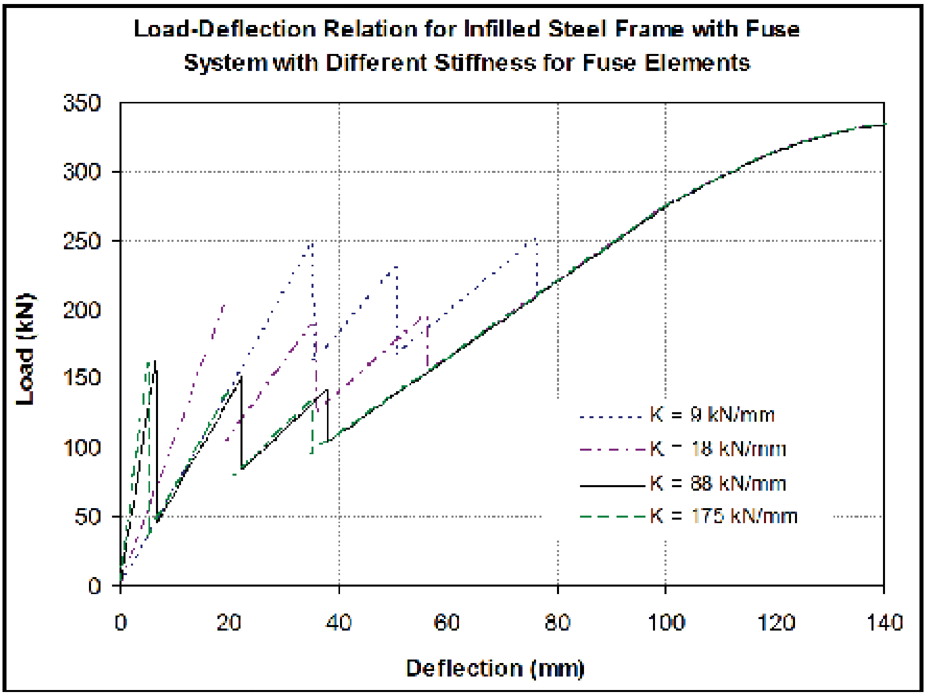

Figure 32. Load-deflection relation for two-bay, three-story infilled steel frame with fuse system with different stiffness for fuse elements [53].

The effect of varying the vertical position of fuse elements with respect to the top of the wall was also examined. Four positions consisting of the wall top corner, 300 mm, 600 mm, and 900 mm below the top corner were chosen. The results of the analysis of the two-bay, three-story frame are illustrated in **Figure 31**, which show that the lower the position of fuse element, the larger the frame drift at fuse breakage points. The results also show that by lowering the position of the fuse, the initial stiffness of the entire system will be reduced and the fuse breaks at larger deflection. It can be concluded that higher positions enhances the effectiveness of the fuse function. Finally, in order to examine the effect of the fuse stiffness on the overall response, four different stiffness values were chosen for fuse elements and the results of the analysis of the two-bay, three-story frame are shown in **Figure 32**, which show that for fuse with lower stiffness, the load and deflection at fuse breakage increases. It can therefore be concluded that the stiffness of the fuse element can have a notable effect on the response of infilled frame.

7. Concluding remarks

The study presented has shown that existing commercial software (such as ANSYS or other similar software) can be used to effectively model complex use of masonry walls. The study has shown how various finite elements can be used to model masonry, structural fuse, as well as infilled frame for analysis under in-plane lateral loading. The available library of finite elements seems to be well-developed for this purpose. Aside from concluding the appropriateness of existing of modeling capabilities to capture various behavioral aspects of masonry infills used in conjunction with fuse elements, some conclusions and remarks can also be mentioned related to the proposed use of fuse concept to mitigate damage to masonry infill walls and/or infilled frames. The concept of using structural fuse elements as sacrificial components in masonry construction is practical and should be given consideration for follow-up R&D studies and more refined design and detailing for practical application. The use of finite element modeling for parametric study of the proposed concept has shown that the effect of frame joint stiffness on the overall mode of behavior is not as much as the stiffness of the frame members. The latter affects the design of the fuse capacity, and for a given frame stiffness, the overall behavior will be sensitive to the fuse capacity. The finite element model analysis also showed that higher positions of the fuse element add efficiency to fuse element performance. While the presented study focused on proof of the concept for masonry infill within steel frames, the concept is equally applicable for concrete frames as well. In fact, variations of the presented concept can be expanded to develop energy dissipating fuse systems for application to steel and concrete frames as well as light frame construction infilled with other materials than masonry.

Author details

Ali M. Memari[1]* and Mohammad Aliaari[2]

*Address all correspondence to: memari@engr.psu.edu

1 Department of Architectural Engineering and Department of Civil and Environmental Engineering, Penn State University, PA, USA

2 IMEG Corporations, Pasadena, CA, USA

References

[1] Ravichandran SS, Klingner RE. Seismic Design Factors for Steel Moment Frames with Masonry Infills: Part 1. Proceedings of the 11th North American Masonry Conference, Minneapolis, Minnesota, June 2011, The Masonry Society, Longmont, CO; 2011

[2] Tucker C. Predicting the In-plane Capacity of Masonry Infilled Frames, Ph.D. Dissertation, Tennessee Technological University; December 2007

[3] Drysdale RG, Hamid AA, Baker LR. Masonry Structures – Behavior and Design. 2nd ed. The Masonry Society; 1999

[4] Paulay T, Priestley MJN. Seismic Design of Reinforced Concrete and Masonry Buildings. Wiley; 1992

[5] Riddington JR. The influence of initial gap on Infilled frame behavior. Proceedings of Institution of Civil Engineers. 1984;**77**:295-310

[6] Klingner RE, Rubiano NR, Bashandy T, Sweeney S. Evaluation and analytical verification of Infilled frame test data. TMS Journal, The Masonry Society. 1997;**15**(2):33-41

[7] Masonry Standards Joint Committee (MSJC). Building code requirements and specification for masonry structures, TMS 402-13/ACI 530/13/ASCE 5-13. In: Longmont, CO. 2013

[8] ASCE. Minimum Design Loads and Associated Criterias for Buildings and Other Structures, ACSE 7-16. Reston, VA: American Society of Civil Engineers; 2016

[9] Benjamin JR, Williams HA. The behavior of one-story brick shear walls. ASCE, Journal of Structural Division. 1958;**84**:1723.1-1723.30

[10] Holmes M. Steel frames with brickwork and concrete infilling. Proceedings, The Institution of Civil Engineers. 1961;**19**:473-478

[11] Stafford-Smith B. Lateral stiffness of Infilled frames. ASCE, Journal of the Structural Division. 1962;**88**(ST6):183-199

[12] Esteva L. Behavior Under Alternating Loads of Masonry Diaphragms Framed by Reinforced Concrete Members. Proceedings, International Symposium on the Effect of Repeated Loading on Materials and Structures, RILEM, Mexico City, Vol. 5; 1966

[13] Mallick DV, Garg RP. Effects of openings on the lateral stiffness of Infilled frames. Proceedings of the Institution of Civil Engineers. 1971;**44**:205-222

[14] Leuchars JM, Scrivener JC. Masonry infill panels subjected to cyclic in-plane loading. Bulletin of New Zealand National Society of Earthquake Engineering. 1976;**9**(2):121-131

[15] Liauw TC, Lee SW. On the behaviour and the analysis of multi story infilled frames subject to lateral loading. Proceedings of The Institute of Civil Engineers, Part 2. 1977; **63**:641-656

[16] Dowrick DJ. Earthquake Resistant Design for Engineers and Architects. 2nd ed. Wiley; 1987

[17] Klingner RE, Bertero VV. Earthquake resistance of Infilled frames. ASCE Journal of Structural Division. 1978;**104**(ST6):973-989

[18] Yanev BS, McNiven HD. Mathematical Modelling of the seismic response of one story steel frame with Infilled partitions. The Canadian Conference on Earthquake Engineering, Montreal, Que. 1979;**2**:828-846

[19] Priestley MJN. Masonry. In: Rosenblueth E, editor. *Design of Earthquake Resistant Structures*. London: Pentech Press; 1980. pp. 195-222

[20] Achyutha H, Jagadish J, Rahman SS. Effect of Contact Between Infill and Frame on the Behaviour of Infilled Multi-story Frames. Proceedings of 6th International Brick Masonry Conference, Rome, Italy; 1982. pp. 574-581

[21] Bertero VV, Brokken S. Infills in seismic resistant building. ASCE, Journal of Structural Engineering. 1983;**109**(6):1337-1361

[22] Dawe JL, Seah CK. Behavior of masonry infilled steel frames. Canadian Journal of Civil Engineering. 1989;**16**:865-876

[23] Manos GC, Mpoufidis D, Demosthenous M, Triamataki M. Influence of Masonry Infill Panels on the Response of R.C. Structures Subjected to Lateral Loads. Proceedings, 5th North American Masonry Conference, Urbana-Champaign, Ill, June 3-6, 1990, pp. 93-104

[24] Hendry AW, Liauw TC. Tests on Steel Frames with Reinforced Masonry Infilling. Proceedings of 3rd International Masonry Conference. The British Masonry Society, London; 1994 pp. 108-114

[25] Sanainejad A, Hobbs B. Inelastic Design of Infilled Frames. ASCE, Journal of Structural Engineering. 1995;**121**(4):634-650

[26] Fardis MN, Calvi MG. Effects of Infills on the Global Response of Reinforced Concrete Frames. In: Duma, editor. Proceedings of 10th European Conference on Earthquake Engineering. Balkema, Rotterdam; 1995. pp. 2893-2898

[27] Combescure D, Pegon P, Anthoine A. Modelling of the in-plane behavior of masonry infill frames. In: Elnashai, editor. European Seismic Design Practice. Balkema, Rotterdam; 1995

[28] Negro P, Verzeletti G. Effect of Infills on the global behavior of R/C frames: Energy considerations from Pseudodynamic tests. Earthquake Engineering and Structural Dynamics. 1996;**25**:753-773

[29] Mehrabi AB, Shing PB. Finite element modeling of masonry-Infilled RC frames. ASCE, Journal Structural Engineering. 1997;**123**(5):604-613

[30] Mosalam KM, White RN, Ayala G. Response of Infilled frames using pseudo-dynamic experimentation. Earthquake Engineering and Structural Dynamics. 1998;**27**:589-608

[31] Chiou Y-J, Tzeng J-C, Liou Y-W. Experimental and analytical study of masonry Infilled frames. ASCE Journal of Structural Engineering. 1999;**125**(10):1109-1117

[32] Flanagan RD, Bennett RM. In-plane behavior of structural clay tile Infilled frames. ASCE Journal of Structural Engineering. 1999;**125**(6):590-599

[33] Fardis MN, Bousias SN, Franchioni G, Panagiotakos TB. Seismic response and design of RC structures with plan-eccentric masonry Infills. Earthquake Engineering and Structural Dynamics. 1999;**28**:173-191

[34] Dorji J. Seismic Performance of Brick Infilled RC Frame Structures in Low and Medium Rise Buildings in Bhutan. Queensland University of Technology: Masters Thesis; 2009

[35] Goel N, Singh Y, Gupta VK. Design aids for performance based design of masonry infills in frame buildings. Springer Journal of Institution of Engineers (India), Civil Engineering Division. May 2009;**90**:7-13

[36] Baird A, Palermo A, Pampanin S, Riccio P, Tasligedik AS. Focusing on reducing the earthquake damage to facade systems. Bulletin of the New Zealand Society for Earthquake Engineering. 2011;**44**(2):108-120

[37] Lu X, Chen Y, Mao Y. New concept of structural seismic design: Earthquake resilient structures. Tongji Daxue Xuebao/Journal of Tongji University. July 2011;**39**(7):941-948. DOI: 10.3969/j.issn.0253-374x.2011.07.001

[38] Asteris PG, Cotsovos DM, Chrysostomou CZ, Mohebkhah A, Al-Chaar GK. Mathematical micromodeling of infilled frames: State of the art. Engineering Structures. 2013;**56**:1905-1921. DOI: 10.1016/j.engstruct.2013.08.010

[39] Jie Ren W, Cheng Ma Z, Qiang Wang Z. Research on seismic behavior of Infilled frame structure. Applied Mechanics and Materials. 2013;**256-259**:2148-2151. DOI: 10.4028/www.scientific.net/AMM.256-259.2148

[40] Quayyum S, Alam MS, Rteil A. Seismic behavior of soft storey mid-rise steel frames with randomly distributed masonry infill. Steel and Composite Structures. 2013;**14**(6):523-545. DOI: 10.12989/scs.2013.14.6.523

[41] Saim R, Khan MKL, Munir F, Anwar W, Hassan S. Seismic performance assessment of masonry Infilled steel frame structures. International Journal of Innovation and Applied Studies (IJIAS). 2014;**8**(4):1470-1484

[42] Wang F, Kang T, Yang Y, Lu S. Seismic behavior of the wall-frame structure infilled with rubber concrete brick. 2015;**31**:661-670. DOI: 10.11717/j.issn:2095-1922.2015.04.11

[43] Bahreini V, Mahdi T, Najafizadeh MM. Numerical study on the in-plane and out-of-plane resistance of brick masonry infill panels in steel frames. Shock and Vibration. 2017;**15**:1-16. DOI: 10.1155/2017/8494657

[44] Keyvani Borujeni A, Mahdi T. Numerical methods in civil engineering nonlinear modeling of the infill wall based on the brittle cracking model. Numerical Methods in Civil Engineering. 2017;**1**(4):7-15

[45] Noorifard A, Mehdizadeh F, Tabeshpour MR. Preventing undesirable seismic behaviour of infill walls in design process. Urbanism. Architecture. Constructions. 2017;**8**(1):57-80

[46] Palios X, Fardis MN, Strepelias E, Stathis SN. Unbonded brickwork for the protection of infills from seismic damage. Engineering Structures. 2017;**131**:614-624

[47] Asteris PG, Sophianopoulos D. Behavior of masonry infilled steel framed structures under strong ground motion; 2018. https://www.researchgate.net/publication/265153004

[48] Yuen TYP, Zhang H-H, Kuang JS, Huang Q. Shake table tests on RC frame infilled by slitted masonry panels. Springer, Bulletin of Earthquake Engineering. 2018. DOI: 10.1007/s10518-018-0339-3

[49] Memari AM, Aliaari M. Seismic infill wall isolator subframe (SIWIS) system for use in buildings. Proceeding, ATC-17-2 Seismic on Response Modification Technologies for Performance-Based Design; Los Angeles, CA; 2002

[50] Aliaari M, Memari AM. Analysis of masonry infilled steel frames with seismic isolator subframes. Engineering Structures Journal. 2005;**27**:487-500

[51] Aliaari M, Memari AM. Experimental evaluation of a sacrificial seismic fuse device for masonry infill walls. ASCE Journal of Architectural Engineering. 2007;**13**(2):111-125

[52] Kauffman AL, Memari AM. Performance evaluation of different masonry infill walls with structural fuse elements based on in-plane cyclic load testing. Buildings. 2014;**4**:605-634. DOI: 10.3390/buildings4040605

[53] Aliaari M. Development of seismic Infill Wall isolator subframe (SIWIS) system PhD Thesis, Pennsylvania State University, University Park, PA; 2005

[54] Aliaari M, Memari AM. Development of a seismic design approach for infill walls equipped with structural fuse. Open Civil Engineering Journal. 2012;**6**(1):249-263

[55] ANSYS Users' manuals – Version 6.1. (2002), ANSYS Inc., Canonsburg, PA

[56] Seah CK. A universal approach for the analysis and design of masonry infilled frame structures. PhD Thesis, Univ. of New Brunswick, Fredericton, N.B., Canada; 1998

[57] El-Dakhakhni WW, Elgaaly M, Hamid AA. Three-strut model for concrete masonry-infilled steel frames. Journal of Structural Engineering, ASCE. 2003;**129**:177-185

[58] Richardson J. The behavior of masonry infilled steel frames. MS Thesis, University of New Brunswick, Fredericton, N.B., Canada; 1986

Section 2

Novel Structural Elements

Chapter 3

Prefabricated Steel-Reinforced Concrete Composite Column

Hyeon-Jong Hwang

Additional information is available at the end of the chapter

http://dx.doi.org/10.5772/intechopen.77166

Abstract

In conventional concrete-encased steel composite columns, a steel section is placed at the center of the cross section. Thus, the contribution of the steel section to the overall flexural capacity of the column could be limited. For better efficiency and economy, particularly under biaxial moment, the steel section needs to be placed at the corners, rather than at the center of the cross section. Recently, a prefabricated steel-reinforced concrete column has been developed to utilize the advantages of the reinforced concrete column and the steel-concrete composite column. In the composite column, four steel angles are placed at the corners of the cross section, and transverse bars and plates are used to connect the angles by welding or bolting. The composite column has been widely applied to industrial buildings that require large sized columns and fast construction. In this chapter, the newly developed composite column is introduced, and basic mechanism, structural performance, and field application case are discussed.

Keywords: metal and composite structures, composite column, steel angle, weld connection, bolt connection, compression test, flexural test, cyclic test

1. Introduction

Nowadays, the demand for huge buildings, long-span structures, and skyscrapers has increased. As a result, (1) sectional performance of compressive members, and (2) fast and safe construction method become important. **Figure 1(a)** shows a conventional concrete-encased steel (CES) composite column using a wide-flange steel section at the center of the cross section. Generally, the wide-flange steel is placed at the center of the cross section, and then longitudinal bars and tie bars are placed in construction site. Thus, the contribution of the steel

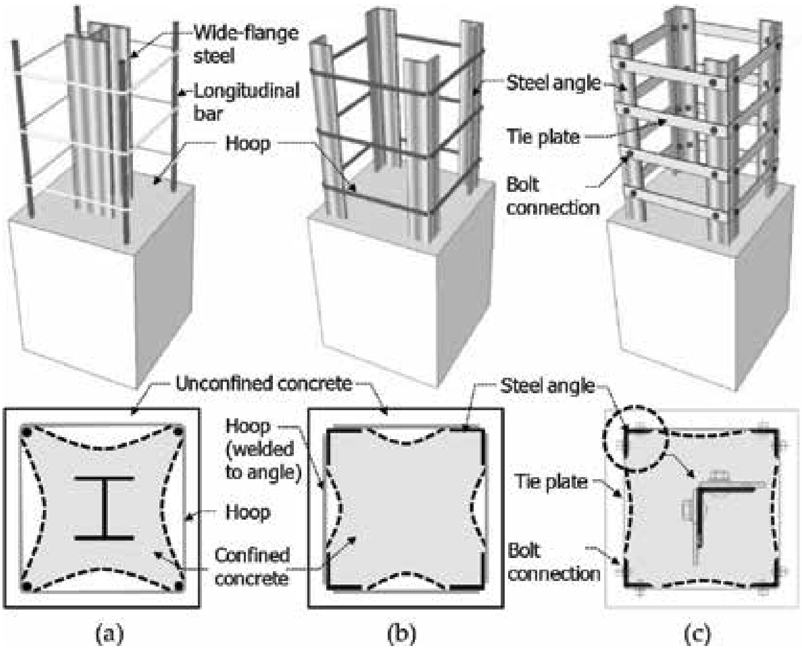

Figure 1. Comparison of CES column and PSRC columns. (a) CES composite column, (b) PSRC composite column (weld connection), (c) PSRC composite column (bolt connection)

section to the overall flexural capacity of the column could be limited. Further, the need for rebar and formwork construction requires considerable construction time. Particularly, in mega structures such as semiconductor factory and warehouse using long and large sized columns, fast and safe construction methods are necessary.

In order to improve structural capacity and cost efficiency, a prefabricated steel-reinforced concrete (PSRC) composite column has been used. As shown in **Figure 1(b)** and **(c)**, the prefabricated steel angles at the four corners replace the conventional wide-flange steel, and the steel angles are weld connected or bolt connected with transverse bars or plates [1–5]. The weld connection should follow the details prescribed in welding standards [6, 7]. The steel angles resist axial load and flexural moment. The transverse bars and plates provide shear resistance, concrete confinement, and bond resistance between the steel angles and concrete. Because the steel cage of angles and transverse reinforcement are prefabricated off site, field rebar work is unnecessary. Further, the self-erectable steel cage can provide sufficient strength and rigidity to support the construction loads of beams and slabs that are superimposed on the PSRC composite column.

Figures 2 and **3** show field application of weld-connected and bolt-connected PSRC composite columns, respectively. Generally, the PSRC composite column with 20 m height and 1.5 m × 1.5 m to 2.0 m × 2.0 m sectional area is used for two- or three-story construction at the same time. In the case of the weld-connected PSRC composite column, the steel cage of angles and transverse reinforcement is moved to construction site, and then concrete form is installed (**Figure 2**). On the other hand, in the case of the bolt-connected PSRC composite column,

Figure 2. Semiconductor FAB (weld-connected PSRC composite column).

Figure 3. Semiconductor FAB (bolt-connected PSRC composite column).

concrete form is preattached to the steel cage and it can be permanently used after concrete pouring (**Figure 3**). Thus, field work related to reinforcing bar placement and concrete form work is excluded, which improves the construction safety and saves the construction time at working in high place.

2. Structural performance of PSRC column

2.1. Contribution of transverse reinforcement

The prefabricated steel angle composite columns strongly depend on the transverse reinforcement that connects the corner steel angles. The transverse reinforcement provides (1) shear transfer between the steel angles, (2) bond between the steel angles and concrete, (3) buckling resistance for the steel angles, and (4) lateral confinement for the core concrete. To satisfy the requirements of (3) and (4), close spacing as well as sufficient strength are required for the transverse reinforcement. However, the transverse bars welded to steel angles or the transverse plates bolt-connected to steel angles may cause premature tensile fracture of the connection, which should be considered in design.

Cover concrete provides local buckling resistance and fire resistance for the steel angles. However, when the transverse bars are not closely spaced, the PSRC composite columns are vulnerable to premature spalling of the cover concrete due to smooth surface of steel angles. Particularly, when the columns are subjected to high axial compression force, the load-carrying capacity and deformation capacity of the PSRC composite columns can be degraded by early spalling of the cover concrete. Further, under cyclic lateral loading, the PSRC composite columns are expected to be more susceptible to such damages as the ductility demand increases.

2.2. Compressive strength

2.2.1. Design method

The nominal compressive strengths P_n of a PSRC composite column under concentric axial loading can be evaluated by current design code equations for a concrete-encased steel composite column. For example, AISC 360–10 [8] specifies the nominal compressive strength based on plastic stress and column length effect.

$$P_n = P_{no} \cdot 0.658^{(P_0/P_e)} \tag{1}$$

$$P_{no} = 0.85f'_c\left(A_g - A_s - A_{sr}\right) + F_yA_s + f_{yr}A_{sr} \tag{2}$$

$$P_e = \pi^2\left(EI_{eff}\right)/(KL)^2 \tag{3}$$

$$EI_{eff} = E_sI_s + 0.5E_sI_{sr} + C_1E_cI_c \tag{4}$$

$$C_1 = 0.1 + 2A_s/(A_c + A_s) \le 0.3 \tag{5}$$

where P_{no} = maximum compressive strength of the composite column; P_e = elastic buckling strength of the column; f_c' = concrete strength; F_y and A_s = yield strength and area of the steel section, respectively; f_{yr} and A_{sr} = yield strength and area of the longitudinal bars, respectively; EI_{eff} = effective flexural stiffness of the composite column; KL = effective buckling length; E_s = elastic modulus of steel; E_c = elastic modulus of concrete (= $4700\sqrt{f_c'}$); I_s, I_{sr}, and I_c = second-order moments of inertia of the steel section, reinforcing bar, and concrete, respectively, with respect to the centroid of the column section; and A_c = concrete area.

For better evaluation of the load-carrying capacity of a PSRC composite column, numerical analysis using the stress–strain relationship of confined concrete, unconfined concrete, and steel can be used as shown in **Figure 4** [1, 3]. The numerical analysis can be performed using strain compatibility method [9]. The stress–strain relationship of confined and unconfined concrete can be determined from various existing models [10–12].

The nominal compressive strengths P_n of a PSRC composite column under eccentric axial loading can be evaluated by assuming plastic stress distribution of the composite section. In

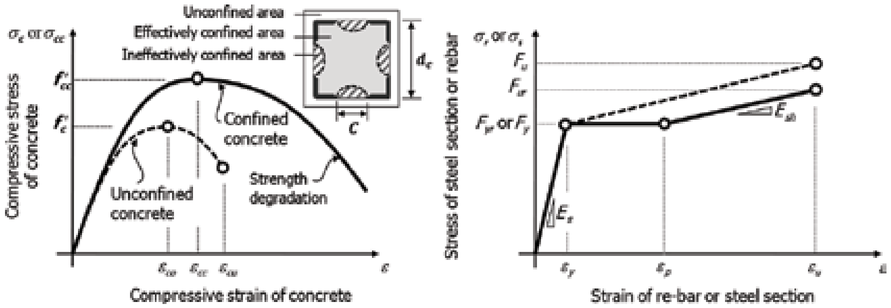

Figure 4. Stress–strain relationships of concrete and steel for numerical analysis.

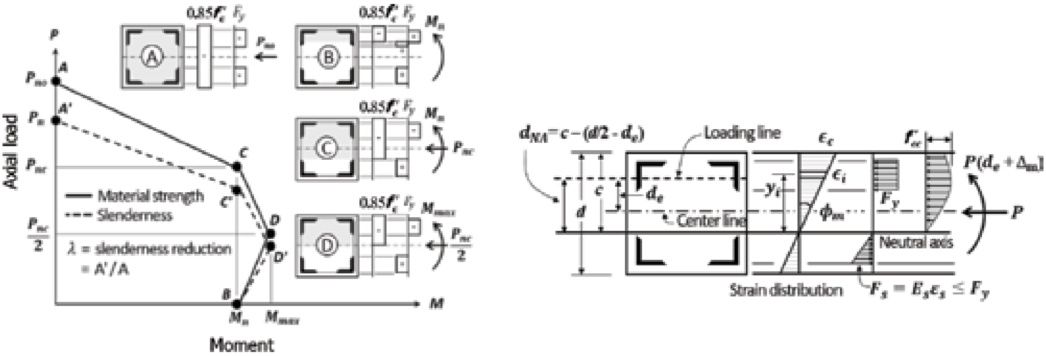

(a)

(b)

Figure 5. Section analysis methods of PSRC column under eccentric axial loading: (a) *P-M* interaction diagram and (b) strain-compatibility method.

Figure 5(a), performance points A and B indicate pure compressive strength P_{no} and moment strength M_n, respectively. Performance points C indicates the compressive strength P_{nc} corresponding to the moment M_n. Performance points D indicates the maximum moment strength corresponding to $P_{nc}/2$. Considering the slenderness effect of columns, each performance point should be decreased by multiplying the slenderness reduction factor λ to the compressive strength (where λ = ratio of P_n to P_{no}). Further, using the strain-compatibility method, *P-M* interaction diagram can be estimated (**Figure 5(b)**).

2.2.2. Structural test

Figure 6 shows the test setup for the concentric axial loading and eccentric axial loading tests. The eccentricity can be controlled using the distance between the column center and loading center. During the test, the load-carrying capacity, axial shortening, and horizontal expansion were measured to evaluate the structural performance of the PSRC composite columns.

Figure 7(a) compares the axial load-strain relationships of a CES and PSRC composite columns using steel ratio of 2.0% under concentric axial compression force [3–5]. The axial load behavior of the PSRC composite column was similar to that of the CES composite column. The

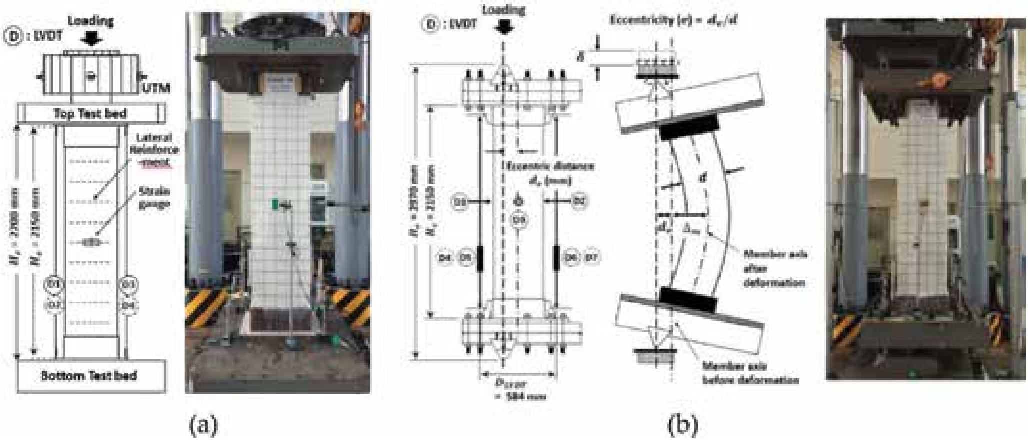

Figure 6. Test setup of compressive loading tests: (a) concentric axial loading and (b) eccentric axial loading.

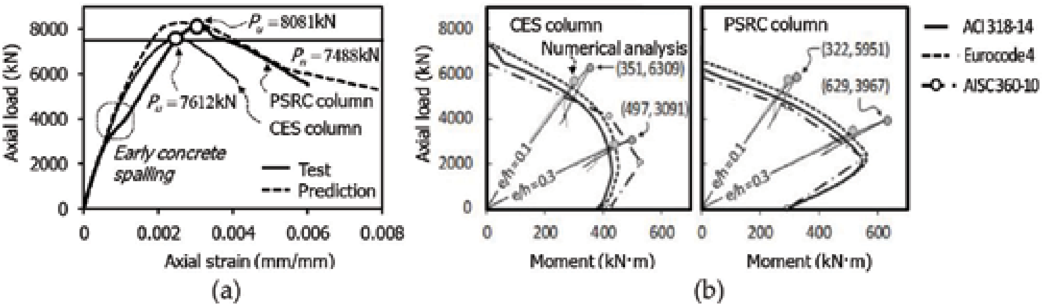

Figure 7. Axial load-carrying capacities of CES and PSRC columns: (a) concentric axial loading and (b) eccentric axial loading.

contribution of the steel angles to the lateral confinement increased the peak strength P_u and the deformation capacity in the PSRC composite column. Under concentric axial force, local buckling of the steel angles was not observed. After the peak strengths, significant cracking and subsequent concrete spalling occurred. Particularly, the early spalling can be initiated at the corners of the cross section because of the smooth surface of the angle. Thus, to secure robust axial load behavior of the PSRC composite columns under high axial load, it is recommended that the spacing of transverse reinforcement be decreased to half of the requirement of CES composite columns.

Figure 7(b) compares the *P-M* interaction curves of design codes [8, 13, 14] with the test results of CES and PSRC composite columns under eccentric load with a low eccentricity ratio of e/h = 0.1 and 0.3. As the eccentricity ratio increased, the structural behavior changed from compression to flexure. The peak strength of the CES composite column was less than that of the PSRC composite column with e/h = 0.3. This is because the effective compressive area of the steel and concrete sections was increased in the PSRC composite column with large eccentricity. In the PSRC composite columns, the *P-M* interaction curves of design codes were similarly predicted at the load level of $0.2P_n$ to $0.5P_n$, regardless of the assumption for the stress distribution. Further, the maximum flexural strength predictions of the PSRC composite columns were greater than those of the CES composite columns, because of the steel angles placed at the four corners of the column. This result indicates that when the same amount of the steel is used for composite columns, the flexural strength of PSRC composite columns can be greater than that of CES composite columns under general design compression load (= $0.2P_n$ ~ $0.5P_n$).

2.3. Flexural strength

2.3.1. Flexural design method

The ultimate flexural strength of a PSRC composite column can be evaluated by performing a section analysis based on either plastic stresses (i.e., plastic stress method) or strain-induced stresses (i.e., strain-compatibility method); the stresses of the steel angles, reinforcing bars, and concrete are determined by linear strain distribution and the stress–strain relationships of the materials [1]. **Figure 8** shows the stress distributions at the PSRC cross section by two methods. For the plastic stress method (**Figure 8(a)**), plastic stresses of concrete, steel angles, and reinforcing bars can be used as $0.85f_c'$, F_y, and F_{yr}, respectively. For the strain-compatibility method (**Figure 8(b)**), strain-induced stresses of angles, reinforcing bars, and concrete can be determined assuming linear distribution of strain over the entire cross section.

$$-F_y \le \sigma_s = E_s\varepsilon \le F_y \tag{6}$$

$$-F_{yr} \le \sigma_r = E_s\varepsilon \le F_{yr} \tag{7}$$

$$\sigma_c = f_c'\left(\frac{2\varepsilon}{\varepsilon_{co}} + \left(\frac{\varepsilon}{\varepsilon_{co}}\right)^2\right) \quad for - \varepsilon_{cu} \le \varepsilon \le 0 \tag{8}$$

where σ_s, σ_r, σ_c = strain-induced stresses of angles, re-bars, and concrete, respectively; ε = strain which is linearly proportional to the distance from the neutral axis; ε_{co} = strain corresponding to the concrete strength f_c'; and ε_{cu} = ultimate strain of concrete. In σ_s, σ_r, σ_c, and ε, compressive stress and strain are negative values. Perfect bond (or full composite action) between steel

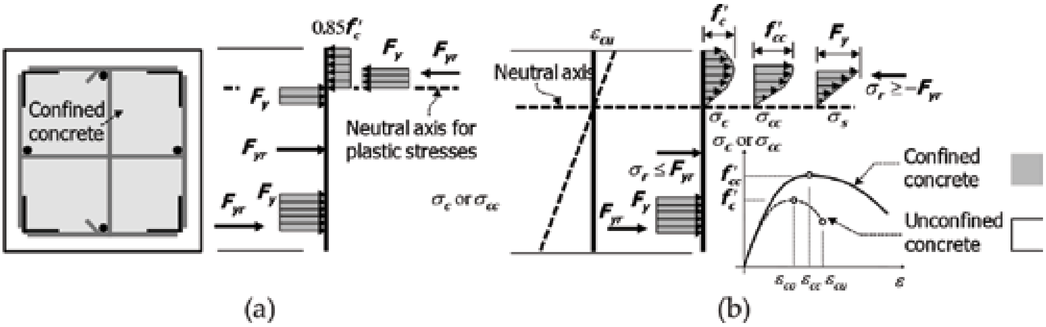

Figure 8. Section analysis methods of PSRC column: (a) plastic stress method and (b) strain-compatibility method.

angles and concrete is assumed for the section analysis. For confined concrete, the stress–strain relationship of the confined concrete can be used.

2.3.2. Shear design method

The shear resistance of a PSRC composite column is provided by concrete, transverse reinforcement, and steel angles. Since the dimensions of the angle cross section are significantly less than that of the entire cross section, the contribution of the angles to the shear strength is neglected. Thus, the nominal shear strength V_n of a PSRC composite column can be calculated, on the basis of current RC design code [13].

$$V_n = \frac{1}{6}\sqrt{f'_c}bd + A_{st}F_{yt}\frac{d}{s} \le \frac{5}{6}\sqrt{f'_c}bd \tag{9}$$

where b = width of the cross section; d = effective depth of the cross section; and A_{st}, F_{yt}, and s = area, yield stress, and spacing of the transverse reinforcement, respectively.

2.3.3. Bond strength design method

Figure 9 shows the details of the weld- or bolt-connection between the steel angles and transverse reinforcement. Before spalling of concrete cover, the shear transfer between the steel angles and concrete is provided by friction of the angle surface and concrete bearing of the transverse reinforcement projected from the angle surface. Conservatively neglecting the frictional resistance, the nominal bond strength B_n of a steel angle is provided by the concrete bearing of the transverse reinforcement [1].

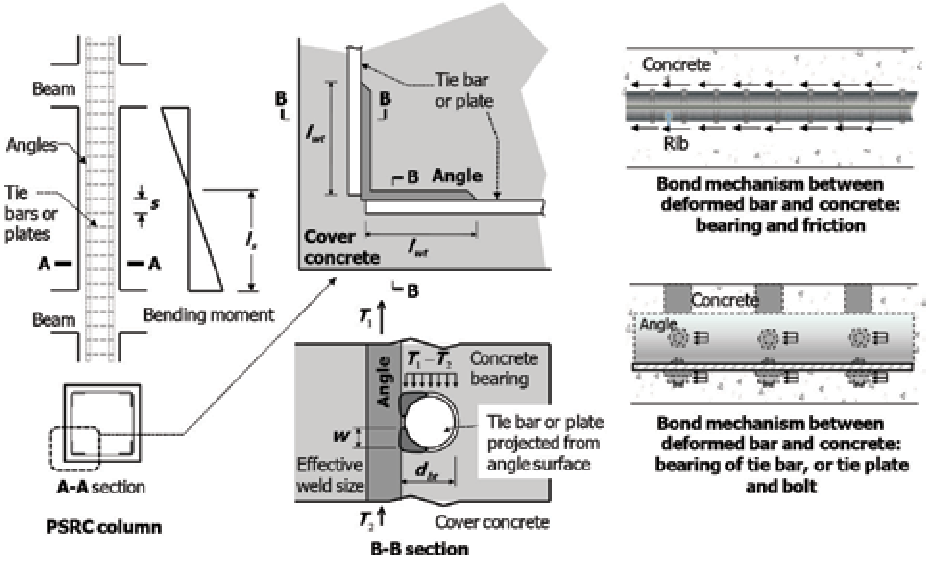

Figure 9. Bond strength between steel angle and concrete.

$$B_n = \alpha\left[0.85 f'_c (2 d_{bt} l_{wt})\right]\left(\frac{l_s}{s}\right) \tag{10}$$

where d_{bt} = diameter or thickness of a transverse reinforcement projected from the angle surface; l_{wt} = weld length of a transverse bar or projected length of a transverse plate from the angle surface; l_s = shear span length of the PSRC composite column; and α = a factor addressing the confinement effect on the bearing area (≤2.0). After spalling of concrete cover at large inelastic flexural deformation, concrete bearing disappears and is replaced by dowel action of the transverse reinforcement.

2.3.4. Structural test

Figure 10 shows the test setup for the flexural loading tests to investigate the flexural and shear strengths, shear transfer between steel angle and concrete, and strength at the joint between steel angle and transverse reinforcement. The columns are simply supported, and two-point loading is applied at the center of the columns. To estimate the curvature, deflections at least three points need to be measured.

Figure 11(a) shows the moment-curvature relationships at the center span of a CES column and a PSRC column with a cross section of 500 mm × 500 mm (i.e., 2.0% steel ratio) [1]. In the PSRC column using the same steel ratio of the CES column, the peak strength was 56.7% greater than that of the CES column for the following reasons: (1) the yield strength of the steel angles used for the PSRC column was 15.9% greater than that of the wide-flange steel section used for the CES column and (2) the angles placed at the four corners of the cross section can develop 35.2% higher nominal flexural capacity than the center wide-flange steel section. In the PSRC column, the load-carrying capacity was suddenly decreased when bond failure (i.e., concrete bearing failure) occurred in the bottom angles in the shear span (**Figure 12(b)**). After the bond failure, dowel action of the transverse bars developed, causing significant bond-slip deformation. Ultimately, it failed due to the fracture of the transverse bars and spalling of web concrete, which was the typical bond-shear failure mode of the PSRC composite column.

Figure 11(b) compares the effect of transverse reinforcement spacing on the moment-curvature relationship of PSRC composite columns with a smaller cross section of 400 mm × 400 mm

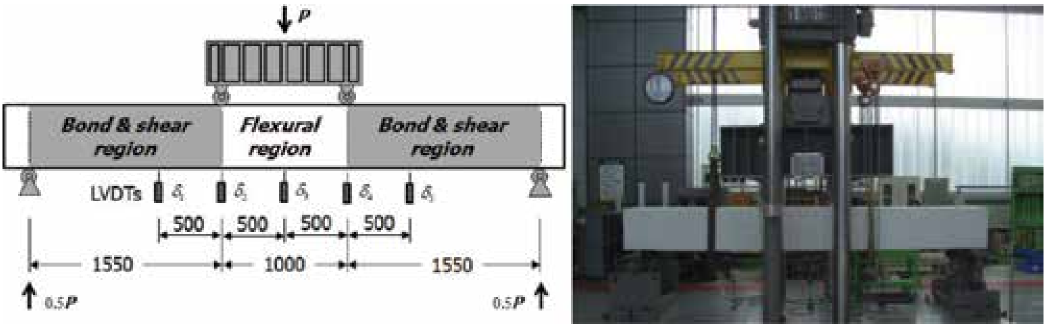

Figure 10. Test setup of flexural loading tests.

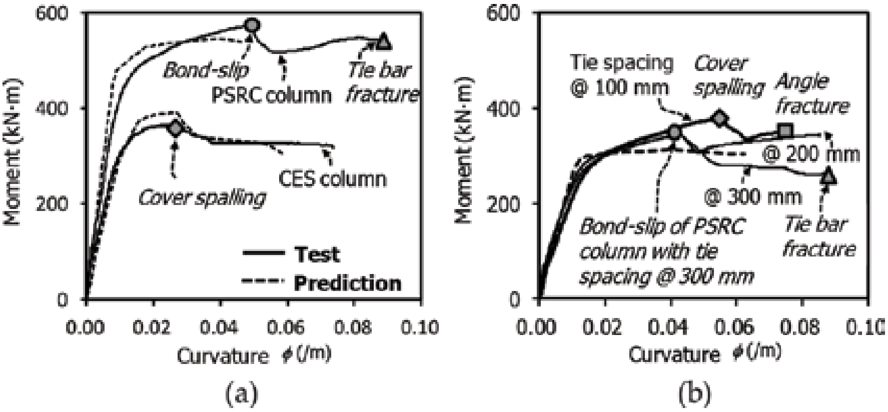

Figure 11. Moment-curvature relationships at the center span of CES and PSRC columns: (a) CES and PSRC columns; (b) PSRC columns according to transverse bar spacing.

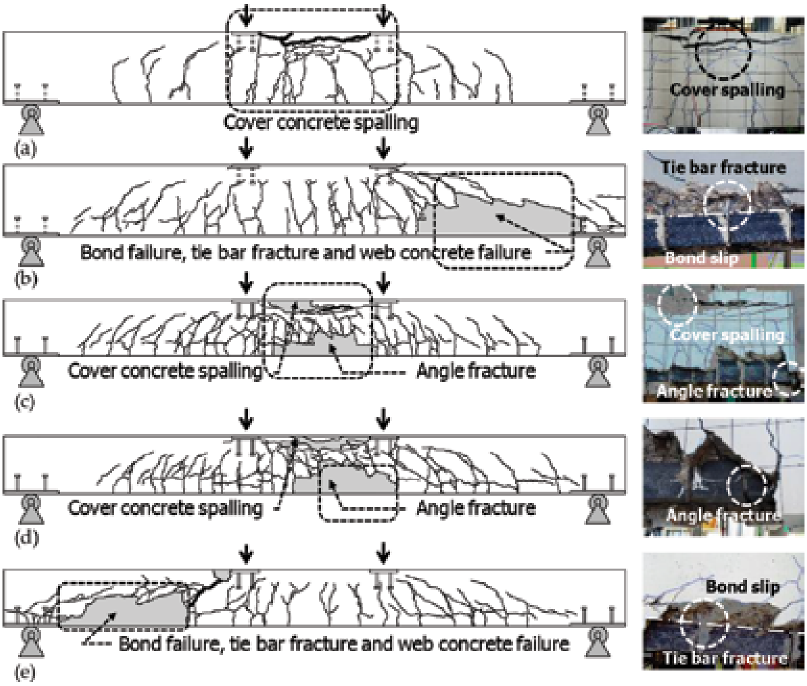

Figure 12. Failure modes of CES and PSRC columns. (a) CES column, (b) PSRC column, (c) PSRC column @ 100 mm tie, (d) PSRC column @ 200 mm tie, (e) PSRC column @ 300 mm tie

(i.e., 3.1% steel ratio). When the transverse reinforcement at a spacing of 100 mm was used, the load-carrying capacity was degraded due to spalling of cover concrete in the uniform moment span, but was slightly recovered due to the strain hardening of the steel angles. Ultimately, it failed due to the tensile fracture of the bottom angle in the uniform moment span (**Figure 12(c)**).

The moment-curvature relationship and failure mode of the PSRC composite column with greater transverse reinforcement spacing of 200 mm were similar to those of the PSRC composite column with transverse reinforcement spacing of 100 mm. It failed due to tensile fracture of the angles in the uniform moment span (**Figure 12(d)**). In the PSRC composite column with the greatest transverse reinforcement spacing of 300 mm, bond failure occurred in the bottom angles. After the bond failure, the load-carrying capacity was significantly decreased due to spalling of web concrete caused by dowel action of the transverse reinforcement. Ultimately, it failed due to fracture of the transverse reinforcement (**Figure 12(e)**).

2.4. Seismic performance

Figure 13 shows the test setup of cyclic loading tests for CES and PSRC composite columns. Using two oil jacks, a uniform axial load corresponding to about 22% of compressive capacity are applied, and a cyclic lateral load is applied using an actuator to the column.

Figure 14 compares the cyclic behaviors of the CES and PSRC composite columns using steel ratio of 2.2%. In the CES composite column, the load-carrying capacity gradually decreased after the peak strength. Although spalling of the cover concrete occurred at the lateral drift of 3.0–4.0% in the plastic hinge region, the load-carrying capacity was not significantly decreased. However, after the spalling of the cover concrete, post-yield buckling occurred in the longitudinal bars. Ultimately, it failed at the drift ratio of 7.0% because of a low cycle fatigue fracture of the longitudinal bars. In the PSRC composite column, the peak strength was 20% greater than that of the CES composite column because of the higher yield strength and the location of the steel angles. Spalling of the cover concrete occurred at the drift ratio of 3.0%, and significant shear cracks occurred in the plastic hinge region because of the increased shear demand. The angles and transverse reinforcement were exposed because of the spalling of cover concrete at the drift ratio of 5.0%. The exposed angles and longitudinal bars were subjected to local

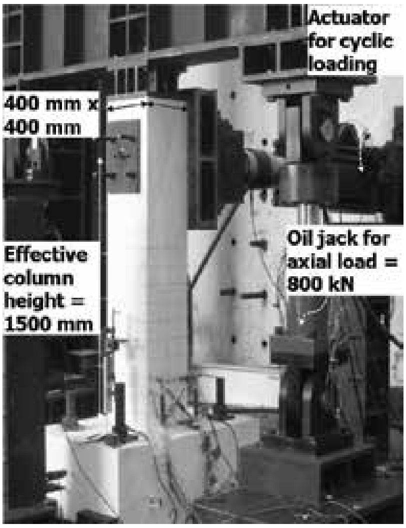

Figure 13. Test setup of cyclic loading tests.

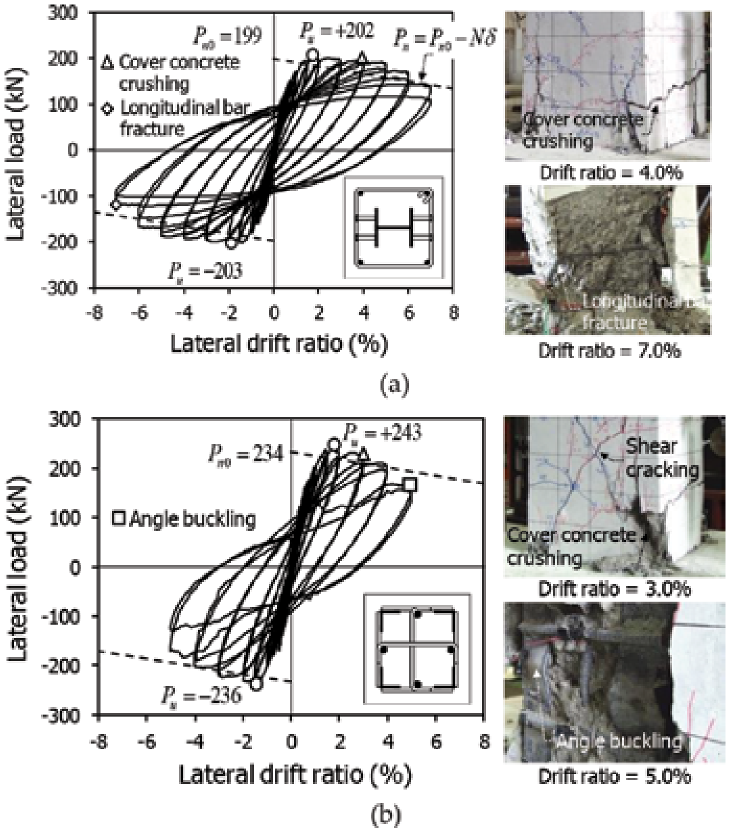

Figure 14. Lateral load-drift relationships of CES and PSRC columns: (a) CES column and (b) PSRC column.

buckling during repeated cyclic loading. As a result, the load-carrying capacity was degraded. However, despite the local buckling of angles and longitudinal bars, tensile fracture did not occur at the joint between the angles and transverse reinforcement.

2.5. Beam-column joint

2.5.1. Design method

Figure 15 shows a U-shaped composite beam-PSRC composite column connection. In order to minimize the workability problem during concrete pouring, only the web plate of the U-section is passed through the joint, and the top and bottom flanges are connected to the top and bottom band plates in the joint. Under high axial compressive force and cyclic lateral loading, premature cover concrete spalling of the joint may deteriorate the connection's strength and deformation capacity.

Figure 16 shows the three mechanisms that contribute to the joint shear strength: web shear yielding of the U-shaped steel section (**Figure 16(a)**), direct strut action of the in-filled concrete

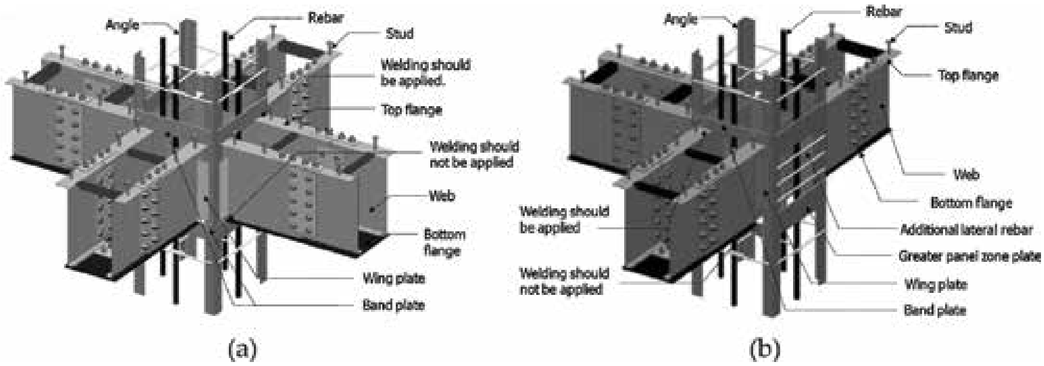

Figure 15. Beam-column joint details: (a) interior beam-column joint and (b) exterior beam-column joint.

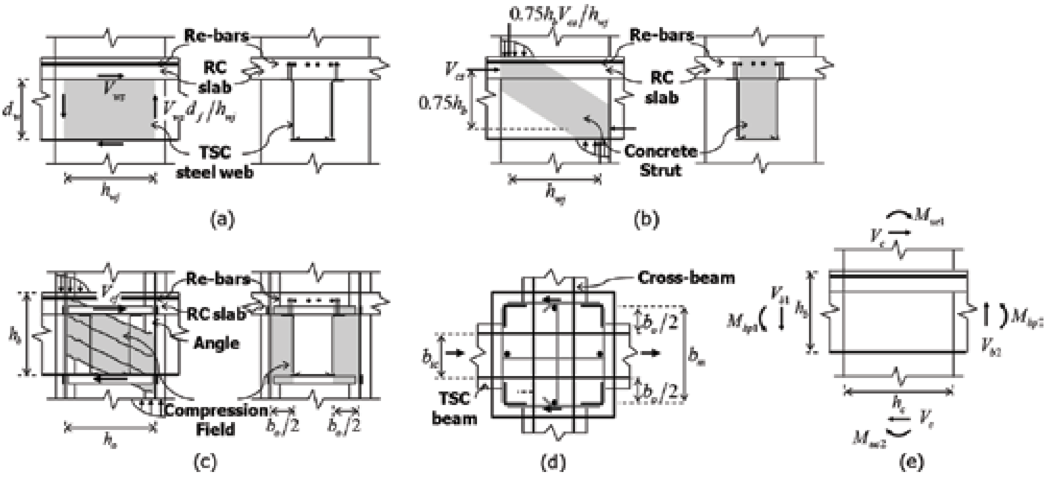

Figure 16. Joint shear strength mechanisms. (a) Web shear yielding (V_{ws}), (b) Concrete diagonal strut (V_{cs}), (c) Strut and tie action (V_{st}), (d) Effective width b_o for interior joint, (e) Joint shear demand.

inside the U-shaped section (**Figure 16(b)**), and the strut-and-tie action between the concrete (outside of the U-shaped section) and the band plates (**Figure 16(c)**) [2]. The shear strength V_{ws} of the two web plates is defined as follows:

$$V_{ws} = (2) \cdot 0.6 F_y t_w h_{wj} \tag{11}$$

where t_w = web thickness; and h_{wj} = effective horizontal length of the web in the joint in the direction of the shear.

The shear strength V_{cs} of the direct concrete strut is defined as follows:

$$V_{cs} = 1.7\sqrt{f'_c}\, b_{ic} h_c \le 0.5 f'_c b_{ic} h_b \quad \text{for the interior joint} \tag{12}$$

$$V_{cs} = 1.2\sqrt{f'_c}\, b_{ic} h_c \le 0.5 f'_c b_{ic} h_b \quad \text{for the exterior joint} \tag{13}$$

where b_{ic} = width of the in-filled concrete, h_c = depth of the PSRC composite column; and h_b = overall depth of the composite beam including the concrete slab.

The shear strength V_{st} of the strut-and-tie action is defined as follows:

$$V_{st} = 0.4\sqrt{f'_c}\,b_o h_o \tag{14}$$

$$b_o = b_{af} - b_{ic} - 2t_w \tag{15}$$

where b_o = effective width of the joint concrete; h_o = effective length of the joint concrete in the direction of shear; b_{af} = distance between the corner angles in the direction orthogonal to the shear; and b_{ic} and t_w = width of the in-filled concrete and web of the U-shaped section, respectively.

For the strut-and-tie mechanism in Eq. (14), the tension force caused by the concrete strut should be resisted by the top and bottom band plates. Thus, the required cross-sectional area A_{bp} of each band plate is calculated as follows:

$$A_{bp} \geq \frac{V_{st}}{2F_{ybp}} \tag{16}$$

where $2F_{ybp}$ = yield strength of the top and bottom band plates.

The joint shear capacity and demand can be expressed as moments, from the static moment equilibrium at the joint (**Figure 16(e)**).

$$\sum M_{uc} - \sum V_b h_o/2 \leq \phi M_{nc} \tag{17}$$

$$\sum M_{uc} = \sum M_{bp} + \sum V_b h_c/2 - V_c h_b \tag{18}$$

$$M_{nc} = V_{ws} d_w + V_{cs}(0.75h_b) + V_{st} d_b \tag{19}$$

where (ΣM_{uc} - ΣV_b $h_o/2$) and M_{nc} = joint shear demand and capacity, respectively; ΣM_{pb} and ΣV_b = sums of the plastic moments and shear demands, respectively, of the composite beams framing into the joint; V_c = column shear demand; d_w = center-to-center distance between the top and bottom flanges; $0.75h_b$ = approximate moment arm for the composite beam section; and d_b = center-to-center distance between the top and bottom band plates.

2.5.2. Structural test

Figure 17 shows the cyclic lateral load-story drift ratio relationships of U-shaped steel composite beam-PSRC composite column joints. The composite beam has 330 mm width and 700 mm height including slab. The PSRC composite column has 800 mm × 800 mm cross-sectional area. In the interior beam-column joint, cover concrete spalling in the PSRC composite column occurred in the vicinity of the U-section, whose web plate buckled, and severe diagonal cracking occurred in the joint face. The fracture was initiated at the weld joint between the web and the bottom flange and then propagated vertically. Because the band

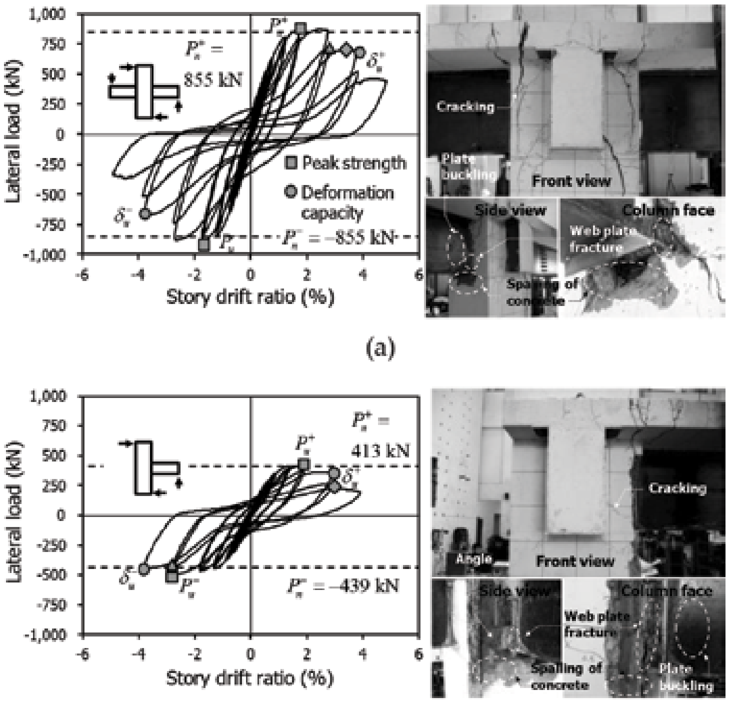

(a)

(b)

Figure 17. Lateral load-drift relationships: (a) interior beam-column joint and (b) exterior beam-column joint.

plates were not connected to the bottom flange of the U-section, the band plates were not damaged even after cover concrete spalling. However, a gap occurred between the end of the U-section and the column face under positive moments, which was attributed to an anchorage slip of the web plates showing plastic strains inside the joint. As the anchorage slip increased, development of the beam's flexural capacities was delayed, which caused significant pinching in the cyclic behavior. The top band plates welded to the top flange of the U-section were pulled out under a negative moment. In the exterior beam-column joint, after the peak strengths, the load-carrying capacity was significantly degraded because of cover concrete spalling in the PSRC composite column and because of local buckling and fracture of the web in the composite beam. The steel angles of the column were completely exposed.

3. Conclusions

In this chapter, a prefabricated steel-reinforced concrete (PSRC) composite column using steel angles was introduced. Using current design codes, the structural capacities of PSRC composite columns can be evaluated, and it shows better performance than those of a conventional concrete-encased steel (CES) composite column.

- The axial load-carrying capacity and deformation capacity of PSRC composite columns are comparable to, or even better than, those of conventional CES composite columns. In the PSRC composite column under axial compression, the corner angles and the transverse reinforcement provide adequate lateral confinement to the concrete.
- The corner angles of the PSRC composite column increase the flexural strength and stiffness up to about 30%, compared to those of the conventional CES composite columns.
- The bond strength between steel angles and concrete is generated by the bearing strength of the transverse reinforcement projected from the steel angle surface. When the bond strength is greater than the demand (i.e., when close spacing of tie bars is used), the PSRC composite columns show ductile behavior after flexural yielding without bond failure, and ultimately fail due to fracture of the steel angles. Otherwise, significant bond slip occurs in the steel angles, and ultimately the columns fail due to the bond failure of steel angles or the fracture of transverse bars.
- Under cyclic lateral loading, the PSRC composite columns show about 20% lower deformation capacities than that of the conventional CES composite column. The lower deformation capacity of the PSRC composite columns is attributed to the following reasons: (1) relatively large plastic strains occur in the corner steel angles; (2) after spalling of the cover concrete, the exposed steel angles are susceptible to local buckling; and (3) the shear demand of the transverse reinforcement increases.
- In composite beam-PSRC composite column joints, the load-carrying capacity decreases because of the web local buckling of the U-section at the column face. Ultimately, the beam-column joints fail because of a tensile fracture of the buckled web plates initiated at the weld joint between the web and the bottom flange of the U-section. As yielding occurs in the web plate of the beam, significant web plate anchorage slip occurs inside the joint. However, the anchorage slip mitigates possible stress concentration that may be caused by the discontinuity of the flange plate, which contributes to the increase in deformation capacity.

Author details

Hyeon-Jong Hwang

Address all correspondence to: hwanggun85@naver.com

College of Civil Engineering, Hunan University, Changsha, Hunan, China

References

[1] Eom TS, Hwang HJ, Park HG, Lee CN, Kim HS. Flexural test for steel-concrete composite members using prefabricated steel angles. Journal of Structural Engineering. 2014;**140**(4): 04013094. DOI: 10.1061/(ASCE)ST.1943-541X.0000898

[2] Hwang HJ, Eom TS, Park HG, Lee SH, Kim HS. Cyclic loading test for beam-column connections of concrete-filled U-shaped steel beams and concrete-encased steel angle columns. Journal of Structural Engineering. 2015;**141**(11):04015020. DOI: 10.1061/(ASCE) ST.1943-541X.0001242

[3] Hwang HJ, Eom TS, Park HG, Lee SH. Axial load and cyclic lateral load tests for composite columns with steel angles. Journal of Structural Engineering. 2016;**142**(5):04016001. DOI: 10.1061/(ASCE)ST.1943-541X.0001452

[4] Kim HJ, Hwang HJ, Park HG, Kim DK, Yang JM. Eccentric axial load test of prefabricated composite columns using bolt-connected steel angles. Journal of Korean Society of Steel Construction. 2017;**29**(3):249-260. DOI: 10.7781/kjoss.2017.29.3.249

[5] Kim HJ, Hwang HJ, Park HG, Kim DK, Yang JM. Axial load test of prefabricated composite columns using bolt-connected steel angles. Journal of Korean Society of Steel Construction. 2017;**29**(2):147-158. DOI: 10.7781/kjoss.2017.29.2.147

[6] AWS (American Welding Society). Structural Welding Code-Reinforcing Steel (AWS D1.4). Miami; 1998. 45 p

[7] AWS (American Welding Society). Structural Welding Code-Steel (AWS D1.1). Miami; 2010. 540 p

[8] AISC (American Institute of Steel Construction). Specification for Structural Steel Building (ANSI/AISC 360-10). Chicago; 2010. 610 p

[9] Spacone E, El-Tawil S. Nonlinear analysis of steel-concrete composite structures: State of the art. Journal of Structural Engineering. 2004;**130**(2):159-168. DOI: 10.1061/(ASCE)0733-9445(2004)130:2(159)

[10] Hognestad E. A study of combined bending and axial load in reinforced concrete members. In: Bulletin Series. Vol. 399. Urbana, IL: Univ. of Illinois Engineering Experimental Station; 1951

[11] Mander JB, Priestley MJN, Park R. Theoretical stress strain model for confined concrete. Journal of Structural Engineering. 1988;**114**(8):1804-1826. DOI: 10.1061/(ASCE)0733-9445 (1988)114:8(1804)

[12] Hoshikuma J, Kawashima K, Nagaya K, Taylor AW. Stress-strain model for confined reinforced concrete in bridge piers. Journal of Structural Engineering. 1997;**123**(5):624-633. DOI: 10.1061/(ASCE)0733-9445(1997)123:5(624)

[13] ACI (American Concrete Institute). Building Code Requirements for Structural Concrete and Commentary. ACI 318-14. Farmington Hills, MI; 2014. 520 p

[14] Eurocode 4. Design of Composite Steel and Concrete Structures-Part 1-1: General Rules and Rules for Buildings. Belgium: CEN; 2004. 122 p

Section 3

Theoretical Modeling

Chapter 4

Mechanical Performance of Simple Supported Concrete Beam-Cable Composite Element with External Prestress

Teng Wang, Yanmei Ding, Wangchun Zhang and
Yu Song

Additional information is available at the end of the chapter

http://dx.doi.org/10.5772/intechopen.76517

Abstract

A new reinforcement technology of external prestress based on stretch tilted belly poles has been presented. Taking simply supported beam, which is reinforced by three titled belly poles, as a research object to establish a model of reinforced simply supported beam. Relationship expressions about deflection and internal force increment of external cable or about load and deflection have been deduced. Finite element model is established by ABAQUS. The influence of structure performance of reinforced simply supported beam with cable section, cable sag and initial internal force value was investigated. Three tests are carried out to testify the results of theoretical analysis and numerical simulation. The results show that the redistributions of internal force and sectional stress have occurred, and the stiffness, crack load, ultimate load, and structure ductility are all improved with the increase of three design parameters. For example, the crack load, ultimate load, and structure ductility have increased, respectively, by 24%~40%, 15%~42%, and 14%~40%. High initial internal force, small section, and big cable sag should be avoided, because the probability of brittle failure of structure will increase. The analytical result shows that the reliability of internal increment expression of external cable and carrying capacity expression can be used in the engineering practice.

Keywords: concrete structure, simply supported beam, external prestress, tilted belly poles, test

1. Introduction

External prestressing is a technique originally developed for reinforcing bridge structures and now has applications in architectural structures [1]. It has gone through three stages of development. In the early stage, external tendons were installed with curvature at the bottom and sides of a beam and held by deviators. Prestressing forces were applied by transverse tensioning. In the second stage, external tendons were installed with curvature only at the vertical sides of a beam, and prestressing forces were applied by a tensioning jack. Multiple weaknesses have been identified in this tensioning technique during practical applications. First, prestressing forces had to be applied to an independent working surface, but the working surface was usually obstructed by columns. Second, the friction between a deviator and an external tendon could weaken the effects of prestressing forces. To avoid the aforementioned problem with working surface, external tendons were usually continuously and axially installed along the full length of a beam. However, this would complicate the stress states of the columns and beam-column joints and thereby undermine the structure's seismic performance [2]. To overcome these disadvantages, retractable web members were introduced to apply prestressing forces in the later stage. Web members can be installed vertically or diagonally, and DWMs are an improvement on vertical web members (patent number: ZL 03134360.0). In DWM prestressing, external tendons are anchored to the upper parts of both beam sides, and retractable DWMs are used to stretch the tendons, which then transfer the prestressing forces to the beam. Compared to the two earlier external prestressing techniques, DWM prestressing has two main advantages: (1) The way in which the prestressing force is applied allows for easier and safer construction and enhances the effects of prestressing forces; (2) As external tendons are not continuously installed along the full beam length and do not span any column, the installation process will neither cause mechanical disturbance to the floor, columns, and other vertical elements nor occupy the space required to reinforce vertical elements; (3) external tendons running through beam ends can increase the shear strength of beam ends [3, 4].

At present, stress increments in external tendons can be calculated mainly by the reduction factor method, regression analysis of section reinforcement ratio, deformation analysis, and so on. However, there is a lack of unified standard and the standard parameter values for an external tendon in the stiffness of a beam is infinitely great an ultimate state differ between standards from different countries [5–8]. Based on the assumption of infinite beam stiffness, a study [9] examined the force distribution in an external tendon that was subjected to a uniformly distributed load applied by DWM, with the increase in tendon length being used as the parameter. The relationship between tendon extension and load was derived. When DWM external prestressing is applied to a simply supported beam (SSB), the beam does not have infinite stiffness and tends to deform under the prestressing force [10, 11]. The load on tendons applied by web members was not uniformly distributed. Therefore, the mechanical behavior of a beam reinforced by this technique remains unknown. For this reason, the present study investigated the behavior of a SSB reinforced by external prestressing with three DWMs using a combination of theoretical derivation, numerical analysis, and experimental verification. Three variables, including initial tendon force, tendon cross-sectional area, and initial tendon sag, were considered and the influences of beam-end rotation and beam deflection on tendon force were analyzed. Then the pattern of variation in the RC beam's structural performance was obtained. The findings of the study are expected to provide a design basis for practical application of this technique and theoretical support for research on the mechanical behavior of a fixed-end beam after reinforcement.

2. Theoretical analysis

2.1. Increment in tendon stress

2.1.1. Fundamental assumptions

The theoretical analysis was based on the following fundamental assumptions:

1. An external tendon is an ideally flexible material subjected only to tension, and it deforms only elastically throughout its deformation process;
2. The web members have infinite stiffness and do not stretch or shrink during beam deformation. They are always perpendicular to the tangents at the connections between web members and tendons. The effect of dead load of web members on tendons is ignored;
3. The slip between external tendons and web members during beam deformation is negligible and so is the friction between tendons and beam-end anchorage and between web members and beam-bottom anchorage. The shear deformation of the beam, together with its secondary effect, has only negligibly small effects on RC beam.
4. The load applied to an external tendon by the three DWMs can be treated as a uniformly distributed load.

2.1.2. Computing model of tendon

Figure 1 shows the curves describing deformation of an external tendon in a SSB reinforced by DWM prestressing. The dotted line L_1 shown in the figure is the elliptic curve describing the deformation of a tendon under a uniformly distributed load provided in [9]. The solid line, L_2, is a broken line for a tendon stabilized by three web members; it is a polygon incised in L_1.

2.1.3. Solving for external tendon force

According to Song Yu [9], the shape function for a tendon under a uniformly distributed load has the following form:

$$\frac{\left(y-\frac{l^2-8f^2}{16f}\right)^2}{\left(\frac{l^2+8f^2}{16f}\right)^2}+\frac{\left(x-\frac{l}{2}\right)^2}{2\left(\frac{l^2+8f^2}{16f}\right)^2}=1 \tag{1}$$

where l and f are the tendon span and sag, respectively, after application of the initial prestressing force.

Let $m = \frac{l^2+8f^2}{16f}$ and compute the derivative of the shape function with respect to x. Then performing integration on the arc-length formula will yield the expression for initial tendon length, s_o:

$$s_0 = \frac{3l}{4} + \frac{\sqrt{2}\,m}{4} + \ln\frac{2\sqrt{2}\,m+l}{2\sqrt{2}\,m-l} \tag{2}$$

When the SSB undergoes a beam-end rotation of θ under the action of an external load, the resulting span and sag of each tendon can be expressed as follows:

$$L' = l - 2 \cdot e \cdot \sin\theta \tag{3}$$

$$f = f + y \tag{4}$$

where e is the initial eccentricity of external tendon and y is the deflection of the beam under the action of an external load.

Change in tendon length is associated with tendon span and sag. After the SSB deforms, both the tendon span and sag will change. Substituting Eqs. (3) and (4) into Eq. (2) will give the tendon length for a given beam deflection.

$$s = \frac{3L'}{4} + \frac{\sqrt{2}\,m'}{4} + \ln\frac{2\sqrt{2}\,m'+L'}{2\sqrt{2}\,m'-L'} \tag{5}$$

where $m' = \frac{L'^2+8f'^2}{16f'}$.

Since the behavior of external tendons is always elastic, according to the Hooke's law,

$$\Delta S = S - S_0 \tag{6}$$

$$\Delta S = \frac{\Delta F}{EA_s} \cdot S_0 \tag{7}$$

$$p_s = P_0 + \Delta F \tag{8}$$

where Δs is tendon extension, ΔF is the increment in tendon force, E is tendon's elastic modulus, A_s is tendon cross-sectional area, s_0 is initial tendon length, and p_S is the tendon force for a given beam deflection.

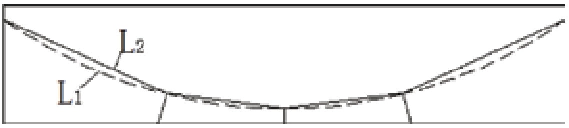

Figure 1. The external cable diagram of deformation.

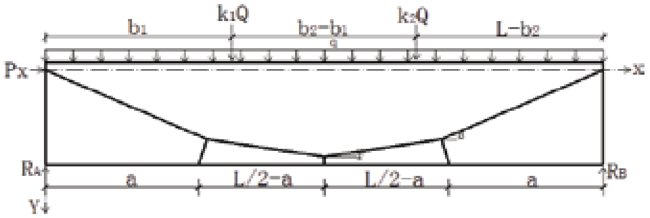

Figure 2. Analysis diagram of beam-cable element.

2.2. Calculation of bearing capacity of a RC beam during normal service

2.2.1. Computing model

After a SSB is reinforced by DWM external prestressing, the main forces acting on it include constant and live loads (e.g., concentrated force, *ki·Q*, and uniformly distributed load, *q*), prestressing force on the beam exerted by tendons, p_s, reaction forces from the supports, and concentrated forces exerted on the beam by web members. This analysis focused on two randomly selected concentrated forces. The force analysis and the coordinate system used are presented in **Figure 2**.

2.2.2. Load-deformation relationship

Let EI denote the flexural rigidity of a beam within its elastic range and *e* be the initial eccentricity of tendon. The force applied by a DWM can be decomposed into two components. This analysis did not consider the effect of the horizontal component on the beam's mechanical behavior in order to simplify the calculation. The analytical results proved reliable. Normally, the use of *n* web members will divide a beam into four segments. Thus three web members divide the beam into four segments. Computing the moment at an arbitrary cross-section of the beam gives

$$EI \cdot y'' = \frac{qx(l-x)}{2} + k_i Q \cdot \sum_{i=1}^{n} f(x) - p_s \cdot m(x) - p_s \cdot (e+y) \cdot \cos\gamma \tag{9}$$

where

$$f(x) = \begin{cases} x(l-b_i)/l & (0 \le x \le b_i) \\ b_i(l-x)/l & (b_i \le x \le l) \end{cases} \tag{10}$$

$$m(x) = \begin{cases} x\sin\gamma \quad (0 \le x \le a) \\ -(x-a)(\sin\gamma - \sin\beta) + x\sin\gamma \quad (a \le x \le a + l' \cdot \sin\varphi) \\ -(x-a)(\sin\gamma - \sin\beta) + x\sin\beta \quad (a + l' \cdot \sin\varphi \le x \le l/2) \\ -(l-x-a)(\sin\gamma - \sin\beta) + (l-x)\sin\beta \quad (l/2 \le x \le l - a - l' \cdot \sin\varphi) \\ -(l-x-a)(\sin\gamma - \sin\beta) + (l-x)\sin\gamma \quad (l - a - l' \cdot \sin\varphi \le x \le l - a) \\ (l-x)\sin\gamma \quad (l - a - l' \cdot \sin\varphi \le x \le l) \end{cases} \tag{11}$$

where *l′* is the length of a DWM, *Φ* is the angle between the DWM and the *y*-axis, *ki* is a load factor, *bi* is the distance from the concentrated load to the support, *r* is the angle between the midspan web member and the horizontal plane at its intersection with the tendon, and *β* is the angle between the DWM and the horizontal plane at its intersection with the tendon.

By taking the partial derivative of formula (9), we obtain

$$y(x)=e\left[\frac{\cos\omega(x-\frac{l}{2})}{\cos(\frac{\omega l}{2})}-1\right]+\frac{q}{p_s\cdot\cos\gamma}\cdot\Bigg\{\frac{x}{2}(l-x)-\frac{1}{\omega^2}\Bigg[\frac{\cos\omega(x-\frac{l}{2})}{\cos(\frac{\omega l}{2})}-1\Bigg]\Bigg]\Bigg\}$$
$$+\frac{Q}{p_s\cdot\cos\gamma}\sum_{i=1}^{2}k_i\cdot f(x)-\frac{1}{\cos\gamma}\cdot m(x) \tag{12}$$

where

$$\omega=\sqrt{\frac{p_s}{EI}\cos\gamma} \tag{13}$$

Eq. (12) describes the relationship between external load and RC beam deflection, which can be used as a theoretical basis for design of SSB reinforced by external prestressing with three web members.

3. Finite element analysis

3.1. Constitutive relations

A model of an RC beam reinforced by external prestressing was constructed by separate modeling using ABAQUS, a software suite for finite element analysis. The concrete was modeled using C3D8R, a linear reduced integration element with eight nodes. The rebars, web members, and external tendons were constructed of T3D2, a three-dimensional, two-node linear truss element. The slip between rebars and concrete was neglected. The constraints between the concrete and reinforcement cage were applied via the Embedded Region command. The constraint relationships between external tendon and concrete beam and between web members and concrete beam were achieved via the Kinematic coupling command. External prestressing force was applied by decreasing the temperature and solved by an implicit solver

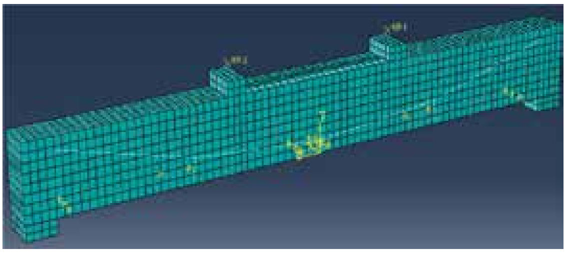

Figure 3. Finite element model. (a) Concrete, (b) steel reinforcement, (c) web member.

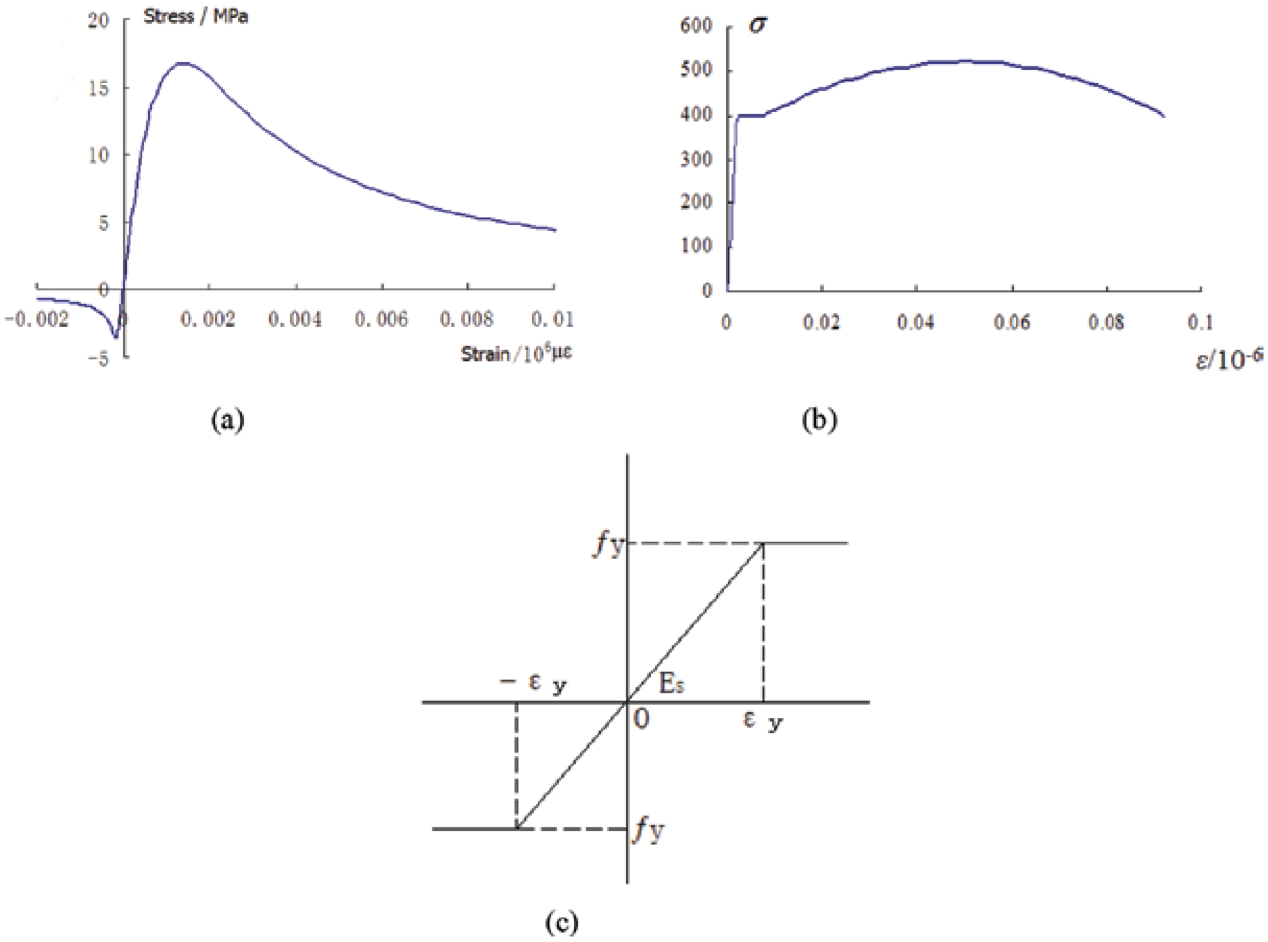

Figure 4. The material stress–strain curve.

(**Figure 3**). The concrete was modeled with the plastic damage constitutive model provided in ABAQUS, the rebars were modeled with the improved rebar model developed by Esmaeily-xiao, and the web members were simulated using an ideally elastic-plastic model. The constitutive relations for the model materials are presented in **Figure 4**.

3.2. Parameter design

The beam had dimensions of 3000 × 300 × 180 mm. It was constructed of C25 concrete, three Φ14 rebars in the concrete under tension, two vertical Φ14 rebars in the concrete under compression, Φ6 stirrups @100, and Φ14 web members (threaded). Design levels of the tendon parameters considered are as follows: initial tendon force, Level 3; tendon cross-sectional area, Level 3 (**Table 1**); and tendon sag, Level 4. Design values of other parameters are given in the first five lines of **Table 2**. FJGL denotes a control specimen, which was unreinforced. *denotes a specimen to be tested in the experimental verification.

3.3. Numerical results

3.3.1. Common features

The load-deflection curve for a RC beam generally splits into four portions. The characteristics of the four portions and the corresponding stages of the beam's behavior are summarized below:

1. Elastic deformation. In this stage, the concrete at the beam bottom slightly deflected without fracturing and the corresponding portion of the load-deflection curve is nearly linear;
2. Yielding. As the load increased, the bottom concrete showed increased deflection as a result of cracking. The rebars in the tensioned region reached the yield point earlier than the external tendons. The corresponding portion of the load-deflection curve contained a noticeable turning point;
3. Hardening. The neutral axis of a cross-section shifted downward and the external tendons were fully engaged in the work;
4. Failure. As the load continued increasing, the external prestressing tendon or the concrete under compression would fail after the tendon stress exceeded its ultimate strength or the compressive stress in the concrete exceeded its compressive strength. Their failure modes are different: the tendons failed via brittle fracture, while the concrete failed by ductile fracture.

No.	Cable diameter (mm)	Sectional area of cable (mm^2)	Breaking force (kN)
1	Φ9	48	75
2	Φ12	86	133
3	Φ15	134	208

Table 1. Design parameters of pre-stressed cables.

Beam number	**Cable sectional area (mm^2)**	**Sag of cable (mm)**	**Initial**		**Comparison of bearing capacity of simulated specimens**			
			Cable internal force (kN)	**Percent (%)**	**L/300 hour (kN)**	**Percentage increase (%)**	**L/200 hour (kN)**	**Percentage increase (%)**
FJGL	/	/	/	/	90	/	105	/
JGL-1-1*	48	200	20	27	97	8	116	10
JGL-1-2	48	200	30	40	110	22	121	15
JGL-1-3	48	200	40	53	116	29	128	22
JGL-1-4	48	200	60	80	125	39	143	36
JGL-2-1	86	200	20	15	108	20	120	14
JGL-2-2	86	200	40	30	121	34	135	29
JGL-2-3	86	200	60	45	130	44	150	43
JGL-3-1	134	200	20	10	110	22	122	16
JGL-3-2	134	200	40	20	126	40	138	31
JGL-3-3	134	200	60	29	134	48	153	46
JGL-4-1	48	250	20	27	100	11	120	14
JGL-4-2	48	250	40	53	118	31	138	31
JGL-4-3	48	250	60	80	136	51	152	45
JGL-5-1	134	250	20	10	114	27	124	18
JGL-5-2	134	250	30	15	125	39	130	24
JGL-5-3	134	250	40	20	135	50	142	35
JGL-5-4	134	250	60	29	146	62	157	50
JGL-6-1	48	300	20	27	108	20	127	21
JGL-6-2	48	300	40	53	125	39	150	43
JGL-6-3	48	300	60	80	143	59	166	58
JGL-7-1	134	300	20	10	120	33	144	37
JGL-7-2	134	300	40	20	148	65	165	58
JGL-7-3	134	300	60	29	164	82	190	81
JGL-8-1	48	400	20	27	113	26	135	29
JGL-8-2	48	400	40	53	130	44	165	57
JGL-8-3	48	400	60	80	155	72	185	76
JGL-9-1	134	400	20	10	153	70	200	90
JGL-9-2	134	400	40	20	190	111	230	119
JGL-9-3	134	400	60	29	237	163	260	147

*Indicates the test specimen to be tested.

Table 2. Simply supported beam's design parameters and change of bearing capacity.

3.3.2. Relationship between beam deflection and increment in tendon force

1. The greater the initial tendon force, the smaller the maximum tendon deflection (or a tendon's energy dissipation capacity). **Figure 5a** shows the tendon force-deflection curves of a tendon with a cross-sectional area of 48 mm^2 and sag of 200 mm for different initial tendon forces (20, 40, and 60 kN). It is clear that the maximum tendon deflection at the fracture point gradually decreased. This implies that it is unreasonable to optimize reinforcement design simply by increasing the initial tendon force.
2. As the tendon cross-sectional area increased, the rate of growth in tendon force increased, and thus the contribution by the tendon became more significant. Conversely, a smaller tendon cross-sectional area is associated with a slower rate of increase in tendon force. **Figure 5b** illustrates the tendon force-deflection curves for different tendon cross-sectional areas (48, 86, and 134 mm^2) when the tendon sag was 200 mm and initial tendon force was 20 kN. This figure demonstrates that a larger tendon cross-sectional area is better in reinforcement design.

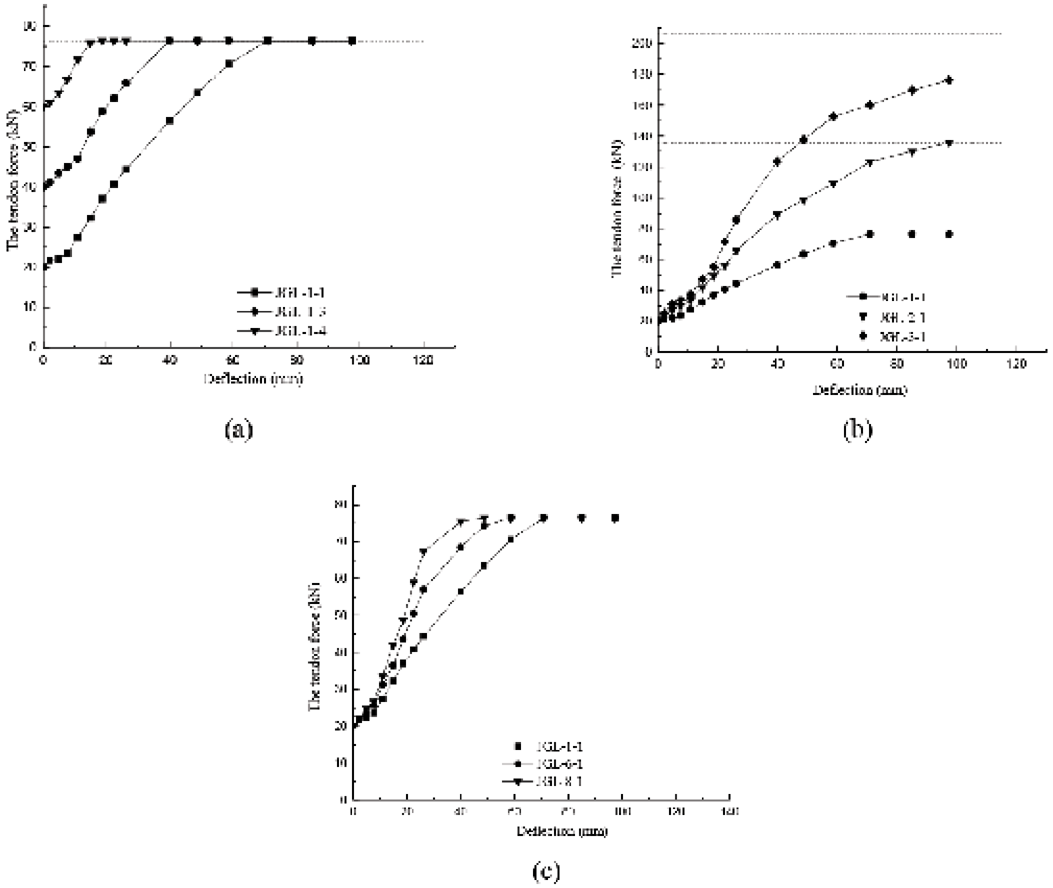

(a) (b) (c)

Figure 5. Cable internal force deflection curve. (a) The initial tendon force, (b) sectional area of cable, and (c) sag of cable. *The horizontal dotted line represents the tensile force at which the external prestressing tendon begins to fracture.

3. The rate of tendon force growth increased with increasing tendon sag. **Figure 5c** shows the tendon force deflection curves for different tendon sags (200, 300, and 400 mm) when the tendon cross-sectional area was 48 mm^2 and initial tendon force was 20 kN. As can be seen in this figure, a large tendon sag can ensure more effective reinforcement.

3.3.3. Effects of different parameters on the load-deflection curve

Initial tendon force, tendon cross-sectional area, and tendon sag have different effects on the load-deflection curve for the RC beam:

1. Effect of initial tendon force. **Figure 6a** shows the load-deflection curves for four different initial tendon forces when the tendon cross-sectional area was 48 mm^2 and tendon sag was 200 mm. An analysis of the curves reveals that an increase in the initial tendon force can increase the RC beam's ultimate bearing capacity and reduce the duration of the hardening stage. Decreasing initial tendon force has the opposite effects. As shortened duration of hardening is not expected for structural performance, a greater initial tendon force does

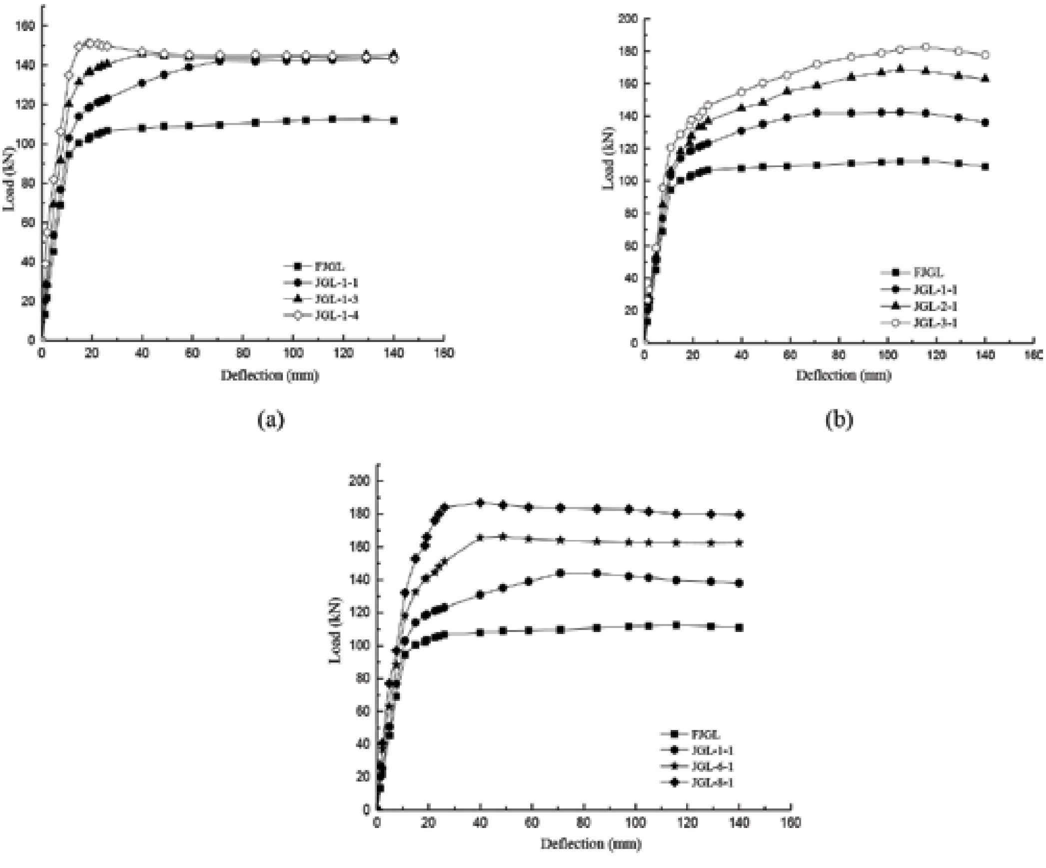

(a) (b) (c)

Figure 6. Effect of different factors on strengthening beam. (a) Initial internal force of cable, (b) sectional area of cable, and (c) sag of cable.

not necessarily mean more effective reinforcement. After the initial tendon force exceeded a threshold (53% in this study), the external tendon will yield and fracture in advance and the RC beam becomes more likely to fail by brittle fracture.

2. Effect of tendon cross-sectional area. When the initial tendon force and tendon sag stay unchanged, there is a positive relationship between tendon cross-sectional area and the structural performance of a balanced-reinforced beam. As the tendon cross-sectional area increased, the structure improved both in yield strength and ultimate strength, and the duration of the hardening stage was extended. **Figure 6b** shows the load-deflection curves for different tendon cross-sectional areas and constant initial tendon force (20 kN) and tendon sag (200 mm). When the tendon cross-sectional area was 48, 86, and 134 mm^2, the RC beam's yield strength increased by 15, 22, and 30%, respectively, compared with that of the unreinforced beam. The corresponding increases in the beam's ultimate strength were 16, 37, and 48%. These results demonstrate significant improvement in structural ductility. According to the concept of an over-reinforced beam, there should be an upper limit on tendon cross-sectional area. This needs to be discussed in future research.

3. Effect of tendon sag. When the initial tendon force and cross-sectional area remain constant, the structural performance of the RC beam tends to vary positively with tendon sag. As the tendon sag increased, the structure showed increases in both yield strength and ultimate strength. **Figure 6c** illustrates the load-deflection curves for a tendon specimen with initial tendon force of 20 kN and cross-sectional area of 48 mm^2. When the tendon sag was 200, 300, and 400 mm, the beam's yield strength increased 15, 29, and 45%, respectively, after the reinforcement. The corresponding increases in its ultimate strength were 16, 33, and 48%, respectively. These results suggest great effect of sag on the beam's bearing capacity. When the tendon sag exceeded a threshold (300 mm in this case, equal to beam height), the duration of hardening experienced by the beam was shortened. Further research is needed to verify if this threshold equals beam height in all cases.

3.3.4. Characteristics of plastic zone development

The analysis above shows that the application of DWM external prestressing not only improved the bearing capacity of the SSB but also altered the plastic zone developed in the beam. **Figure 7** shows the contours of stress in the plastic zone throughout the deformation processes of the unreinforced beam and the RC beam. When the unreinforced beam was subjected to an external load, a plastic zone arose first in the beam segment in the stage of pure bending. As the load increased, the plastic zone tended to expand toward the two ends symmetrically about the midspan position. The height of the plastic zone at midspan gradually increased and always peaked around the midspan. The plastic zone within the segment in shear bending gradually expanded from the loading point to the supports.

In the RC beam, the plastic zone in the region corresponding to the pure-bending segment of the unreinforced beam expanded at a slower rate due to the presence of web members. The plastic zone's height decreased compared to that in the unreinforced beam. Along the beam bottom, it was symmetrically distributed about the midspan web member. As the load

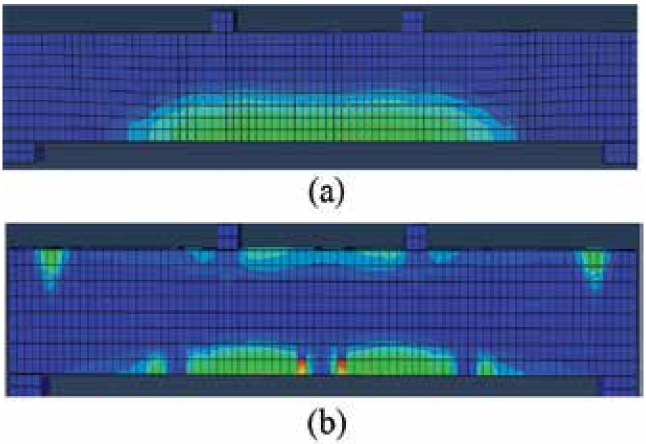

Figure 7. The plastic strain distribution of beam. (a) FJGL and (b) FGL-3-3.

increased, the plastic zone slowly extended toward the top and ends and reached the highest point between web members. The plastic zone area was significantly smaller than that observed in the unreinforced beam. A plastic zone developed at the RC beam top, which is characteristic of deformation of continuous beams. This suggests that after reinforcement, the stress in the beam was redistributed and the properties of the material were used to a greater extent.

4. Tests and results

4.1. Experimental design

Table 1 shows the number of test specimens and their materials. Two parts were prepared for each of the specimens indicated by *. The specimens were divided into three groups. Then "1-" and "2-" were added to the original specimen numbers.

Figure 8 shows the design of the specimens (reinforcement ratio 1.27%). The properties of the rebars, steel wire ropes, and other materials used in the RC beam are presented in **Table 3**. The concrete strength, at 28 MPa, was measured using rebound hammer.

Loading scheme: A three-point bend test was performed on the specimens using a hydraulic servo jack (**Figures 9** and **10**). Each test process was first controlled by load, which increased 10 kN for each stage. After the load reached 100 kN, displacement control was applied, and the displacement increased 5 mm each stage. The loading time was 3 min and the period of sustained load was 30 min.

Observation scheme: (1) observed variables: load, midspan displacement, beam-end displacement, and stress in concrete, wire ropes, rebars, and web members; (2) observation method: measurements by load transducer, displacement meter, and resistance strain gauge and manual measurement record using coordinate paper (rope length change was measured as strain in rope) and calculation using the Hooke's law; and (3) test devices: static strain gauge, ruler, and so on [12].

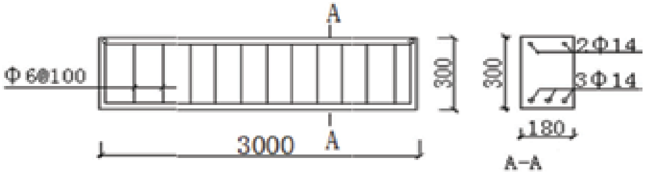

Figure 8. Sectional properties of tested beam (the unit used in the figure is mm).

Name	Diameter Φ (mm)	Density ρ (kg/m^3)	E_s (N/mm^2) × 10^5	Breaking force(kN)	Tensile strength (N/mm^2)
Wire rope	9	/	1.4	75	1550
Wire rope	15	/	1.4	208	1550
Reinforcement	14	7800	1.95	/	400

Table 3. Material properties table.

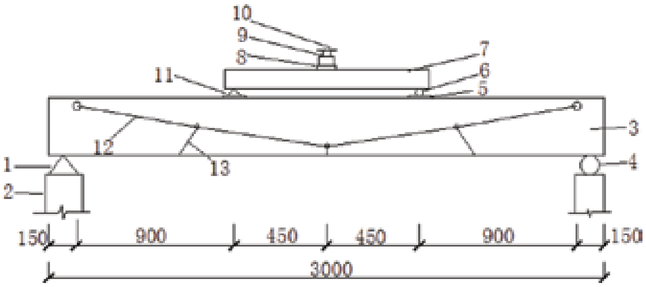

Figure 9. Schematic diagram for loading setup (the unit used in the figure is mm). Notes: (1) fixed hinged support; (2) buttress; (3) test beams; (4) rolling hinged support; (5) backing plate; (6) rolling hinged support; (7) distributive girder; (8) jack; (9) pressure sensor; (10) reaction beam; (11) rolling hinged support; (12) wire rope; and (13) web member.

Figure 10. Load diagram of testing beam.

First, the SSB's mechanical properties before reinforcement were measured, and the results were plotted as load-deflection curves. Stop loading when the maximum fracture width in the concrete in the tensioned region reached 0.2 mm and then unload the specimen. Later, the initial prestressing force was applied to each specimen based on the reinforcement design requirements until the specimen failed.

4.2. Experimental results

4.2.1. Load-deflection curve

Figure 11 compares the load-deflection curves for four specimens before and after reinforcement. When the beam deflection reached 4 mm, specimens 1JGL-1-1, 2JGL-1-1, 1JGL-5-2, and 2JGL-5-2, respectively, showed 29, 30, 41, and 43% increases in load compared to those before reinforcement. For a deflection of 7 mm, the load increased 26, 28, 35, and 37%, respectively, compared with those before reinforcement. The experimental results demonstrate that the specimens became stiffer after the reinforcement.

Figure 12 compares the load-deflection curves for six specimens before and after reinforcement. The fracture strength of specimens 1JGL-1-1, 2JGL-1-1, 1JGL-5-2, and 2JGL-5-2 increased by 21, 26, 38, and 42%, compared to the fracture strength of specimen 2JGL-5-2. Their ultimate strengths were up 13%, 15%, 41%, and 43%, respectively, compared with specimen 2JGL-5-2.

The experimental results show that the reinforcement improved the stiffness of the specimens and resulted in 24 and 40% increases in their fracture strength, 24 and 37% increases in yield strength, and 15 and 42% increases in ultimate strength on average. Specimens with larger tendon cross-sectional areas and sags exhibited better structural performance, consistent with the numerical results.

4.2.2. Failure characteristics

The failure characteristics of the six specimens are presented in **Table 4**. The unreinforced beams were balanced-reinforced. As they failed when the rebars began yielding, their failure mode was ductile failure. The RC beams were divided into two groups: one group with small tendon cross-sectional areas and small tendon sag, and the group with larger tendon cross-sectional areas and larger tendon sags. The rebars all yielded as the tendons failed. The structure ductility was relatively high in both groups. The former group failed before the external tendons fractured, while the latter group failed before the concrete was crushed. This difference demonstrates that large cross-sectional areas and tendon sags in reinforcement design can deliver better results.

4.2.3. Fracture distribution

1-FJGL is an unreinforced beam. When the external load applied to it reached 40 kN, the first fracture arose at midspan. Later, new fractures developed in the pure-bending beam segment at intervals of about 130 mm. A diagonal fracture developed in the shear-bending segment when the external load was 60 kN and continuously propagated upward as the load increased. After the external load exceeded 100 kN, a number of vertical fractures occurred at midspan, resulting in a sharp increase in beam deformation. The load-deflection curve had

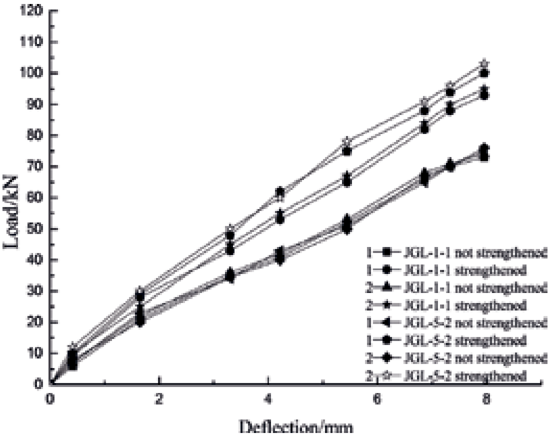

Figure 11. Comparison of bearing capacity between, before, and after reinforcement.

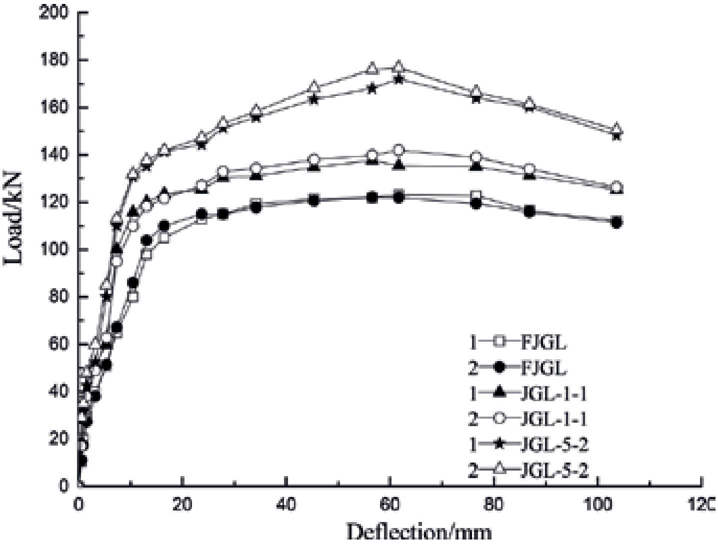

Figure 12. Comparison of load-deflection curves between reinforced beam and unreinforced beam.

only one peak, which corresponded to midspan point in the fractured region on the sides of the specimen (**Figure 13**).

Specimens 2JGL-1-1 and 2JGL-5-2 were loaded until the maximum fracture width reached 0.2 mm. Then they were unloaded and reinforced by a prestressing force. At this point, all fractures in them were closed and the beams formed inverted arches with vertical displacements of 1 mm and 2 mm, respectively.

Beam number	Cable diameter (mm)	Sag of cable (mm)	Internal force of cable (kN)	Cracking load (kN)	Ultimate load (kN)	Failure characteristics
1FJGL	—	/	/	42	124	Ductility
2FJGL	/	/	/	40	115	Ductility
1JGL-1-1	9	200	20	50	136	Broken of cable
2JGL-1-1	9	200	20	53	141	Broken of cable
1JGL-5-2	15	250	30	58	175	Crush
2JGL-5-2	15	250	30	60	180	Crush

Table 4. Characteristic load and failure of beam.

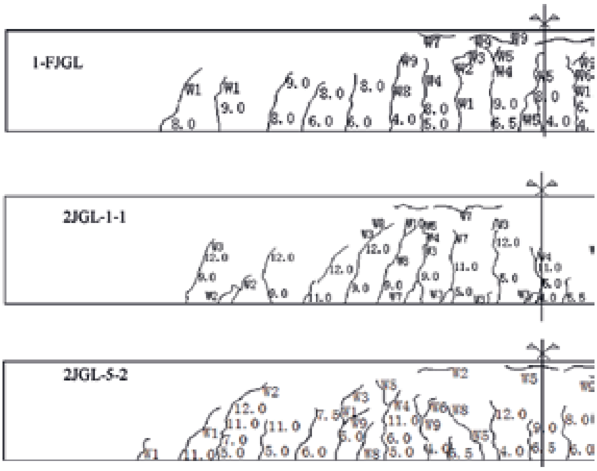

Figure 13. Beam crack mapping. 1-FJGL, 2JGL-1-1, 2JGL-5-2.

Beam number	Yield step		Ultimate load 90%		Displacement ductility ratio (mm)
	Load values (kN)	Displacement (mm)	Load values (kN)	Displacement (mm)	
1FJGL	94	13.5	113	93.9	6.9
2FJGL	99	13.2	116	96.2	7.1
1JGL-1-1	117	14.8	125	146.4	9.9
2JGL-1-1	122	14.1	128	136.2	9.6
1JGL-5-2	133	11.3	152	100.2	8.9
2JGL-5-2	132	10.6	162	85.9	8.1

Table 5. Ductility coefficient of beam.

Specimen 2JGL-5-2. These fracture characteristics of 2JGL-5-2 were similar to those of the previous specimen. Their fracture characteristics differed in two ways: (1) the magnitudes of load at characteristic points were higher than those observed for 2JGL-1-1. For example, the primary fractures opened again when the load was 60 kN and new fractures arose extensively in the shear-bending segment as the load was reached and (2) the four peaks were more obvious in the load-deflection curve for 2JGL-5-2 (See 2JGL-5-2 in **Figure 12**).

The phenomena described above are consistent with the stress contour plots (**Figure 7**), demonstrating the reliability of the analytic method.

4.2.4. Ductility of RC beam

Ductility is an important indicator considered in seismic design for beams. It is usually measured by displacement-based ductility coefficient, μ, [13]:

$$\mu = \Delta u / \Delta y \tag{14}$$

where $\triangle y$ is the displacement when the longitudinal rebars in the beam begin yielding and $\triangle u$ is the displacement when the load is decreased to 90% of the maximum load. The ductility coefficients of the test beams are presented in **Table 5**.

Table 5 reveals that the RC beams had much higher ductility than the unreinforced beams. The specimens with small tendon cross-sectional areas and small initial tendon forces exhibited slightly higher ductility than the specimens with larger tendon cross-sectional areas and greater initial tendon forces.

4.3. Summary

The analysis performed earlier suggests that after being reinforced by DWM external prestressing, the SSB exhibited slightly increased stiffness, improved fracture strength, yield strength, and ultimate strength and significantly increased ductility. This is because the mechanical behavior of the RC beam was constrained by the external prestressing force.

1. It took longer times for the primary microfractures in the concrete to become through-going fractures.
2. The beam formed an inverted arch. When an external load was applied, a part of the load would serve to offset the arch displacement.
3. At a point during the experiment, reinforcement system composed of the external prestressing tendons, web members, and beam-bottom anchorage created a “net bag,” which enclosed the working segment of the SSB and caused redistribution of stress at cross-section.
4. Throughout the experiment, the web members served as an elastic support for the beam bottom and resulted in redistribution of internal force in the SSB. The support force provided by the elastic support tended to increase with increasing external load.

5. Comparison of the theoretical, numerical, and experimental results

Figure 14 compares the theoretical, numerical, and experimental load-deflection curves for specimens JGL-1-1 and JGL-5-2.

Due to the fundamental assumptions mentioned earlier, the theoretical values for the stage of elastic deformation were slightly smaller than corresponding experimental and numerical values, thus ensuring the safety of the specimens. This demonstrates that the theoretical results can accurately describe the mechanical behavior of the specimens and the calculation method is reliable. For the stage of plastic deformation, the theoretical values were significantly greater than the experimental and numerical values, indicating that the theoretical calculation cannot provide reliable guidance.

The experimental data were highly consistent with the numerical data for both elastic deformation and plastic deformation stages, demonstrating the validity of the numerical method proposed.

Figure 15 compares the structural performance extracted from all experimental curves with the structural performance of the beam models observed in numerical analysis. The findings are as follows:

1. The specimens reinforced by prestressing had better structural performance than unreinforced beams.
2. The structural performance curves fit the numerical and experimental data and roughly move in the same manner, thus confirming the numerical results.

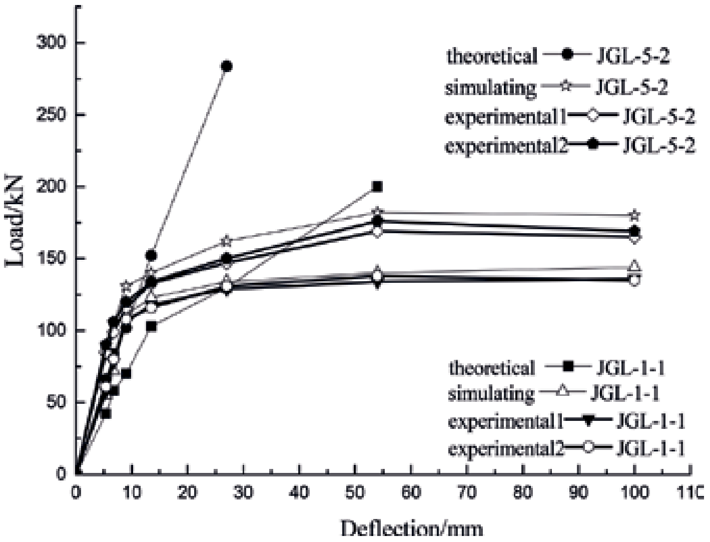

Figure 14. Comparison of theoretical, simulated, and experimental values.

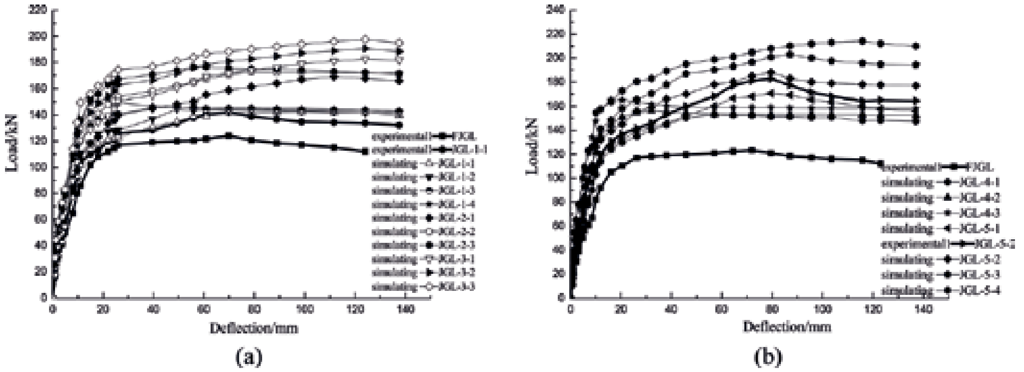

Figure 15. Comparison of simulation value and test value of related specimens. (a) Dip 200 All values contrast and (b) dip 250 All values contrast.

6. Conclusions

1. The load-deflection curve for a RC SSB can be divided into four portions, which correspond to the four deformation stages: elastic deformation, yielding, hardening, and failure. The RC beam specimens failed in two modes: brittle failure of external tendons and ductile failure of concrete in compression.
2. The application of DWM external prestressing results in redistribution of stress at the cross-section of the RC beam, which allows the materials to make greater contribution and improves the beam's structural performance.
3. The theoretical calculation method proposed can deliver reliable results for the stage of elastic deformation and provide a basis for applications in practice.
4. Small tendon cross-sectional areas and high initial stress are not recommended for reinforcement design.

Author details

Teng Wang[1,2]*, Yanmei Ding[1,2], Wangchun Zhang[1,2] and Yu Song[1,2,3]

*Address all correspondence to: wangteng2035@163.com

1 Key Laboratory of Protected Horticulture, Shandong provincial Education Department, Weifang, China

2 Architectural and Civil Engineering Institute, Weifang University of Science and Technology, Weifang, China

3 Western Engineering Research Center of Disaster Mitigation in Civil Engineering of Ministry of Education, Lanzhou University of Technology, Lanzhou, China

References

[1] Yu S. Engineering Structural Detection and Reinforcement. Beijing: Science Press; 2005. pp. 12-15. (in Chinese)

[2] Ting ZY, Jisheng Q, Hengwei H. Survey on research of external pre-stressed concrete beams. Journal of Huazhong University of Science and Technology (Urban Science Edition). 2002;**19**(4):86-91. (in Chinese)

[3] Lou TJ, Lopes AV, Lopes SMR. Influence of span-depth ratio on behavior of externally pre-stressed concrete beams. ACI Structural Journal. 2012;**109**(5):687-695

[4] Ahmed G, Beeby AW. Factors affecting the external pre-stressing stress in externally strengthened pre-stressed concrete beams. Cement and Concrete Composites. 2005;**27**(9-10):945-957

[5] Jinsheng D, Guangda Q. Ultimate stress in external tendons-comments on the existing typical methods. Engineering Mechanics. 2010;**27**(9):63-68 (in Chinese)

[6] He Z, Zhao L, Wang J. A unified algorithm for calculating stress increment of external tendons based on deflection. China Civil Engineering Journal. 2008;**41**(9):90-96. (in Chinese)

[7] Ghallab A, Beeby AW. Calculating stress of external pre-stressing tendons. Structures and Buildings. 2004;**157**(4):263-278

[8] Wu G, Wu Z, Yang W, Jianbiao J, Yi C. Experimental study on flexural strengthening of RC beams with pre-stressed high strength steel wire ropes. China Civil Engineering Journal. 2007;**40**(12):28-37 (in Chinese)

[9] Yu S, Wang Y, Aipeng LI. Internal force analysis of external pre-stressed cable of tilted belly poles. Engineering Mechanics. 2011;**28**(5):143-148. (in Chinese)

[10] Zhu H, Yang Y, Fan W. External Prestressing Bridge Reinforcement Technology Review. International Conference on Engineering Technology and Application (ICETA 2015)

[11] Astawa MD, Raka IGP, Tavio. Moment Contribution Capacity of Tendon Prestressed Partial on Concrete Beam-column Joint Interior According to Provisions ACI 318-2008 Chapter 21.5.2.5 (c) Due to Cyclic Lateral Loads. The 3rd Bali International Seminar on Science & Technology (BISSTECH 2015)

[12] Xu L, Xu F, Hao Z, Wenke Q. The design and test study on pre-stressed railway concert beam -bridge strengthened by externally draped CFRP tendon. Engineering Mechanics. 2013;**30**(2):89-95. (in Chinese)

[13] Vasudevan G, Kothandaraman S. Experimental investigation on the performance of RC beams strengthened with external bas at soffit. Materials and Structures. 2014;**47**(10):1617-1631

Section 4

Vibration Control

Vertical Natural Vibration Modes of Ballasted Railway Track

Akira Aikawa

Additional information is available at the end of the chapter

http://dx.doi.org/10.5772/intechopen.79738

Abstract

Impact loads from running trains induce natural vibration within the ballast layer, which causes ballast deterioration over time. This study measured the natural vibration characteristics of the ballast layer using field measurements, full-scale impact loading experiments and large-scale finite element analysis. Experimental test results indicate that the vibration components in the high-frequency range are dominant in ballast responses under loading and that ballast motions during unloading are mainly induced by vibration components in the low-frequency range, causing large displacement over a long duration. Numerical results indicate that the normal frequency of the vertical elastic vibration mode is detected at approximately 310 Hz and that the rigid-body bounce mode of the ballast layer occurs at one-third of the elastic vibration mode frequency. They coincide substantially with values held by field measurements. Stress acting on the angular part of the ballast is more than 1000 times greater than the average loading stress under the sleeper bottom. The combined structure, which consists of the ballast layer and sleepers, vibrates easily in synchrony with resonance motions induced by the impulse waves. Improvement of the contact condition on the sleeper bottom is expected to decrease the displacement amplitude of ballast gravel, thereby reducing ballast degradation.

Keywords: impact loads, natural vibration of granular layer, full-scale impact loading experiments, tensionless analysis

1. Introduction

A ballasted track is characterized by its structure, with a ballast layer sandwiched between sleepers and a roadbed, which greatly reduces impact loads generated by dynamic rolling—contact interaction between the wheels and rails. However, this benefit has an adverse effect:

The ballasted tracks are structurally prone to deteriorate over time. They absolutely require periodic maintenance work and repair. Recently, many attempts were made to improve the ballasted track structure. For example, many types of elastic and/or viscoelastic structural members, such as rail pads, under-sleeper pads and under-ballast mats, were attempted to reduce ballast degradation [1–3]. In one experimental investigation, the sleeper's vibration characteristics, including the dynamic effects of sleeper/ballast interactions, were investigated through a modal analysis to predict the railway track's dynamic response [4]. Dynamic wheel/rail interactions, which significantly contribute to impact vibration and noise, were also investigated for rail and wheel surface defects in field measurements and numerical simulations [5–8]. When considering the future of the railway management, it is impossible to disregard the necessity for frequent maintenance that is dependent upon manual aid. Therefore, the need exists to improve maintenance methods for the ballasted track based on findings from empirical and numerical investigations of the dynamic response characteristics and deterioration factors of the ballast layer.

Running trains cause dynamic loads mainly through two mechanisms [9, 10]. One is the dynamic load from passing axle loads as a train passes. The related frequency characteristics, which depend on the number of axles passing per unit of time, are limited to low frequencies of only several Hertz to approximately 30 Hz. The other mechanism is the impact load that is generated dynamically by the rolling contact mechanism between the wheels and rails. The ballast layer transmits this sharp pulse-shaped impact load superimposed on the low-frequency loads from passing axles. This waveform, when transformed into a frequency domain, exhibits numerous vibration components with broadband characteristics that extend from low frequencies to several kilohertz. That is to say, dynamic response measurements of the ballasted track require high-precision measurements of vibration components ranging broadly from several Hertz to several kilohertz. Outputs of sensor would be degraded by noise of tens of millivolts deriving from the inductive currents of high-voltage overhead cables in conventional field measurements, which necessitated the use of a low-pass filter to alleviate that interference. Ensuring the measurement accuracy of high-frequency vibration components exceeding 50–100 Hz was impossible under such conditions. For that reason, no comprehensive discussion of these components has been reported in the literature to date.

This chapter gives accurate field measurements of the dynamic responses of the ballasted track with a train passage at a sampling frequency of 10 kHz without low-pass filters, using special sensing sleepers and sensing stones produced by the authors [11, 12]. Using the measurement effects, the analysis can be done with a focal point on propagation characteristics of dynamic loads inside the ballast layer and vertical natural modes of the ballast layer. Moreover, the author conducted a free fall-weight impact loading test on a full-scale mock-up of a ballasted track to ascertain the response motions of the ballast layer, with high rapidity and with high accuracy, in the high-frequency region immediately after the impact load was used [13]. Furthermore, using a direct solver MUMPS [14–17] corresponding to large-scale parallel computing of a distributed memory type, according to finite element transient response analysis FrontISTR [18] and Advance/FrontSTR [19] based on a fine ballast aggregate model, both the elastic natural vibration mode and the rigid-body bounce natural vibration mode of the granular ballasted layer are simulated numerically.

2. Rigid-body bounce vibration mode and elastic natural vibration mode

In general, a dynamic load propagates as an elastic wave through the interior of an object, consequently inducing the natural vibration modes specific to the object, which can be applied to the ballasted track composed of the ballast aggregate. Although the ballast layer is a discontinuous structure, it presumably has natural vibration modes that are specific to the ballasted track. **Figure 1** shows some characteristics of the principal natural vibratory motions in the vertical direction of the ballast layer [20]. One characteristic is the rigid-body bounce natural vibration mode. Another is the elastic shrinkage natural vibration mode. The ballasted track structure represents a single degree of freedom system that includes sleepers, rails and other components which constitute the track structure mass, along with the ballast layer and roadbed which constitute the spring rigidity component. In the bounce natural vibration mode, this single degree of freedom system moves vertically and rigidly under a train's dynamic load. The ballast layer acts as an elastic one-directional spring in the vertical direction. Rigid-body natural vibration modes of six kinds exist: They are translational and rotational along each of the three axes. In both the dynamic loads applied to the ballast layer and in the responses of the ballast layer, the translational vibration components in the vertical direction are predominant.

Therefore, this research specifically examines the translational bounce behaviour in the vertical direction. According to the dynamics, the natural frequency of the first-order rigid-body bounce mode f_1 is given theoretically as $f_1 = \sqrt{k/m}/(2\pi)$, where k and m, respectively, denote the ballast stiffness and overburden mass of the track structure. This mode reportedly exists at approx. 100 Hz [21].

The elastic vibration mode is the motion by which the whole ballast layer shrinks and stretches vertically as an elastic body. This natural vibration mode is considered not to occur in a normal-state ballast layer but to occur when the ballast layer is under high confining pressure generated by the train's weight applied to the layer. To date, no report of the relevant literature has described a study conducted to capture this mode, that is, ballast motion in the frequency domain related to this mode. Moreover, on a real track, natural vibration that

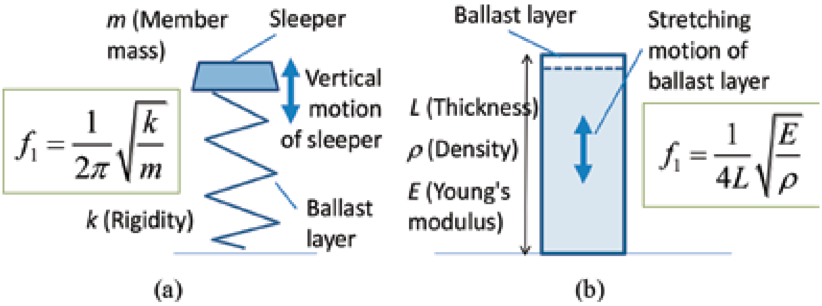

Figure 1. Principal vertical natural vibration motions of the ballast layer. (a) Rigid-body bounce mode, (b) elastic shrinkage mode.

entails bending deformation and torsional deformation of the members occurs. According to the physical theory related to standing waves on the railway track, the natural frequency of the elastic first-order vibration mode f_1 is given theoretically as $f_1 = \sqrt{(E/\rho)}/(4L)$, where E, ρ and L, respectively, denote the ballast layer's Young's modulus, density and thickness.

3. Vibration tests by the use of a full-scale mock-up

The author built a full-scale mock-up of the ballasted track structure and investigated natural vibration characteristics of the ballasted track by performing an experimental modal analysis based on impulse excitation tests.

Figure 2 shows the profile/plane of the mock-up and the sensor positions [22–24]. To build the full-scale mock-up, the author employed new ballast using hard andesite, which complies with the same standard for the real track. They were compacted sufficiently. Type 3 prestressed concrete (PC) monoblock sleepers were used for the mock-up. They are used widely for the metre-gauge (1067 mm-wide) railway lines that are conventionally used for Japan Railway Companies. For the prevention of interference of vibration effects of the concrete frame, urethane foam panels were sandwiched between the mock-up and the outer concrete frame. The author installed acceleration sensors on the mock-up and the concrete frame, vibrated the mock-up and ensured that the vibrations were sufficiently isolated to assess the vibration-insulating properties. The author conducted tests by hitting the end of the sleeper laterally, longitudinally and vertically with an impulse hammer to make it vibrate. Test records included measurements of the acceleration responses: 22 sleeper locations and several ballast layer locations. From those data the accelerance was calculated: the transfer functions of the acceleration responses to the excitation force in the frequency domain. Then

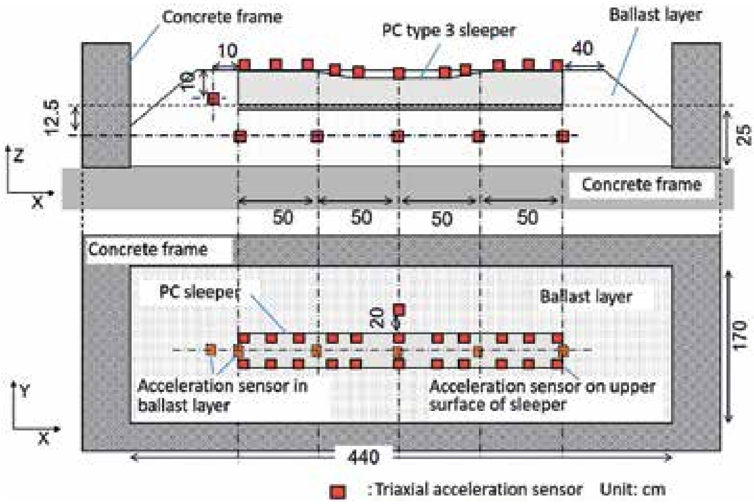

Figure 2. Overview of full-scale vibration test.

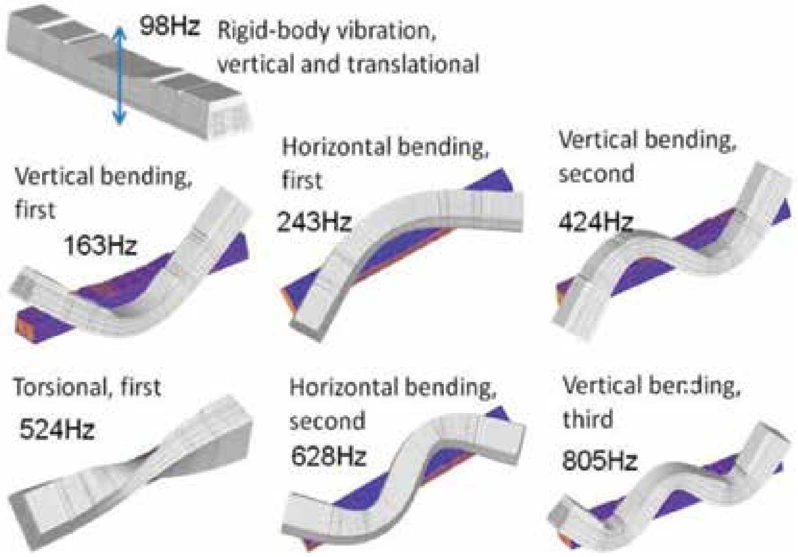

Figure 3. Mode shapes of natural vibration acquired from test results.

experimental modal analysis was conducted considering the location relations of the measuring points. As a result, for the ballasted track, the author was able to identify the natural vibration frequencies and their modal shapes between the low-frequency domain and 1 kHz.

Figure 3 presents the natural vibration frequencies and the specific modal shapes of the ballasted track that were acquired from the test results [22–24]. Although there are rigid-body vibration modes of six types as described above, the figure shows only the rigid-body translational mode in the vertical direction. It also shows that the vertical and translational rigid-body vibration is generated at 98 Hz, which agrees well with earlier reported research results. Furthermore, six types of dominant natural vibration mode entailing the bending and torsional deformations of sleepers are identified as shown in the same figure. Nevertheless, the author was unable to capture any vertical elastic natural vibration mode of the ballast layer in this test. That is true probably because the elastic vibration modes of the whole ballast layer would occur only when the ballast layer continuity is sufficiently satisfied according to the train loads on the ballast layer.

4. Field measurements and spectral analysis

Dynamic responses were measured on an actual ballasted track of a main conventional railway line in Japan to identify the dominant natural vibration modes of the ballasted track. The track structure at the measurement site, consisting of continuous welded rail weighing 60 kg/m and type 3 PC sleepers, was designed based on the Japanese standard [25], which allows a running speed higher than 130 km/h. The measurement site was located on a solid embankment in a straight section. For spacing between the sleepers, 41–42 sleepers are positioned over a distance of 25 m. The author chose a straight section with satisfied track conditions, based on measurement data from an inspection car. The ballast layer at the measurement site is made of new andesite hard stones with clear-cut edges. The ballast layer is approx. 30 cm thick.

Figure 4 presents an overview of sensor positions. Details of the measurements are described in earlier reports of the literature [26, 27]. This article specifically examines the measured responses for a passenger train moving at approx. 120 km/h (sampling frequency is 10 kHz). The sleeper vibration acceleration and the ballast vibration acceleration were measured using piezoelectric triaxial acceleration sensors: 10 mV/G sensitivity, 500 G measurement range and 2–10,000 Hz frequency range within 5% deviation. The ratio of noise to the maximum measurable acceleration is approximately 0.002%. The acceleration sensor also offers an appropriate level of performance to enable measurement for the determination of load characteristics in a high-frequency domain. The following analyses were conducted by obtaining linear amplitude spectra by application of fast Fourier transformation of the time history response waveforms in response to vibration accelerations, with smoothing at a 20 Hz bandwidth.

Figure 5 shows a special sensing sleeper designed to assess the dynamic load distribution on the sleeper bottom, for a wide frequency range from a low frequency of 0.01 Hz up to a high frequency of several tens of kilohertz. The sensing unit comprises a type 3 PC sleeper fitted with many ultra-thin-type impact load sensors. Attached to the sleeper's whole undersurface is a solid mass comprising 75 impact load sensors (25 pieces × 3 rows). Each impact load sensor has a main body and cover members. The main body including a piezoelectric film has solid cover plates on both surfaces. The cover plates (8 cm × 8 cm) transmit impact load to the main body in cases of impact loads of a running train, thereby preventing sensor breakage [12, 27]. Each sensor can measure a load up to a maximum of 10 kN. The sensor has thin metal plates attached to both sides of a thin piezo-film. The structure, which resembles that of a condenser, has no internal resistance. For that reason, no current is induced by noise sources, even in the electromagnetically high-tension environment that prevails during train operation. This

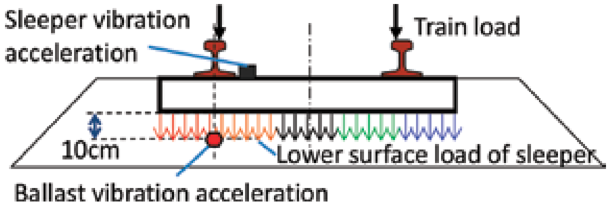

Figure 4. Measuring sensor positions.

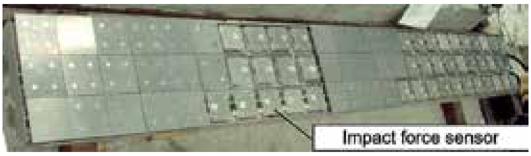

Figure 5. Overview of sensing sleeper.

feature enables high-quality load measurement. Both terminals output a charge that is proportional to the impact load, but digitization of the charge output is extremely difficult. For that reason, the charge from the sensor is usually converted into a voltage by integrating the electric circuit attached to a sensor output terminal (charge amplifier). For that purpose, an impedance transformation circuit with extra-high impedance, ultra-low noise and differential input-type operational amplifiers (OP-amps) can be used for the instrumentation preamplifier. Moreover, this sensor has good reactivity. Because the output voltage can be as high as several tens of volts, the ratio of noise to the maximum measuring load is as low as 0.003%. The sensor can measure load characteristics at high frequencies.

Figure 6 shows the acceleration amplitude spectrum and the displacement amplitude spectrum of the ballast gravel at 10 cm depth. The acceleration spectrum shows that components at frequencies higher than 100 Hz as well as the low-frequency components contribute greatly to the ballast response. These high-frequency vibration components are attributable to the sharp pulse-shaped impact loads induced by the dynamic mechanisms between the wheels and rails.

When particularly addressing the ballast displacement, its amplitude is extremely small in the high-frequency domain. For instance, the displacement amplitude is only 1/1000 μm at a frequency of approx. 800 Hz, which is equivalent to the natural frequency of the ballasted track entailing the third mode of the vertical bending of the sleeper. Therefore, the vibration components in the high-frequency domain are not transmitted by rigid-body vibrations around the centre of gravity of the ballast gravel, but the dynamic loads are transmitted through the elastic undulation propagation because of the local and minute deformation behaviour and sliding behaviour at the tips of the edges of contact points between the ballast stones. However, the displacement amplitude in the low-frequency domain from several Hertz to 20 Hz is several thousand times higher than those in the high-frequency domain. Consequently, the loads in the low-frequency domain are transmitted mainly through rotational and translational rigid-body vibrations of the individual ballast gravel particles. This figure also depicts peak profiles of responses related to the natural vibration modes of the

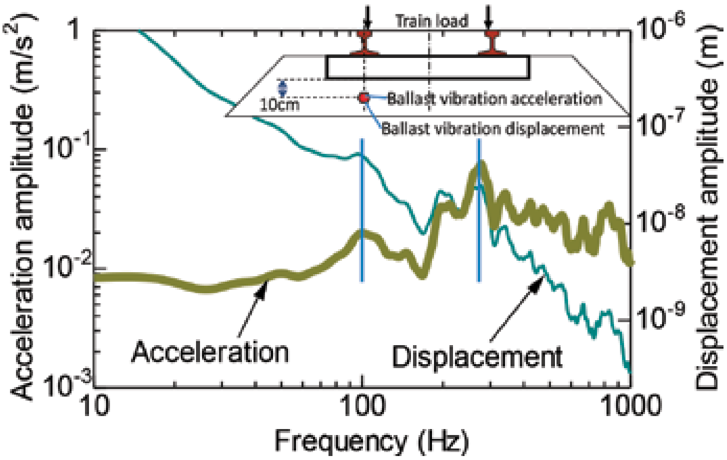

Figure 6. Acceleration and displacement amplitude spectra of the ballast (measured).

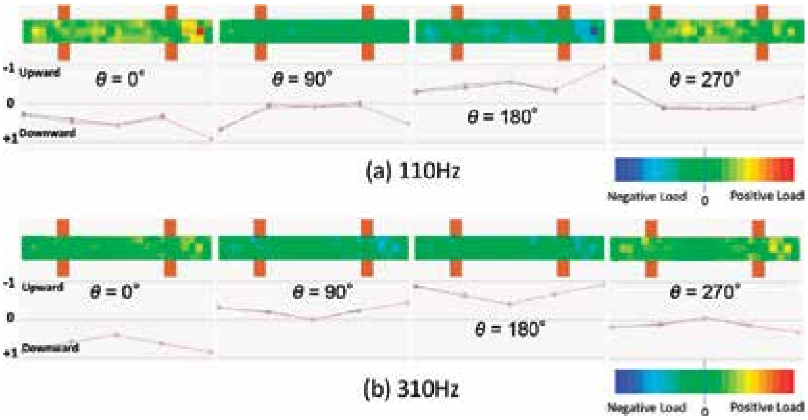

Figure 7. Distribution of vertical loading at the bottom of the sensing sleeper and normalized displacement at the top of the sleeper (measured).

ballasted track explained in the preceding paragraph. These curves identify the rigid-body resonance mode of the ballast layer around 100 Hz and indicate another large peak profile at around 300 Hz. From the full-scale experiment presented in **Figure 3**, the rigid-body natural vibration mode of the ballasted track appears at 98 Hz.

Figure 7 shows the relation between the two-dimensional distribution of the vertical loading on the bottom surface of the sleeper and the normalized vertical displacement of the sleeper in cases of two frequencies (110 and 310 Hz), which give the peak profiles of the response curves. In the figures, θ denotes the relative phase angles with reference to vertical motion at the centre of the sleeper. In the distribution maps, red denotes the positive load (compression). Blue shows the negative load (tension). Regarding the sleeper motion, the downward direction indicates the downward behaviour of the sleeper. The upward direction indicates the upward behaviour of the sleeper. Panels (a) and (b) show that the sleeper repeats a vertical periodic movement at these frequencies, entailing bending deformation of the sleeper at high frequencies, in synchronization with the phase angles.

5. Drop-weight impact loading test

The author repeatedly performed drop-weight impact loading tests using a full-scale mock-up of the ballasted track, dropping a steel weight from a given height and applying impact loads having a sharp pulse shape directly to the track structure. **Figure 8(a)** presents an overview of the test device. **Figure 8(b)** depicts the positions of sensors used for the measurements. The test setup consists of a 30 cm-thick ballast layer built with new andesite ballast gravel on a concrete roadbed. A track structure was built using three pieces of type 3 PC sleepers and two pieces of rails weighing 60 kg/m. The steel weight frame, positioned over the sleeper at the centre, was dropped repeatedly from the given height to apply impact loads to the track structure. Measured data for the magnitude of the impact loads, the vertical displacement of

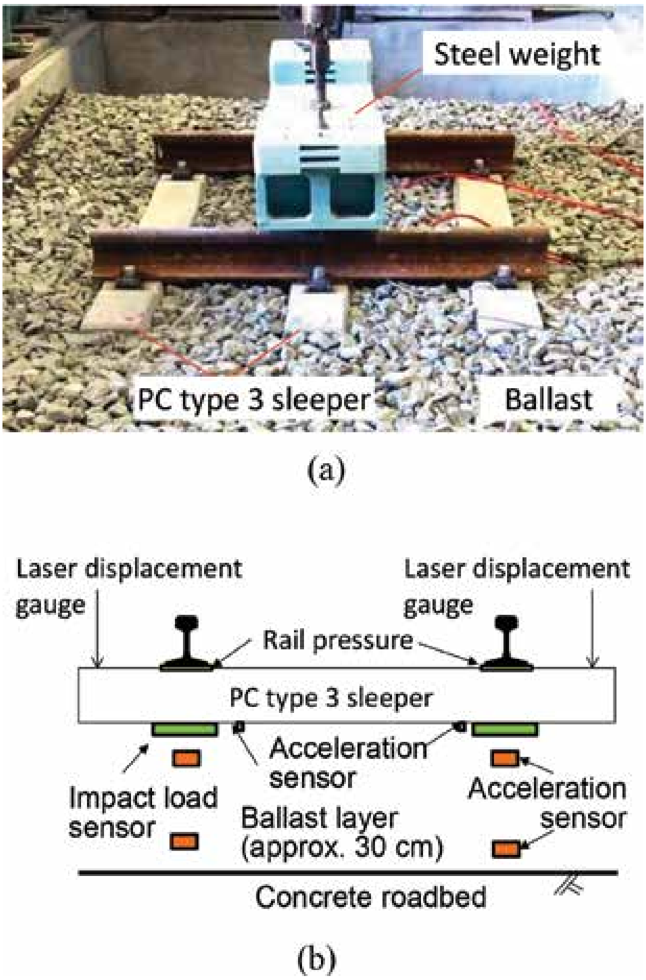

Figure 8. Overview of impact loading test. (a) Drop-weight impact test device, (b) sensor positions.

the sleepers and the acceleration responses of sleepers and ballast were recorded by sampling the data at 10 kHz or 20 kHz. This chapter presents a discussion of the measurement results of the displacement responses of the sleepers [9, 13].

Figure 9(a) shows the time history response of the centre sleeper's vertical displacement after impact loading. This average curve shows results obtained from about 4000 loading tests, excluding initial loading of the first 1000 iterations. The downward displacement in the chart shows the ballast layer compression. The upward displacement represents extension of the ballast layer. **Figure 9(b)** especially depicts data obtained at the moment immediately after loading. The average value of the impact load on the ballast through the left and right rails was 217 kN. The figure shows that because of the compression applied by an impact load, the ballast layer instantaneously deforms elastically. The compression produces maximum downward displacement of 0.178 mm in 0.71 ms. Subsequently, it returns to the preloading

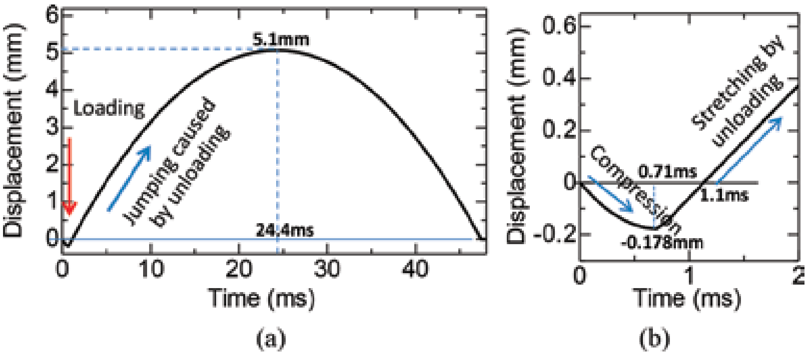

Figure 9. Vertical displacement of sleepers immediately after impact loading. (a) Sleeper displacement, (b) close-up of displacement.

position in 1.1 ms. Results show that only about 1 ms is necessary for the ballast layer compression and restoration. Displacement responses of the sleeper and load during that time include few vibration components at low frequencies.

Following the compression and restoration motions of the ballast layer, sleeper-jumping occurs. The average jumping speed is approximately 1.71 times as high as the average of the compression speed. Their initial speed can be approximately 12.1 times faster than the average compression speed. The jumping height of the sleeper reaches 5.1 mm in 24.4 ms. The sleeper returns to the initial position within 46.7 ms after loading. The jumping behaviour during unloading includes no high-frequency vibration component. Most of the vibration comprises low-frequency components. The author posits that the cause of sleeper-jumping is the abrupt release of the strain energy stored in the ballast.

Figure 9, as described, presents the vertical displacement of the sleeper. Presumably, similar behaviour occurs in the upper part of the ballast layer immediately under the sleepers, which means that the motion under impact loading is extremely slight. The compression and restoration behaviours are high-frequency responses that last for a very short time: about 1 ms. Therefore, high-frequency vibration components are dominant in ballast responses under loading. However, ballast motions during unloading are induced mainly by low-frequency vibration components that cause large displacement and which last longer.

6. Ballast layer modeling

Three-dimensional shape measurement was performed to ascertain three-dimensional vertex coordinates of more than 4000 ballast gravel pieces. Based on the measured coordinates, each shape was expressed using a polyhedral rigid-body discrete element model and was converted into aggregate, with the same size and the same shape, of the tetrahedron secondary elastic finite elements. Details of the measurements were presented in an earlier report [28]. **Figure 10** presents some exemplary images of a ballast gravel piece and its numerical discrete element and finite element models. Regarding the finite element models, a sufficiently fine

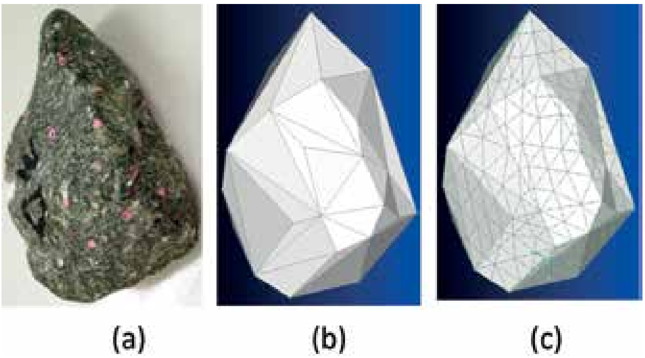

Figure 10. Exemplary pictures of existing ballasts and the digitized models. (a) Ballast, (b) DEM model, (c) FEM model.

mesh size of 1 cm was adopted to support the precise representation of natural frequencies of individual ballast gravel up to several 10 kHz.

Regarding the physical properties of the ballast, density ρ = 2700 (kg/m^3), Young's modulus E = 30 (GPa), Poisson's ratio ν = 0.2 and structural damping parameter η = 0.01 are adopted. The ballast gravel density was the laboratory experimental value obtained from specific gravity tests. The Young's moduli and Poisson's ratio were referred or derived from previous reports of the literature. Regarding the structural damping coefficient, the author adopted general values of a concrete structure.

Figure 11 presents a procedure for the creation of the ballast aggregate using both discrete element and finite element modeling. First, about 100 pieces of the ballast polyhedron discrete element models with different shapes and sizes were placed randomly in the air above rectangular box frames of 20 cm width and length. The gravel was then dropped freely with gravity and was compressed vertically with a loading plate using discrete element software. Next, all individual polyhedron discrete element models were converted into assemblages consisting of the small finite tetrahedron second-order elastic solid elements and split into 1 cm meshes with geometry and contact point information maintained. Each polyhedron discrete element model was divided into approximately 1000 tetrahedron finite elements. The finished rectangular block model has 20 cm width and length, with 17 cm height, and has more than 90,000 tetrahedron finite elements.

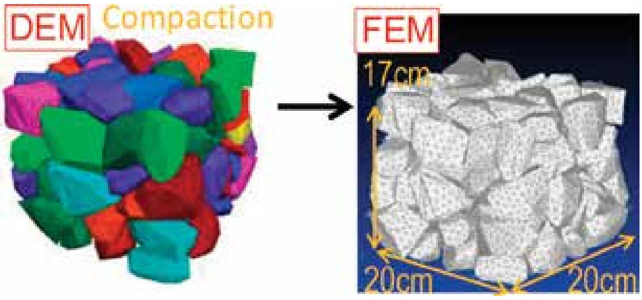

Figure 11. Compaction and modeling of the ballast aggregate with MPCs.

For this procedure, the contact points were mutually connected through multipoint constraints (MPCs), which connected the nodes of elements in three axial directions related to the contact pair of blocks at each contact point. The provided contact-connectivity exhibited no expansion or contraction because it was several tens of thousands of times harder than that of ballast pieces. Accordingly, the spring functions around the contact points were represented by the elastic deformation of the ballast angularities, which were composed of the assemblages of several tetrahedron finite elements adjacent to the contact points.

Figures 12 and **13** present a finite element model of a type 3 PC monoblock sleeper developed by the authors [24] and consisting of 51,146 nodes and 51,944 solid elements. The sleeper model can make a precise representation of all natural frequencies described above, with their response values up to 1 kHz within 5% deviation. Its physical weight is 161.40 kg. Its volume is 0.0677 m^3.

A large-scale finite element model was constructed with multipoint constraints (MPCs) by assembling 48 units of the rectangular unit block models of the ballast described above and

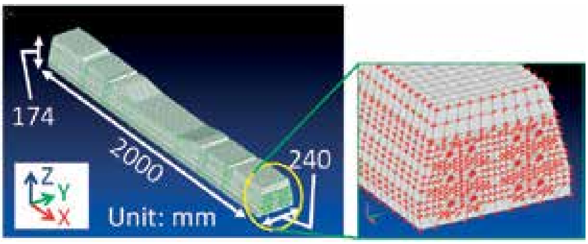

Figure 12. Model of a type 3 PC sleeper.

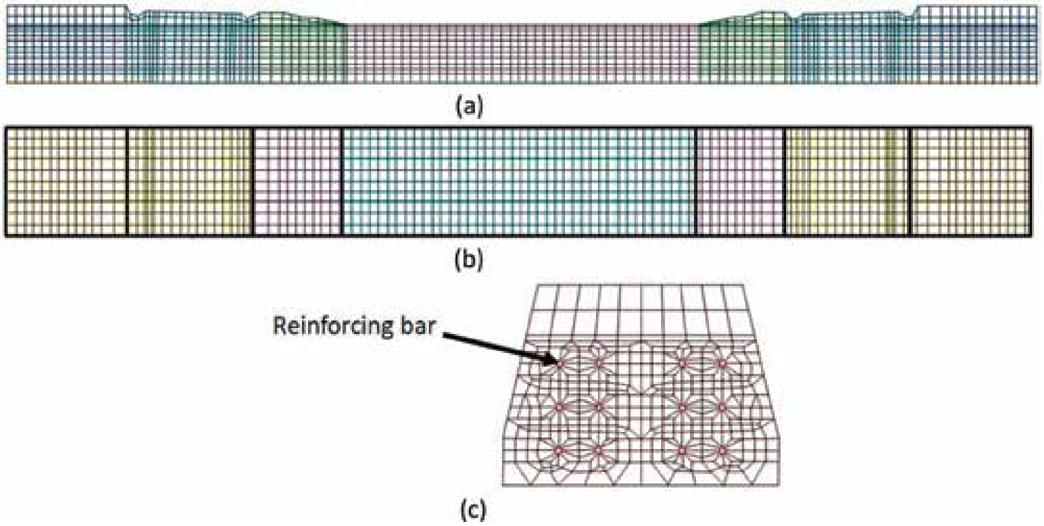

Figure 13. Model of a type 3 PC sleeper. (a) Side view, (b) top view, (c) end face and reinforce bars.

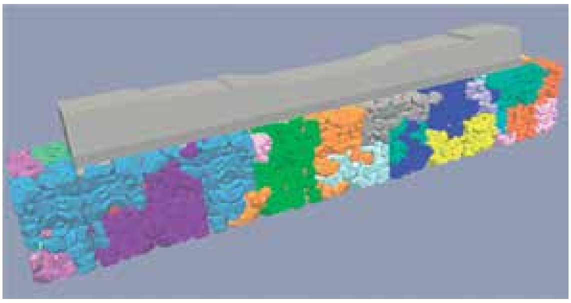

Figure 14. Assembly of ballasted track model and domain segmentation for large-scale parallel computing.

Item	Young's modulus (GPa)	Poisson's ratio	Density (kg/m^3)
Ballast	30	0.200	2700
Concrete	45	0.167	2350
Steel	210	0.290	7820

Table 1. Calculation parameters.

the type 3 PC sleeper model. **Figure 14** presents finished analysis model and its domain segmentation for large-scale parallel computing by the finite element programming code of FrontISTR. The model consists of 7.05 million nodes and 4.15 million second-order solid elements. The degrees of freedom of the model exceed 21 million. By adopting the finite element analysis using the precise model of the ballast layer having a complicated structure, it is possible to reproduce phenomena such as stress concentration and wave propagation within the ballast layer rapidly, easily and exactly. The entire model is divided into 24 sub-domains to introduce the direct solver MUMPS corresponding to the parallel computing of a distributed memory type. By applying the finite element normal-mode analysis by FrontISTR, a set of normal modes related to the ballast aggregate and sleeper system is obtained. Specifications related to the various parameters of each model are presented in **Table 1**.

7. Large-scale finite element transient response analysis of the elastic vibration mode of the ballasted track

The time history response waveforms were calculated numerically by inputting the measured loading waveforms to the top surface of a sleeper model when a passenger train moved over the top surface of the previously described ballasted track model.

Figure 15 displays the actual waveforms of vertical loading (measured in cross-sectional area of 14 cm width and 18 cm length on the bottom surface of the rails) applied by the first axles of a lead coach bogie when the passenger train moved through the test section at about 120 km/h [26, 27].

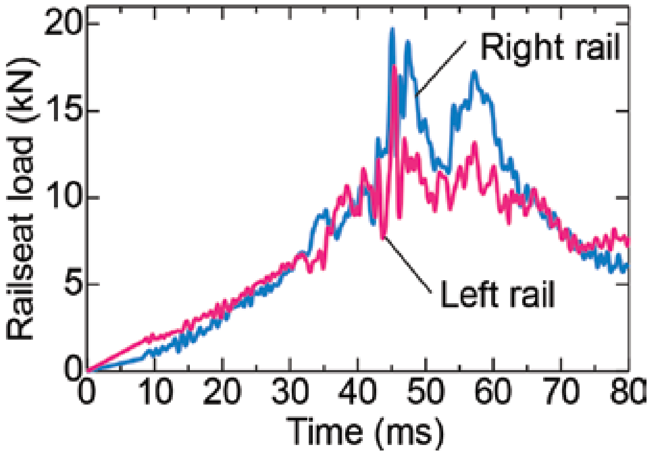

Figure 15. Measured rail seat loads.

The figure shows that the axles passed immediately above the sleeper centre at around 55 ms. Finite element analysis shows that the measured time history waveforms are uniformly input to all nodal points located within the bottom area of the rails on the top surface of the sleeper model. The calculation time interval is set at $\Delta t = 0.1$ (ms). The total calculation steps are 800.

Figure 16 portrays the distribution of the response nodal displacement of the ballast aggregate and the sleeper system at $t = 55.0$ (ms) when the load peaks appeared as the first axle of the lead coach bogie that passed above the sleeper centre. It is apparent that the dynamic displacement induced by a passing train on the ballast is not distributed uniformly throughout the ballast aggregate and the sleeper. Significant displacement is concentrated locally around the rail positions. Analytical results demonstrate that 30 μm maximum downward displacement occurred.

Figure 17 depicts the time history waveforms of response of the von Mises stress on the cross-section inside the gravel angle acting on three contact points, each with some angularity, of the ballast gravel placed at different depths below the loading point of the left rail location. As the figure shows, the stresses in the gravel increase gradually, alternately repeating the minute

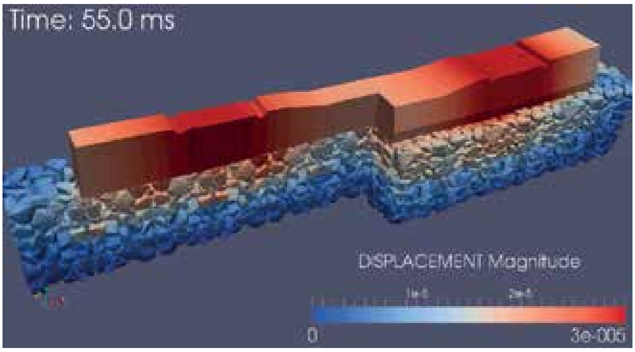

Figure 16. Distribution of nodal displacement ($t = 55.0$ ms).

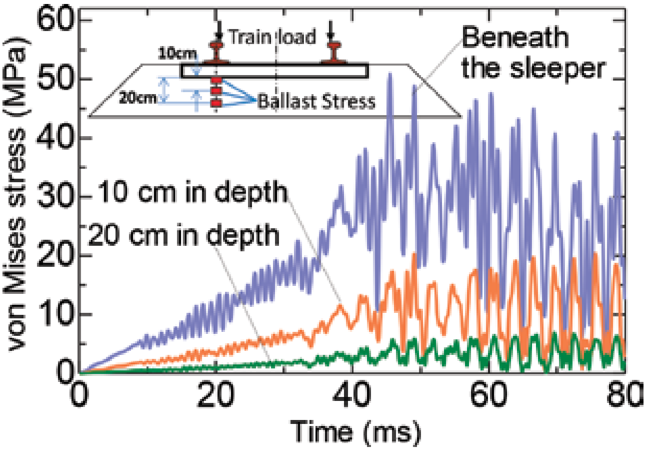

Figure 17. Time history of on Mises stress.

upward (compression) and downward (tension) motions at a frequency of approximately 300 Hz, according to the inputted loads. In this case, the maximum stresses of approximately 50 MPa after elapsed time of about 45–53 ms are observed near the ballast surface beneath the sleeper bottom. It is apparent that the rise in the peak response value becomes gentler as the measurement point becomes increasingly distant (i.e. deeper) from the loading point. A tendency exists for waveforms to become smoother along with the steep decrease in high-frequency vibration included in the wave. Although the investigation reported here involves elastic body analysis without the use of any constitutive equation, the diminishing trend of energy inside the ballast is reproduced closely by simulating the ballast aggregate structure in detail. Results show that the ballast aggregate structure featuring angular parts has the mechanism of energy attenuation.

Figure 18 portrays linear amplitude spectra of response of the von Mises stress on the cross-section inside the gravel angle acting at different depths below the loading point of the left rail, as obtained by conducting fast Fourier transformation of these time history response waveforms and smoothing them at a 20 Hz bandwidth. As the figure shows, these spectra curves identify the first-order elastic vibration resonance mode of the ballast layer at around 337 Hz, where the whole ballast layer stretches vertically as an elastic body.

To detect the exact frequency of the elastic vibration mode of the ballast layer, the author conducted a numerical experiment (simulation), which simulates the impulse loading experiment using a transient response analysis of the previously described large-scale sleeper-ballast aggregate model.

Figure 19 shows the amplitude spectra of response of the vertical displacement of the sleeper by application of a 0.1 ms square waveform of impulse loading. Impulse loading to the left and right rails totals 100 kN. Results of the numerical experiment of the impact loading indicate that the rigid-body natural vibration mode occurs at around 310 Hz. Results show that the analytical natural frequency of the elastic vibration mode of the ballast layer more or less coincides with the measured one described above and that the frequency corresponds to three times the value of the measured natural frequency of the rigid-body mode.

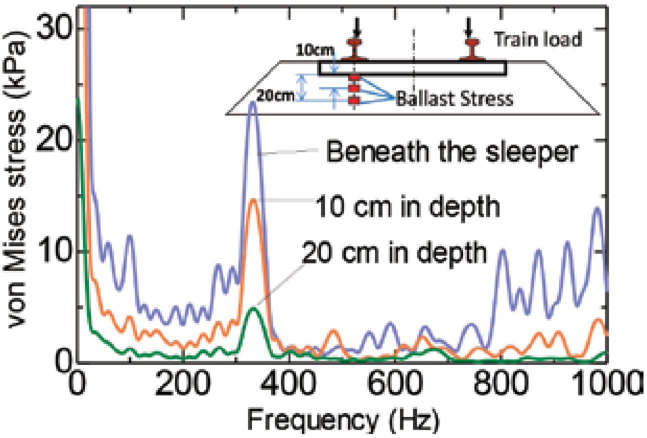

Figure 18. Response spectrum of the von Mises stress.

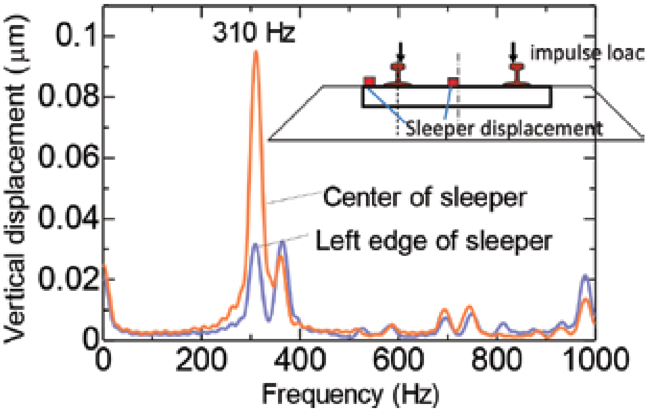

Figure 19. Response spectrum of vertical displacement regarding impulse loading.

8. Large-scale finite element transient response analysis related to the rigid-body vibration mode of the ballasted track

To examine the dominant rigid-body resonance motion around 100 Hz, this chapter presents a description of the large-scale finite element transient response analysis of the ballasted track using nonlinear contact springs (i.e. tensionless springs) in place of the MPCs. Results of the drop-weight tests described above suggest that the jumping motion of the ballasted track, the rigid-body bounce mode, will cause large displacement. Therefore, regarding the previously described large-scale finite element model of the ballasted track, information of the contact points between the ballast pieces and the sleeper nodes is modeled with nonlinear contact springs, that is, with tensionless contact. **Table 2** presents parameters of calculations related to contact points. In this analysis, the tension spring factors are set at 1/100,000 values of the compression spring factors.

Item	Compression spring factor (GN/m)	Tension spring factor (GN/m)
Ballast-ballast	30	0.0003
Sleeper-ballast	10	0.0001

Table 2. Calculation parameters related to contact points.

With finite element analysis, the measured waveforms of the rail seat load were inputted to the top surface of the sleeper model using tensionless springs. **Figure 20** presents the nodal displacement distribution of the ballast aggregate and the sleeper system at *t* = 55.0 ms when load peaks appeared immediately after the first axle of the lead coach bogie passed above the sleeper centre.

Figure 21 depicts time history waveforms of the response of the von Mises stress on the cross-section inside the angular part of the gravel under the left rail. As the figure shows,

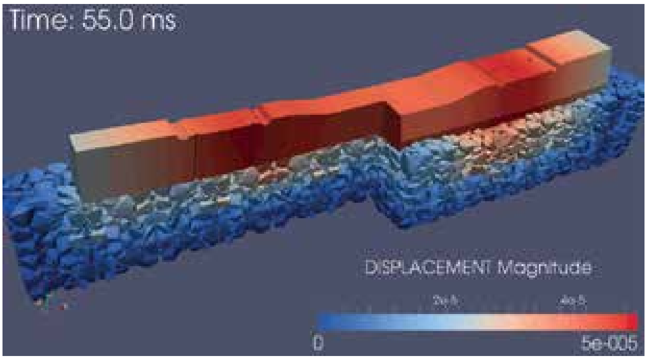

Figure 20. Distribution of nodal displacement (*t* = 55.0 ms).

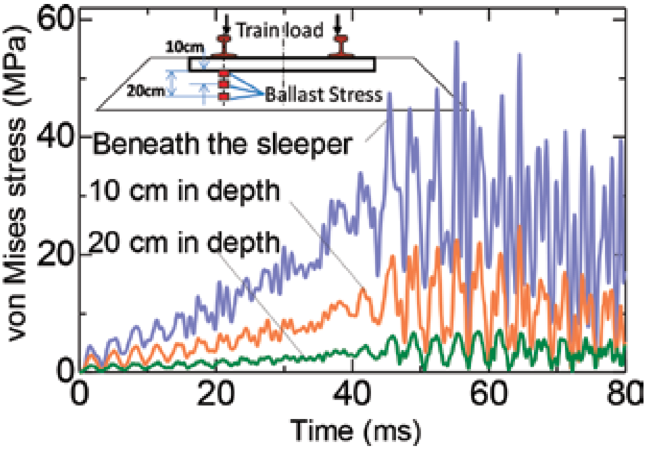

Figure 21. Time history response of the von Mises stress.

considerable stresses of approximately 57 MPa are obtained near the surface of the ballast layer under the sleeper bottom. In the figure, in general, the positive motion denotes compression and downward behaviour. Negative motion denotes tension and upward behaviour.

Figure 22 displays the linear amplitude spectra of response of von Mises stress, on the cross-section inside the gravel angle acting at different depths below the loading point of the left rail, which are obtained by conducting fast Fourier transformation of these time history response waveforms and by smoothing them at 20 Hz bandwidth. As the figure shows, these spectral curves identify the first-order elastic vibration resonance mode of the ballast layer at around 337 Hz, where the entire ballast layer stretches vertically as an elastic body.

Figure 23 presents the time history of response of the vertical displacement at the left edge of the sleeper immediately after the 0.1 ms square impulse loading waveforms of 100 kN. In this figure, the downward displacement shows the downward motion of the sleeper (i.e. ballast

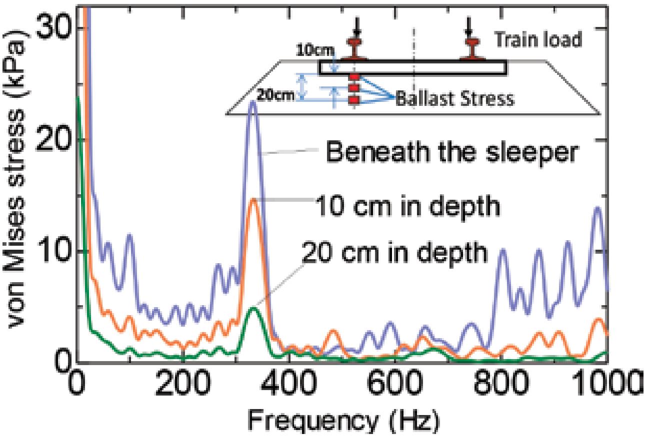

Figure 22. Spectra of von Mises stress.

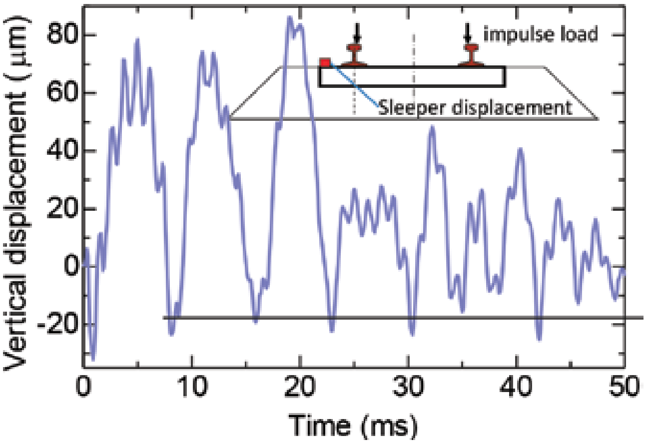

Figure 23. Time history response of sleeper displacement.

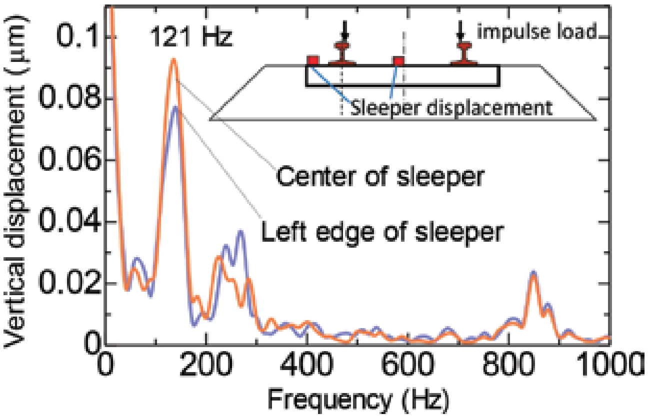

Figure 24. Response spectrum of vertical displacement related to impulse loading.

layer compression); the upward displacement represents the upward motion of sleeper (i.e. ballast layer extension). According to the figure, when an impact load is applied, the ballast layer instantaneously deforms elastically because of compression. It then returns to the preloading position. Consequently, it takes only about 1 ms for the ballast layer to be compressed and restored. Following compression and restoration of the ballast layer, sleeper-jumping occurs. The cause of this sleeper-jumping is the strain energy stored in the ballast under the compression procedure and its abrupt release.

Figure 24 presents amplitude spectra of the vertical displacement of the sleeper. Results indicate that rigid-body natural vibration occurs at around 120 Hz. The value is approximately 10–20% larger than the experimental one and is almost one-third of the elastic natural vibration frequency. Large-scale finite element analysis by tensionless analysis reveals that rigid-body natural vibration mode occurs at almost one-third of the elastic natural vibration frequency.

9. Stress on the cross-section inside the angular part of the gravel

Figure 25 presents time history waveforms of response of the von Mises stress on the cross-section inside the angular part of the gravel where the maximum response stress occurs. This analysis shows that strong stresses up to 80 MPa can be observed in tetrahedral elements near the contact part, whereas the average maximum pressure on the ballast surface is 74 kPa. The stress acting on the angular part is approximately 1100 times greater than the average value of the loading stress on the ballast surface. Assuming that the unconfined compressive strength is 60 MPa at the angular part of the ballast gravel, the application of a dynamic load of 55 kPa or more to the surface of the ballast layer under the bottom surface of the sleeper would cause minute fracturing or breakage around the angular part of the ballast gravel, where the stress will converge.

Figure 26 presents results of measurements indicating the maximum values for all sensors (measured in a cross-sectional square area with 8 cm sides on the whole bottom surface of the sleeper, total: 75 pieces, 25 units × 3 rows) as the passenger train passed. The figure also shows a threshold line of 55 kPa at which breakage will occur in the angular part of the ballast gravel.

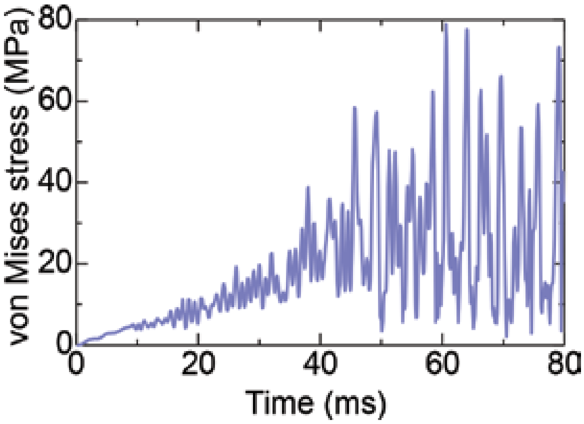

Figure 25. Time history response waveforms of the von Mises stress.

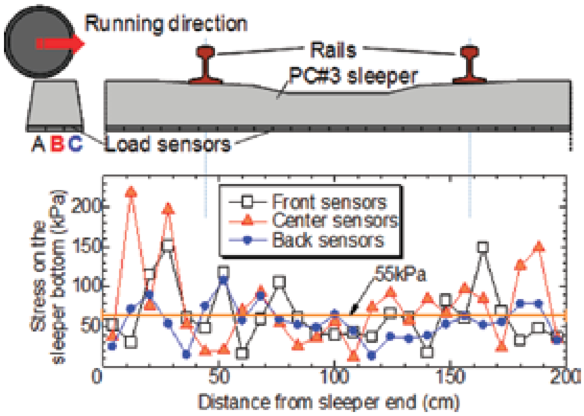

Figure 26. Distribution of the maximum load acting during passage of a passenger train.

Minute breakage might occur at points within the ballast layer where the stress converges if the measured value exceeds this line. As the figure shows, this limit was exceeded in 40 out of the 75 sensors; the ratio of exceeding the threshold is 53%. The results indicate that the degradation of the ballast layer might occur at any time under the effects of regular train passage. Further experimentation and analysis must be conducted to clarify this issue.

10. Relations among natural vibration modes of ballasted track

According to the results, when information related to the contact points between the sleeper bottom and ballast pieces is modeled with MPCs, numerically obtained results show that the vertical elastic natural vibration mode of the ballast layer occurred at about 310 Hz. However, when the contact point is modeled with nonlinear contact springs, i.e. with tensionless contact, the rigid-body natural vibration mode is found numerically as approximately 120 Hz.

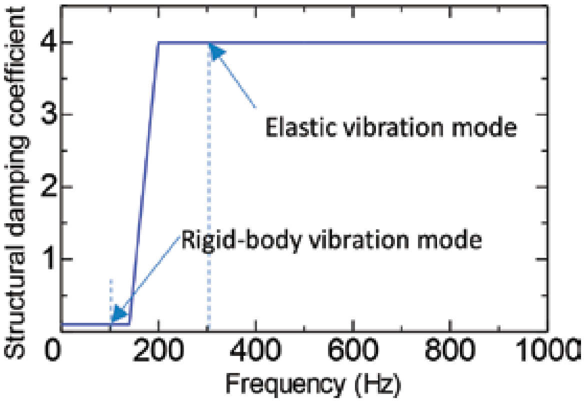

Figure 27. Structural damping coefficient in the vertical direction for a 30 cm-thick ballast layer.

The analytical result coincides to a considerable degree with those obtained using in situ measurements and full-scale experiments. Accordingly, the natural mode which is expected to occur when an impact load is applied is determined mainly by the contact condition on the sleeper bottom.

As shown in **Figure 5** presented earlier, the amplitude of displacement of the ballast gravel decreases in inverse proportion to the squares of the frequency, according to the physical theory. Therefore, the occurrence of the rigid-body natural vibration at one-third of the elastic natural vibration frequency is expected to induce nine times larger amplitude of displacement within the composite structure of the ballasted track than in the case of the elastic natural frequency. The occurrence of the rigid-body natural vibration is expected to contribute greatly to the progress of the ballast deterioration. In theory, improvement of the contact condition between the sleeper bottom and the boundary region of the ballast layer might reduce the amplitude of displacement to one-ninth at most compared with that in the current status of the ballasted track. Moreover, measurements of the ratio of the rigid-body natural vibration and the elastic vibration at the site are expected to contribute to quantitative evaluation of the ballasted track condition.

Figure 27 presents the structural damping coefficient on the sleeper bottom in the vertical direction for a 30 cm-thick ballast layer, as identified by the experimental model analysis using full-scale mock-ups of the ballasted track and precise finite element analysis according to an earlier report of the literature [24]. As the figure shows, the structural damping factor of the ballasted layer has extremely strong dependence on the frequency. The ballast layer, in the high-frequency domain over 200 Hz, provides extremely high damping functions for reducing the impact energy. However, the ballast layer is almost non-resistant to the wave components of dynamic loads in the low-frequency domain. The load components in the low-frequency domain will be reduced only slightly unless the ballast aggregate is fully constrained by an appropriate amount of uniform pressure from the surrounding area. To reduce the ballast degradation based on these mechanisms, improvement of the contact condition of the boundary region adjacent to the sleeper bottom in the ballast layer contributes to restraint of the occurrence of the rigid-body natural vibration modes at low frequencies.

11. Conclusions

As described in this chapter, although the results are limited to the ballasted track of metre-gauge railway lines in Japan, the author dealt with natural vibration modes of the ballast layer, which will engender the phenomena of ballast deterioration, based on precise field measurement, full-scale experiments and large-scale numerical analyses based on high-performance parallel computing. These results can be summarized as described below.

1. Impact loads imposed by running trains induce natural vibration modes within the ballast layer that are specific to the structure and which consequently propagate within the ballast layer through the natural vibration modes. Natural vibration modes play an important role in ballast layer deterioration.
2. According to drop-weight impact loading test, the high-frequency vibration components are dominant in the ballast responses under loading. The ballast motions during unloading are induced mainly by low-frequency vibration components that cause large displacement and which last longer.
3. Analytical results indicate that the stress acting on the angular part of the ballast gravel is approximately 1100 times greater than the average loading stress on the ballast surface under the sleeper bottom. Minute fracturing or breakage around locations where the stress acting on the angular part of the ballast gravel converges will occur at any time because of the effects of regular train passage.
4. Normal frequencies of the vertical elastic vibration mode are detected numerically at around 310 Hz. The rigid-body bounce mode of the ballast layer occurs at almost one-third of the frequency of the elastic vibration mode. These analytical normal frequencies coincide closely with the measured ones.
5. The occurrence of rigid-body modes of the ballast layers plays an important role in the progress of ballast deterioration. The improvement of the contact condition near the sleeper bottom is expected to contribute to reduction of the displacement amplitude of ballast gravel. That will reduce the ballast degradation.
6. The combined structure, which consists of the ballast layer and sleepers, vibrates in synchrony with resonance motions induced by the impulse waves. Improvement of contact conditions near the sleeper bottom is expected to contribute to reduce the displacement amplitude of the ballast gravel and to reduce ballast degradation.

Author details

Akira Aikawa

Address all correspondence to: aikawa.akira.11@rtri.or.jp

Track Dynamics Laboratory, Railway Dynamics Division, Railway Technical Research Institute, Tokyo, Japan

References

[1] Kaewunruen S, Remennikov AM. Sensitivity analysis of free vibration characteristics of an in situ railway concrete sleeper to variations of rail pad parameters. Journal of Sound and Vibration. Nov 2006;**298**(1-2):453-461

[2] Kaewunruen S, Aikawa A, Remennikov AM. Vibration attenuation at rail joints through under sleeper pads. Procedia Engineering. May 2017;**189**:193-198

[3] Sol-Sánchez M, Moreno-Navarro F, Rubio-Gámez MC. The use of elastic elements in railway tracks: A state of the art review. Construction and Building Materials. Jan 2015; **75**:293-305

[4] Remennikov A, Kaewunruen S. Experimental investigation on dynamic railway sleeper/ballast interaction. Experimental Mechanics. Feb 2006;**46**(1):57-66

[5] Kaewunruen S, Ishida M, Marich S. Dynamic wheel–rail interaction over rail squat defects. Acoust Australia. Mar 2015;**43**(1):97-107

[6] Zhao X, Li Z. The solution of frictional wheel-rail rolling contact with a 3D transient finite element model: Validation and error analysis. Wear. May 2011;**271**(1-2):444-452

[7] Zhao X, Zhao X, Liu C, Wen Z, Jin X. A study on dynamic stress intensity factors of rail cracks at high speeds by a 3D explicit finite element model of rolling contact. Wear. Nov 2016;**366-367**:60-70

[8] Sakai H, Takagaki M, Hayashi M, Aikawa A. Analysis of rolling contact behavior between wheel and rail through large-scale parallel computing. Quarterly Report of RTRI. Oct 2014;**55**(3):171-175. Available from: www.jstage.jst.go.jp/browse/rtriqr/55/3/_contents/-char/en

[9] Aikawa A. Research on vertical natural vibration characteristics of gravel aggregate in ballasted track. Quarterly Report of RTRI. 2015;**56**(1):26-32. Available from: www.jstage.jst.go.jp/article/rtriqr/56/1/56_26/_article/-char/en [Accessed: March 16, 2015]

[10] Aikawa A, Techniques to measure effects of passing trains on dynamic pressure applied to sleeper bottoms and dynamic behavior of ballast stones. Quarterly Report of RTRI. 2009;**50**(2):102-109. Available from: www.jstage.jst.go.jp/article/rtriqr/50/2/50_2_102/_article/-char/en [Accessed: June 2, 2009]

[11] Aikawa A. Determination of dynamic ballast characteristics under transient impact loading. Electronic Journal of Structural Engineering (Special Issue—Advances in Rail Track Infrastructure Research and Practice (ARTIRP)-2013). Apr 2014:17-34

[12] Aikawa A. Dynamic characterisation of a ballast layer subject to traffic impact loads using three-dimensional sensing stones and a special sensing sleeper. Construction and Building Materials. 2015;**92**(1):23-30

[13] Aikawa A. Impact-loading-test regarding ballast subsidence countermeasures using high-damping under sleeper pads and high-strength artificial ballast cubes. In: Forde MC, editor. Railway Engineering. ECS Publications, Edinburgh, UK. 2017. ISBN: 0-947644-83-014

[14] CERFACS, ENS Lyon, INPT (ENSEEIHT)-IRIT, Inria and University of Bordeaux. Multifrontal Massively Parallel Solver (MUMPS 5.1.2) Users' Guide. Oct 2017;94. Available from: http://graal.ens-lyon.fr/MUMPS/

[15] Amestoy PR, Duff IS, L'Excellent J-Y. Multifrontal parallel distributed symmetric and unsymmetric solvers. Computer Methods in Applied Mechanics and Engineering. 2000;**184**:501-520

[16] Amestoy PR, Duff IS, Koster J, L'Excellent J-Y. A fully asynchronous multifrontal solver using distributed dynamic scheduling. SIAM Journal of Matrix Analysis and Applications. 2001;**23**(1):15-41

[17] Amestoy PR, Guermouche A, L'Excellent J-Y, Pralet S. Hybrid scheduling for the parallel solution of linear systems. Parallel Computing. 2006;**32**(2):136-156

[18] Okuda H. FrontISTR Ver4.5 User's Manual, Research and Development for Next-generation Information Technology of Ministry of Education, Culture, Sports, Science and Technology, "Research and Development of Innovative Simulation Software," FrontISTR Commons. July 2016. Available from: http://www.frontistr.org/

[19] Yuan X. Advance/FrontSTR. Advance Simulation. Dec 2016;**23**:50-54. AdvanceSoft Corporation. Available from: http://www.advancesoft.jp/ (in Japanese)

[20] Aikawa A. Finite element transient response analysis on the vertical natural vibration modes of the combined structure of the ballast layer and a sleeper. Journal of Japan Society of Civil Engineers, Ser. A2 (Applied Mechanics (AM)). 2015;**71**(2):I_125-I_136. Feb 2016 (in Japanese)

[21] Grassie SL, Gregory RW, Harrison D, Johnson KL. Modelling of railway track and vehicle/track interaction at high frequencies. Vehicle System Dynamics. 1993;**22**(3-4):209-262

[22] Aikawa A. Application of a special sensing sleeper for dynamic interaction within the boundary layer between a sleeper and ballasts. In: The 11th International Conference on Computational Structures Technology (CST2012), Paper No. 130, Dubrovnik, Croatia: Civil-Comp Press, Stirlingshire, Scotland, UK; 2012. ISBN: 978-1-905088-54-6

[23] Aikawa A, Urakawa F, Abe K, Namura A. Dynamic characteristics of railway concrete sleepers using impact excitation techniques and model analysis. In: The Ninth World Congress on Railway Research (WCRR). Lille, France: SNCF; May 22-26, 2011

[24] Sakai H, Aikawa A. Finite element vibration analysis of sleepers including ballast damping characteristics. International Journal of Railway Technology (IJRT). 2012;**1**(3):37-59

[25] Railway Bureau, MILT (Ministry of Land, Infrastructure, Transport and Tourism, and Railway Technical Research Institute, Japan) and RTRI. Design Standards for Railway Structures and Commentary (Track Structures). Maruzen Publishing Co. Ltd; Kanda Jimbo-cho, Chiyoda-ku, Tokyo, Japan; 2012 (in Japanese)

[26] Urakawa F, Aikawa A, Namura A, Kono A. Development of remote automatic measuring system for long-term measurement of dynamic responses of tracks. Proceedings of Railway Mechanics. 2009;**13**:23-28 (in Japanese)

[27] Aikawa A, Urakawa F, Kono A, Namura A. Sensing sleeper for dynamic pressure measurement on a sleeper bottom induced by running trains. In: Railway Engineering. In: Forde MC, editor. UK: University of Edinburgh, Railway Gazette International; 2009. ISBN: 0-947644-65-2

[28] Aikawa A. DEM modeling techniques for dynamic analysis of ballasted railway track. In: 2nd International FLAC/DEM Symposium. Melbourne, Australia: ITASCA; 2011

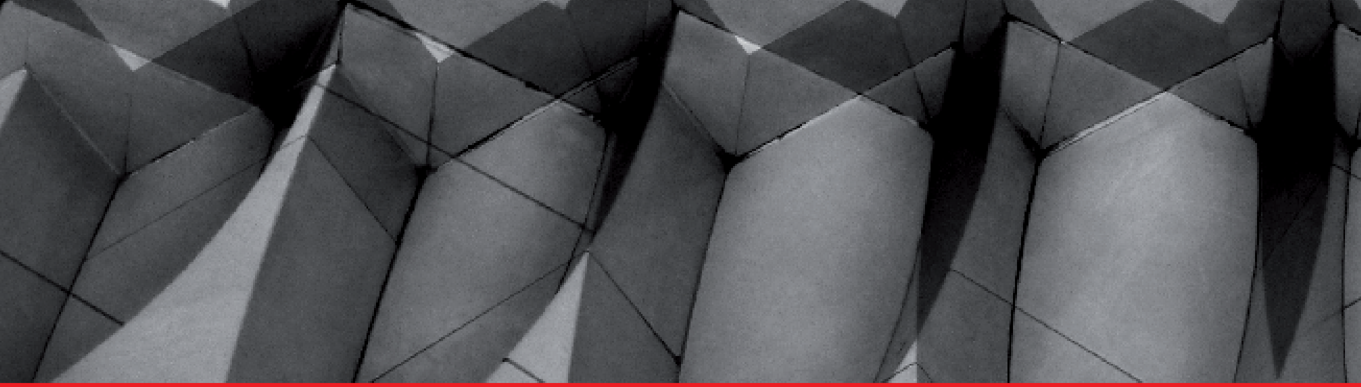

Edited by Hakan Yalciner
and Ehsan Noroozinejad Farsangi

The book presents a collection of articles on novel approaches to problems of current interest in structural engineering by academicians, researchers, and practicing structural engineers from all over the world. The book is divided into five chapters and encompasses multidisciplinary areas within structural engineering, such as structural dynamics and impact loading, structural mechanics, finite element modeling, structural vibration control, and the application of advanced composite materials. *New Trends in Structural Engineering* is a useful reference material for the structural engineering fraternity, including undergraduate and postgraduate students, academicians, researchers, and practicing engineers.

Published in London, UK

IntechOpen

ISBN 978-1-83881-745-9